Multiple Dipole Source Position and Orientation Estimation Using Non-Invasive
EEG-like Signals

by

SAINA NAMAZIFARD

Presented to the Faculty of the Graduate School of

The University of Texas at Arlington

in Partial Fulfillment of the Requirements

for the Degree of

DOCTOR OF PHILOSOPHY

THE UNIVERSITY OF TEXAS AT ARLINGTON

December 2023

To

my father Abbas Namazifard, my mother Sonia Khatami,

and my beloved husband, Mahmood Ghaffarynia

This work would not be possible without all your love and support.

Acknowledgements

I would like to express my sincere appreciation to the many individuals and organizations who have played a vital role in shaping my journey throughout the past four years of my doctoral research.

First and foremost, I would like to express my deep gratitude to my supervising professor, Dr. Kamesh Subbarao, and co-supervising professor, Dr. Ashfaq Adnan. I have learned a lot from them over the past four years, and this dissertation would have been impossible without their support, patience, and invaluable guidance.

I would like to extend my sincere appreciation to the members of my thesis committee, Dr. Khosrow Behbehani, Dr. Paul Davidson, and Dr. Md Rassel Raihan, for their time, expertise, and critical input. Their feedback and guidance have been pivotal in shaping the direction of my research and its overall quality.

I sincerely acknowledge Dr. Timothy Bentley (Deputy, FHP Program) and the Office of Naval Research (ONR: N00014-21-1-2051 and ONR: N00014-19-1-2383) for supporting this work.

I extend my heartfelt thanks to the administrative staff at the Department of Mechanical and Aerospace Engineering for making my Ph.D. journey pleasant. Special thanks to Lanie Gordon and Wendy Ryan for their support and dedication.

My present and past labmates from Aerospace Systems Laboratory (ASL), and Multiscale Mechanics and Physics Lab (MMPL), who have shared this academic journey with me, deserve special recognition. In particular, I want to thank my friends Diganta, Rajnish, Kati, Baris, Cem, Kashish, and Edward for their warm welcome and invaluable guidance when I first arrived in the USA and joined the

Abstract

Multiple Dipole Source Position and Orientation Estimation Using Non-Invasive
EEG-like Signals

Saina Namazifard, Ph.D.

The University of Texas at Arlington, 2023

Supervising Professor: Dr. Kamesh Subbarao

Co-Supervising Professor: Dr. Ashfaq Adnan

The human brain comprises of neurons that connect with each other via electrical signals. One can record and measure these activities using an electroencephalogram (EEG). An essential use of the EEG is in locating the generating source of these signals, usually approximated by dipoles. This is important because, in some particular circumstances, neurons may not function optimally and could make the equivalent dipole generate abnormal signals. This could be a result of seizures or other brain disorders. In order to isolate such disorders, the challenge is to find a non-invasive way to locate the anomalous source.

This research aims to introduce an algorithm that not only can precisely detect the source location of an EEG-like signal but also estimate all other characteristic signal features, such as orientation and magnitude. In general, any source identification problem is solved in two steps. The first step is called the Forward Problem, where the measured signal is simulated mathematically. In the Forward Problem, it is assumed that all the parameters, such as the location of the sensors on the scalp,

the properties of the source (location, orientation, and magnitude), and the head model conductivity, are known. All the mentioned properties are passed to a proper mathematical model that can simulate the signal measured by each sensor.

The second step is the Inverse Problem, which aims to predict the source properties. This problem starts in the opposite direction to the Forward Problem. In this case, it is assumed that the collected signals from the sensors are available, and by utilizing the present mathematical model, one should be able to find the source location and other features. Among different methods to solve the Inverse Problem, a Least Squares error-based Source Localization algorithm is used. This algorithm enables us to add both linear and non-linear constraints, which optimize solving the source identification problem.

Given the absence of the physical source in the EEG-like signal, the actual values of source properties are unknown. Thus, to evaluate the accuracy of the proposed source identification algorithm and compare the estimation results to the actual values, one can use three main approaches. First, one can use the Forward Problem to generate synthetic data where it is assumed that all the dipole features are known. Hence, the estimation result can be compared to these available source properties. Second, comparing the estimation result to one of the available and well-known software is recommended. This study uses the popular MATLAB-based software called EEGLAB to evaluate the proposed estimation.

The third approach to assess the estimation accuracy of the presented method is to use an experimental setup and generate EEG-like signals. In this case, the source is visible, unlike the EEG signals, and all the source properties are known. Since a realistic head phantom is complicated to make and unavailable in many laboratories, a simple experimental setup, including a bucket filled with salt and water, is used to generate the EEG-like signals. This setup is very common for fundamental EEG signal

tests. In this experiment, the electrical sources generate a sine wave with different frequencies to make the test more complicated and challenge the least squares error based source identification algorithm. The proposed algorithm uses the measured data from different oscillatory signal sources and solves an inverse problem by minimizing a cost function to estimate all the signal properties, including the locations, frequencies, and phases. To increase the overall signal accuracy for a wide range of initial guess frequencies, we have utilized the Lomb-Scargle spectral analysis along with the Least Squares error optimization method. We observed that our algorithm can identify the source location within 10 mm from the actual source immersed inside the bucket of radius $=\sim$ 90 mm. Moreover, the frequency estimation error is nearly zero, which justifies the effectiveness of our proposed method.

Finally, we have introduced a novel head model which considered different conductivities without using Finite Element Method (FEM). This approach is based on random conductivity distribution and is computationally less expensive than FEM while providing an acceptable result to generate EEG signals using Forward Model.

Table of Contents

List of Illustrations

List of Tables

Chapter 1

Introduction

Recent studies on EEG forward models and inverse problem solutions are less focused on proposing a novel algorithm or head model, and instead, they focus on details to improve the results. For instance, many studies focus on the thickness of the skull or the number of tissues in a head model and utilize the common source localization algorithms to find the results. However, this study aims to find a novel approach for both the EEG forward model and the source identification.

1.1 Objectives of the Research

The objectives of this research are summarized as follows:

1. Introducing a novel head model to avoid the expensive computation load of conventional algorithms such as the Finite Element Method (FEM). In this head model, the conductivity of different parts of the head model is considered entirely random instead of using the common layered head models. The effect of this head model is addressed for the forward model and the inverse problem. For both cases, the simulation result is acceptable, which means one can substitute this approach to reduce the simulation's run-time while maintaining the simulation results' accuracy.

2. There are standard positions to locate the sensors on the scalp while recording the EEG signal. This study addresses the effect of random sensor locations on EEG source identification results. The provided result shows that, in this case, the number of sensors is more important than the location of the sensors,

and it is optional to keep a certain distance between the adjacent sensors. It is essential to mention that the sensors in this simulation are uniformly distributed on the scalp to ensure that the whole head area is covered with a reasonable amount of sensors.

3. Among various source localization methods, this study uses a constrained least squares error approach to optimize the source identification algorithm. There are two constraints considered in this approach. Firstly, the orientation and the magnitude of the dipole are considered separately. Thus the orientation can be considered as a unit vector. This feature's associated constraint ensures that the orientation vector's norm always equals one. The second constraint is an inequality that forces the source localization result located in the head model. In other words, if the source localization result is outside the head model, the algorithm rejects the answer.

4. The proposed algorithm is also used for an experimental setup where the electrical source generates a sine wave. The introduced algorithm based on the constrained least squares error is modified so it can estimate all the features of the present electrical source, including the location, magnitude, phase, and frequency. Moreover, the Lomb-Scargle method is added to the source identification algorithm to have a more accurate estimation result for the frequency. This method helps to have a precise frequency estimation for the case of unevenly sampled data. In other words, if data loss occurs while recording, this algorithm can still find the dominant frequencies accurately.

5. The next objective of this research is to find the limitations of the proposed algorithm while using experimental data. Usually, when an algorithm is introduced, only the theoretical performance is shown, not the limitations. Hence, this study shows how the complexity of the experiment might affect the accu-

racy of the estimation result. For instance, the number of dominant frequencies is increased from one to four to check if the proposed algorithm can detect all of them. In another experiment, the number of sources increased, which means that the number of unknowns increased significantly for the same amount of data. The result shows the limit of source numbers for the available experimental setup and estimation algorithm.

6. The final objective is to find more EEG sources in the head compared to the standard algorithms and software. This part uses clinical data of a patient with active seizures. The result shows that our algorithm could detect an extra source of the signal while the well-known software EEGLAB could not find it.

1.2 Problem Specification and Requirements

This research aims to optimize the source localization result and estimate other electrical source features such as the magnitude and frequency. More specifically, the presented algorithm is designed to apply to low-voltage electrical signals immersed in a conductive medium. An excellent example of the described problem is the EEG signal source identification.

In terms of the source localization problem, many studies tackle reducing the estimation error. Fig.1.1 schematically defines the problem. It can be inferred from Fig.1.1 that while the exact location of the electrical source is fixed at a point (identified as a red dot), the typical source identification algorithms can only estimate the source location within an area (the green circle). The ideal goal is to reduce the radius of the estimation result (i.e., the radius of the green circle) until it gets as small as the red dot. When this happens, it means the source localization method works accurately. To achieve this goal, it is required to choose a proper source localization

3

algorithm. Among all different algorithms, this study utilizes the Least Squares error since it enables one to add constraints and optimize the simulation result.
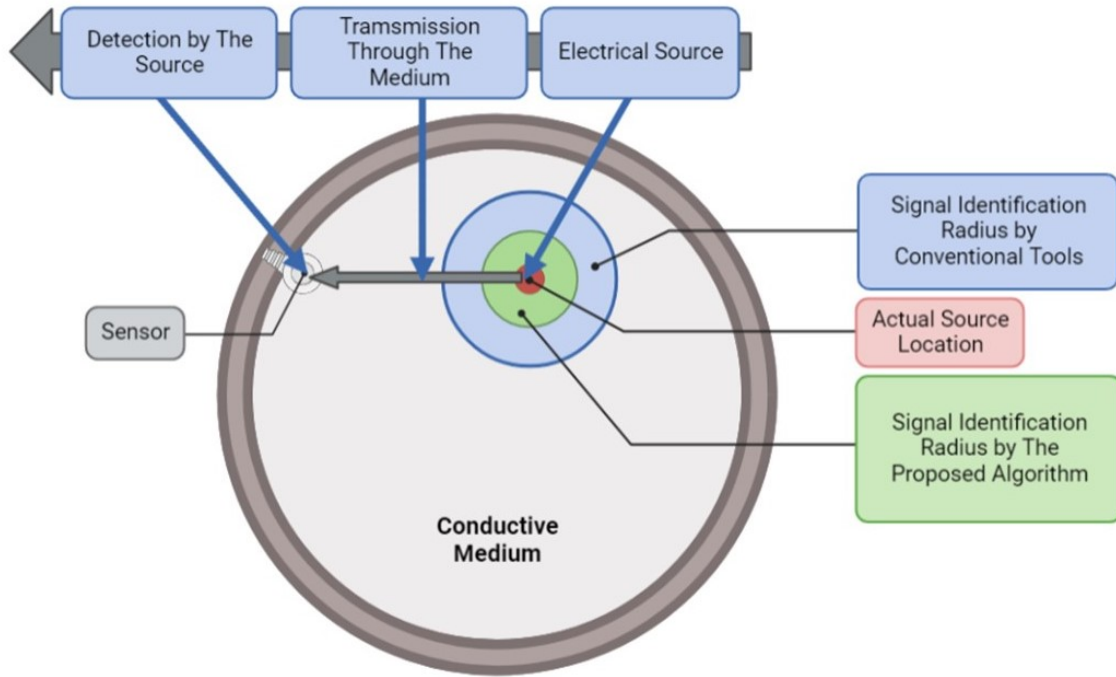
Figure 1.1: An illustration of the general form of the source localization problem

The other problem to solve is to find the electrical source's features other than its location. Depending on the nature of the signal, these features can be frequency, phase, magnitude, and orientation. Since many of the algorithms only focus on estimating the location of the source (source localization algorithm), this raises an interesting question on how to estimate these unknowns precisely. Although the constrained least squares error mentioned previously can be helpful, one needs to add additional steps to have an accurate estimation result. For instance, if the electrical signal generates an oscillatory signal, finding a proper estimation for the frequency can be challenging. The reason for this problem is a nonlinear term in the estimation,

which is highly sensitive to its initial guess while using the least square estimation. To solve this problem, methods like Fast Fourier Transform (FFT) and Lomb-Scargle spectral analysis can be constructive. Fig.1.2 illustrates how to solve the mentioned problem by adding an extra frequency analysis step before passing it to the source identification algorithm.

Eventually, there is a common problem in balancing the accuracy of the source identification result and the computational load. Modeling the head considering its geometry and all other details leads to this problem. The majority of the studies solve this problem by using the Finite Element Model (FEM) to solve the forward problem and model the head accurately. This approach brings a significant advantage of considering all the details and head tissues in solving the forward problem. However, this solution has a computational burden, making it not a suitable option for real-time EEG data analysis implementations. As a consequence, it is required to introduce a new algorithm to diminish the computational load while simulating the head details properly. This study shows that a novel forward model based on randomly distributed conductivity can be a suitable alternative to FEM.
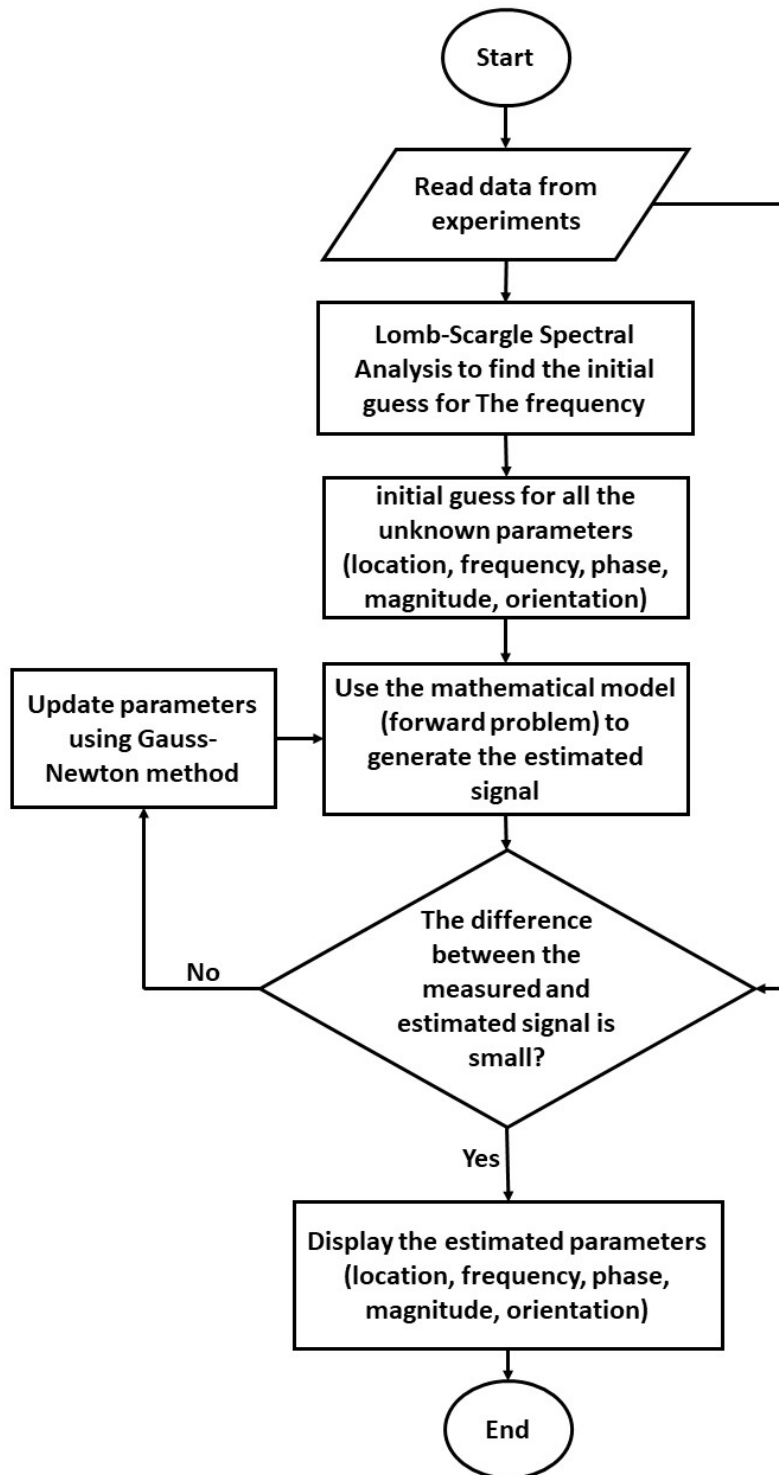
Figure 1.2: Inverse problem solution using Least Squares error algorithm illustrated by a flowchart

1.3 Background and Motivation

This section summarizes the background information and related literature work on the components of this research.

1.3.1 EEG Source Analysis and the Forward Problem

The EEG source analysis, particularly the source localization problem, involves two main steps to solve. The first step is called the forward problem, where the main focus is defining a proper head model and a mathematical model to generate the EEG signal. To put it another way, in this step, it is assumed that all the information about the dipole properties, such as the location, orientation, and magnitude, are available, and one only needs an appropriate mathematical model to generate the associated signal by this dipole.

1.3.1.1 Head Geometry

Finding a proper EEG forward model includes various subjects, from the shape of the head to modeling the head tissue conductivities. This section aims to cover most of these critical subjects and how researchers address them.

First, let us start with the shape of the head. Two main head models are expected in EEG signal analysis studies: 1) spherical head model and 2) realistic head model. As the mentioned head model name implies, the first model considers the head a half-sphere or a whole-sphere head model. As expected, this head model is less realistic, and it is employed in studies where the simplification of the head model is important. The second model is based on the actual head shape. To use this model, it is common to consider different coordinates, such as Talaraich and Montreal Neurological Institute (MNI) coordinates. The Talairach coordinated is based on considering the brain details and a specific line between the anterior commissure

(AC) and posterior commissure (PC). Since these coordinates details come from the X-ray, they can be slightly different from person to a person [2,3]. On the other hand, the MNI coordinate is based on an average head model of 250 normal MRI scans [4]. Thus, the MNI coordinate is more general compared to the Talairach coordinates. Referring to these definitions, this type of head model is utilized when the accuracy of head geometry is essential, and it can drastically affect the EEG data analysis result.

Motivation. For any EEG source analysis, addressing whether the simplified head model (spherical) and the realistic head model work appropriately is critical. In this research, the simulation result for the source localization is provided for both cases.

1.3.1.2 Head Model and the Conductivities

The second feature that plays a significant role in an EEG forward model is the number of head tissues considered. This subject is vital since the conductivity of different tissues can vary approximately from $1e-6 S/m$ to $1.79 S/m$ [5]. This suggests that the electrical signal generated from a dipole should transmit through different tissues with specific conductivities, which can make a difference in the measured voltage on the scalp. Most studies consider a layered head model to simulate different head tissues. While seeing a single layer of the brain in earlier studies is common [6], recent works usually focus on considering as many layers as possible. For instance, in [7,8], a total of 13 tissues are considered in the head model.

Motivation. Given the accuracy of the head models with a large number of simulated head tissues, it is critical to note that these types of simulations are not always beneficial as they usually have a computational burden. Thus, the lack of a new algorithm to consider different conductivities while easy to compute is notable.

1.3.1.3 A Solution to the Mathematical Forward Model

Despite the number of layers, it is crucial to address the method to mathematically model these conductivities and add other features of the model, including the location of the sensors on the scalp and the dipole features. To achieve this goal, it is recommended to use the quasi-static approximation of Maxwell's equations and the Biot-Savart Low, which leads to a general formula to calculate the EEG signal generated from dipoles in the head model, transmitted through the head tissues and eventually collected by EEG sensors located on the scalp [9, 10].

A common approach to solve this forward model to calculate the potential on the scalp while considering more than one conductivity is using the Finite Element Method (FEM). The concept of the Finite Element Method is to divide the desired volume considered in a study into smaller subspaces. The most common shapes of subspaces for the 3D case are tetrahedra or hexahedra [11]. Some studies show the hexahedral model has more advantages and is more common to use [12, 13]. These shapes eventually form a mesh all over the desired volume, which is the head model in this research. This method helps to find the voltage on the scalp, generated from a dipole and transmitted through different tissues with various conductivities in the head model. The advantage of this method is to simulate the conductivity of different tissues very accurately using a massive number of elements [14, 15]. However, this huge number of elements can make a computational burden while simulating the forward model. To solve an EEG forward problem using the FEM method, many common approaches are used, such as the Venant [16], the partial integration [17], the Whitney or Raviart-Thomas [18], and the subtraction approach [19]. All of the above studies mostly use the Continuous Galerkin FEM (CG-FEM) to solve

the problem. Moreover, some studies tackle optimizing the Galerkin approach by introducing modified methods such as the Mixed-FEM [20].

Motivation. From the abovementioned background on how to solve the forward model to find the potential on the scalp, it is concluded that the balance between the accuracy and the computational load is an essential factor. A fast and precise algorithm can solve many different problems in this research area, including real-time EEG data analysis.

1.3.2   Inverse Problem

Detecting the specific location of an electrical signal source immersed in a conductive medium is one of the critical problems in signal identification applications. Most prominent applications include underwater source localization [21, 22] and the Electroencephalography(EEG)/Magnetoencephalography(MEG) signal source localization [23]. The underwater source localization application can vary from underwater vehicle tracking to a vital task like an underwater rescue mission. The EEG/MEG source localization is also important since it is directly related to neurological disorders and can affect human health. It is certain that the application of an optimized source localization algorithm is versatile and can be used to solve many critical problems, including the ones mentioned. In the mentioned cases, the process starts with an electrical signal source that generates an electrical signal. Then signal transmits through a medium from the source to the sensors. Next, the signal is analyzed. These steps collectively provide the spatial location of the electrical source. Since each application involves different environmental conditions, the source identification algorithm must be adapted to ensure accuracy.

The EEG/MEG source localization process is essential in detecting different neurological diseases. In principle, an EEG is used to detect brain signals [24], and a

MEG is used to detect the magnetic fields produced by the electrical current inside the brain [25]. In both detection processes, the human head acts as a conductive medium where its outer surface is used for sensors (i.e., electrodes) to sense signals that are generated somewhere beneath the inner surface (i.e., specific brain signals) [26,27]. In other words, the human head transmits the source generated inside the brain to the electrodes attached to the head. Then recorded data is used for source localization of that electrical signal source. A healthy human brain generates brain waves with a specific range of frequencies and amplitudes [28, 29]. Following some specific motor or sensory activities, the frequencies and amplitudes of the brain waves change. By comparing and analyzing the recorded EEG data, before and after the specific activities, any sign of abnormalities at a particular brain region can be predicted [30]. Over the past several years, various methods have been used to solve the localization problem [31]. Note that there are different applications such as image processing [32–34], fault location in grounded/ungrounded and high-resistance systems [35], and sound source localization [36,37]. Depending on the application, the solution methodologies are different. In principle, all these methods solve an inverse problem. Nevertheless, all methods have their own advantages and limitations.

The Minimum Norm (MN) method for this application was first introduced in 1994 [38] to solve the specific inverse problem and source localization from EEG signals. This method is proper for noise-free signal analysis, but it needs to provide a better result for the deep source localization cases where noise can be inherently present in the signal source. In the same year, a new algorithm called Low-Resolution Electromagnetic Tomography (LORETA) was introduced [39]. The LORETA can be considered an integrated method combining the weighted minimum norm (WMN) technique [40] with the Laplacian operation. It resolves the deep source localization

problem of the MN method. However, the low spatial resolution can be the main disadvantage of this algorithm.

Implementing the recursive steps in solving the inverse source localization problem has significantly improved the results. FOCal Underdetermined System Solution (FOCUSS) is one of these methods which utilizes the WMN to solve the recursive process. FOCUSS could solve the problem of low-resolution results with the LORETA algorithm properly [41].

Another popular EEG source localization method is the Recursive multiple signal classification (MUSIC) [42]. This method defines the source (dipole) in a 3D grid head model. The algorithm is based on the idea of finding a signal subspace and addressing if it works the best for the forward model.

The existing EEG source localization methods are often modified or combined to generate new algorithms. Examples include methods such as Exact low-resolution brain electromagnetic tomography (eLORETA), standardized low-resolution electromagnetic tomographic analysis (sLORETA), RAP MUSIC, LORETA FOCUSS, etc. [31]. The new methods offer applications beyond the traditional EEG source localization algorithms. For instance, the MUSIC method can also be used in sound source localization, as illustrated in [43]. Another application is the acoustic source localization problem. This usually addresses the source localization for the 2D case (both isotropic and anisotropic plates) and the 3D structures. One of the most famous methods is Beamforming which is also utilized in the EEG source localization problems [44]. The advantage of using such methods over traditional EEG source localization methods is the robust behavior of the noisy data with the White Gaussian noise. Also, a few source localization methods depend on knowing the Time of Arrival (TOA) information [45]. In other words, the time a specific signal needs to travel from the source until it reaches the sensor should be available. However, the

Beamforming method works appropriately regardless of having the precise Time of Arrival (TOA). Thus, depending on the situation, these methods can not only be used for source localization inside the human brain but also used for similar kinds of applications.

The Least-squares method uses the real collected signal and the signal generated by the hypothetical electrical source to identify the electrical source. Finding the global minimum of these two signal differences provides the final answer to the source estimation [46].

As mentioned earlier, MUSIC [47] is one of the common methods in different application areas and is not limited to EEG source localization problems. It should be noted that most of the algorithms mentioned earlier can only detect the location of the sources but not the other features, such as the simultaneous detection of frequencies, phases, and amplitudes of the multiple active electrical signal sources. More information about the electrical source can be important for many reasons. For instance, in the case of a rescue mission, there might be other active electrical sources in the water. The specific amplitude and phase information can help distinguish the emergency pulse-generating device from the other electrical sources.

Motivation. This section is a representation of various source localization algorithms including their advantages and disadvantages. This suggests that finding a proper algorithm that can estimate the source location along with its other characteristics can be challenging. Based on the mentioned features of each approach, this study uses the constrained least squares error method to solve the inverse problem and provide the estimation results.

1.4 Contributions of the Research

The major contributions of this research so far are summarized in this section along with the publications.

1.4.1 Optimizing the Source Localization algorithm

Firstly, we focus on optimizing the source localization result and reducing the estimation error. Following are more details of this research's contribution along with the regarding publication.

1. This research aims to estimate all dipole features in the head model. Unlike other studies that focus only on source localization, the presented algorithm can also estimate the orientation and the magnitude.

2. The presented algorithm is tested for many different cases. For instance, two different head geometry (spherical and realistic) is considered in this study. Also, the number of sensors on the scalp and the number of samples are changed to check the effect of these two variables on the EEG source identification result. Moreover, the effect of sensor location is addressed in this study. The goal is to find if the accurate standard location of the sensors on the scalp is critically important or if one can ignore this factor and just focus on the number of sensors instead.

3. A novel forward model based on random conductivity is introduced in this research. The research aims to find a way to reduce the computational cost while keeping various numbers of conductivities in the head model.

   The publication based on the research above is listed below:

- Namazifard, Saina, and Kamesh Subbarao. "Multiple Dipole Source Position and Orientation Estimation Using Non-Invasive EEG-like Signals." Sensors 23.5 (2023): 2855.

1.4.2 Underwater Source Identification

This research is an expansion of the previous one, where the algorithm is appropriately modified for the underwater source identification case. The study also adds an experimental setup to evaluate the updated algorithm with real/experimental data.

1. This study introduces a novel algorithm to optimize source identification where low-voltage (mV range) signals transmit through a conductive medium. The proposed algorithm uses the measured data from different oscillatory signal sources and solves an inverse problem by minimizing a cost function to estimate all the signal properties, including the locations, frequencies, and phases.

2. In order to have an accurate result for the frequency estimation, the Lomb-Scargle spectral analysis is employed along with the least squares error optimization method. This method is appropriate for unevenly sampled data. In other words, if any of the sensors are defective and not recording the data correctly, or the data loss occurs for any other reason, the proposed algorithm can still estimate the frequency.

The publications based on the research above are listed below:

- Namazifard, Saina, et al. "Method for Identification of Multiple Low-Voltage Signal Sources Transmitted Through a Conductive Medium." IEEE Access 10 (2022): 124154-124166.

1.4.3 A Novel Forward Model Based on the Random Conductivity

As mentioned earlier, a novel head model based on random conductivities is used to solve the source identification problem. This study only focuses on the effect of the random conductivity assumption on the forward problem. In other words, this study addresses the EEG reconstruction signal using the new forward model. To

ensure that this model can regenerate the EEG signal correctly, the result is compared to the clinical EEG signal and BESA software.

1. The common way to solve an EEG forward problem while maintaining accuracy is to utilize the Finite Element Method (FEM). However, this method's computational burden makes it unsuitable for specific applications such as real-time EEG source analysis. To decrease the run-time or the computational load, this study eliminated the FEM process and used a random conductivity head model. It should be noted that these random numbers are carefully chosen from a reasonable range to simulate different head model layers.

   The publication based on the research above is listed below:

- Saina Namazifard, and Kamesh Subbarao, "EEG Forward Modeling using Random Conductivity," (To be submitted).

1.5 Dissertation Outline

This dissertation is divided into five chapters, and it is organized as follows: Chapter 2 starts with a complete definition of the EEG source identification problem. The focus of this chapter is on utilizing the Constrained Least Squares error to solve the EEG source identification problem. The results are provided for different data sets, including synthetic and clinical EEG data. This chapter also covers the effect of different factors on source localization results, such as the head model, including its geometry and conductivity simulation, sensor placement of the scalp, number of samples, and many more.

Chapter 3 presents the enhanced source identification method based on the Constrained Least Squares error. The present algorithm is designed for an oscillatory electrical signal transmitted through salt and water until it reaches the EEG sensors. Besides the source localization estimation, this algorithm determines the frequency,

phase, and magnitude of the electrical signal. The goal of this study is to develop our algorithm for a phantom head experiment in the future.

Chapter 4 focuses on the head model and solving the forward problem. This study aims to solve the computational burden of common algorithms such as Finite Element method (FEM), Boundary Element Method (BEM), and more. The novel head model that is introduced in this chapter is based on random conductivity. The results provided in this section compare the EEG signal generated from our forward model to clinical EEG data as well as a well-known software called BESA.

Lastly, Chapter 5 presents the conclusion and provides a few suggestions for future works related to EEG source identification subject.

Chapter 2

Multiple Dipole Source Position and Orientation Estimation Using Non-Invasive
EEG-like Signals[1]

The human brain comprises of neurons that connect with each other via electrical signals. One can record and measure these activities using an electroencephalogram (EEG) [49]. An essential use of the EEG is in locating the generating source of these signals, usually approximated by dipoles. This is important because, in some particular circumstances, neurons may not function optimally and could make the equivalent dipole generate abnormal signals. This could be a result of seizures or other brain disorders. In order to isolate such disorders, the challenge is to find a non-invasive way to locate the anomalous source. In [50], the authors address the location of abnormality for mild depressed patients. In this case, only few regions were associated with depression. Thus to treat these disorders, source localization is crucial and vital in clinical subjects exhibiting such neural activity [51].

EEG signals' source localization has been extensively studied. Cohen et al in [52] additionally compared the accuracy of using EEG signals versus magnetoencephalogram (MEG) signals and showed that EEG signals are as useful as MEG signals for source localization problems. Further, in [53], the authors described trend source localization methods using the finite element method for modeling the human head, and also defined a time-slices approach.

---

[1]Part of the material reported in this chapter is reprinted with permission, from "Namazifard, Saina, and Kamesh Subbarao. "Multiple Dipole Source Position and Orientation Estimation Using Non-Invasive EEG-like Signals." Sensors 23.5 (2023): 2855." (reference [48]).

Among all the studies, there are two important steps for source localization: 1) The forward model for EEG signal approximation; and 2) The inverse problem for locating the generating source. In the forward problem, the electrode potentials are calculated based on the given source properties. Many review articles address different forward problem approaches pertaining to source localization as in [54]. Other studies such as [55, 56] focused on a specific forward problem approach like implementing the boundary element method (BEM) and its effect on source localization error. Moreover, in [57], the effect of forward model errors, and the way to remove them using a Monte Carlo approach is also discussed. The inverse problem on the other hand is solved when the EEG signals are available and measured by electrodes, and the goal is essentially to estimate the signal properties. There are several inverse problem approaches available to find the source location of the signal generators or the dipoles. Robert Grech and his co-authors present a comprehensive review of the approaches, that include the minimum norm estimates, Low Resolution Electromagnetic Tomography (LORETA), Local AUtoRegressive Average (LAURA), Adaptive standardized LORETA/FOCUSS (ALF), and Multiple Signal Classification (MUSIC) [46]. Among these mentioned methods, MUSIC is widely cited (and used) and the main idea is based on the subspace decomposition technique [58]. In other words, this technique tries to select the best signal subspace that works properly for the forward model.[9] builds upon this by introducing a new algorithm based on QR decomposition, and compares it to other available algorithms such as Recursively Applied and Projected MUSIC (RAP-MUSIC) [59]. One of the recent studies showed promising results by using the L_2 norm to solve the underlying ill-posed inverse problem based on Bernoulli Laplacian Priors [60].

Besides the need for robust mathematical algorithms to solve the source localization problem from EEG signals, there is also the need to model the propagation

of the signal through the brain media (matter) before the signal is picked up by the sensors. Among the key factors that affect the signal quality, is the conductivity of the brain matter. For example, [61, 62] implement non-uniform conductivity for the head model. In similar studies, researchers have mostly considered different conductivity for the skin, compact bone, spongy bone, and the brain. Despite these models' popularity, other novel methods exist to solve the forward problem more accurately. For instance, [63] presents a two volume integral equation for the inhomogeneous and anisotropic forward problem, which is more precise than common differential equation-based available methods.

Another important aspect that impacts the source localization solution is the number, and the distribution of the sensors. Many studies are available that show the sensitivity of the solution to different number of sensors, and also examine the number of sensors needed to have a precise solution [64, 65]. There are also studies like [66] that quantify the mis-location of sensors considering them as random variables. However, these studies do not address the effect of the distance from electrodes to the signal resource nor the Received Signal Strength (RSS) attenuation in the source localization problem.

In this chapter, a new algorithm will be introduced to estimate the dipoles' properties, namely strength, location, and orientation, using EEG-like signals. The main contribution is the development of a mathematical model that can be utilized in the inverse solution to determine the source location and orientation. The developed model considers randomly distributed conductivity in the 'head model' as well as randomly distributed sensor locations. This model captures a wide variety of signals received from head models (Finite Element Method based on specified conductivities

for matter inside). The models are verified using the tools from Brain Electrical Source Analysis (BESA) [1].

In the following sections of this chapter, the inverse problem is setup by describing the components of a measurement model. Following this, the solution methodology is presented that describes a constrained optimization approach to solve the inverse problem. The introduced algorithm is applied to three different data sets. First, synthetic data generated by a forward model is utilized to assess the accuracy of the source properties estimation. Second, two different clinical data sets, including a seizure, are considered. Eventually, all the results are compared using a widely available tool - EEGLAB [67].

2.1 EEG Measurement Model

This section describes the EEG measurement model that is utilized to generate synthetic EEG measurements.

2.1.1 Head Model

In this study, two different head models are evaluated: 1) a hemi-spherical (half sphere) head model, as shown in Fig. 2.1; 2) a realistic head model based on the Montreal Neurological Institute (MNI) coordinates. A comparison of these two head models is presented in Fig. 2.2. Note that in both head models +y axis passes through the nasion, and the +x axis passes through the right ear. First, let us consider a half sphere as a brain model which is shown in Fig. 2.1.

---

[1] https://www.besa.de/products/besa-research/features/head-model-selection/
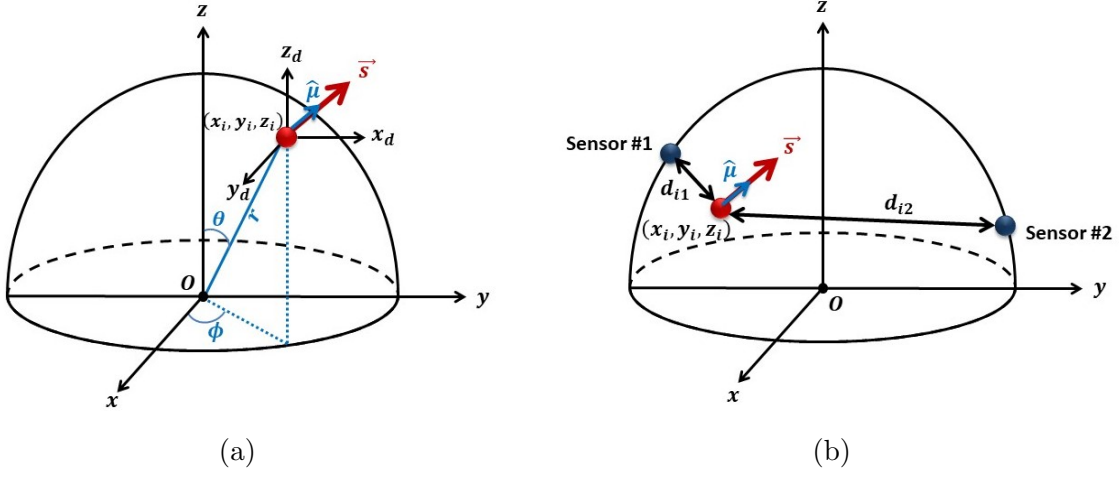
Figure 2.1: Half sphere head model: [a] Spherical coordinates, [b] An example of two sensors in the presence of the ith dipole

According to the Fig. 2.1.[a], the location of any i^{th} dipole with respect to the origin by utilizing spherical coordinates can be presented in a vector $\boldsymbol{l}_i = [l_{x_i} \ l_{y_i} \ l_{z_i}]^T$, given as:

$$\begin{cases} l_{x_i} & = & r_i \sin\theta_i \cos\phi_i \\ l_{y_i} & = & r_i \sin\theta_i \sin\phi_i \\ l_{z_i} & = & r_i \cos\theta_i \end{cases} \tag{2.1}$$

In this study, the radius of the brain spherical model is considered as $r = 10$ cm thus, $r_i \in [0, \ 10)$. Moreover, the two angles are defined as $\theta_i \in [0, \frac{\pi}{2})$ and $\phi_i \in [0, 2\pi)$ to cover the whole half sphere head model.

Similarly the jth sensor location is described as $\boldsymbol{w}_j = [w_{x_j} \ w_{y_j} \ w_{z_j}]^T$, obtained using

$$\begin{cases} w_{x_j} & = & r \sin\theta_j \cos\phi_j \\ w_{y_j} & = & r \sin\theta_j \sin\phi_j \\ w_{z_j} & = & r \cos\theta_j \end{cases} \tag{2.2}$$

Fig. 2.1.[b] illustrates the relation of the ith dipole and two selected sensors.

22
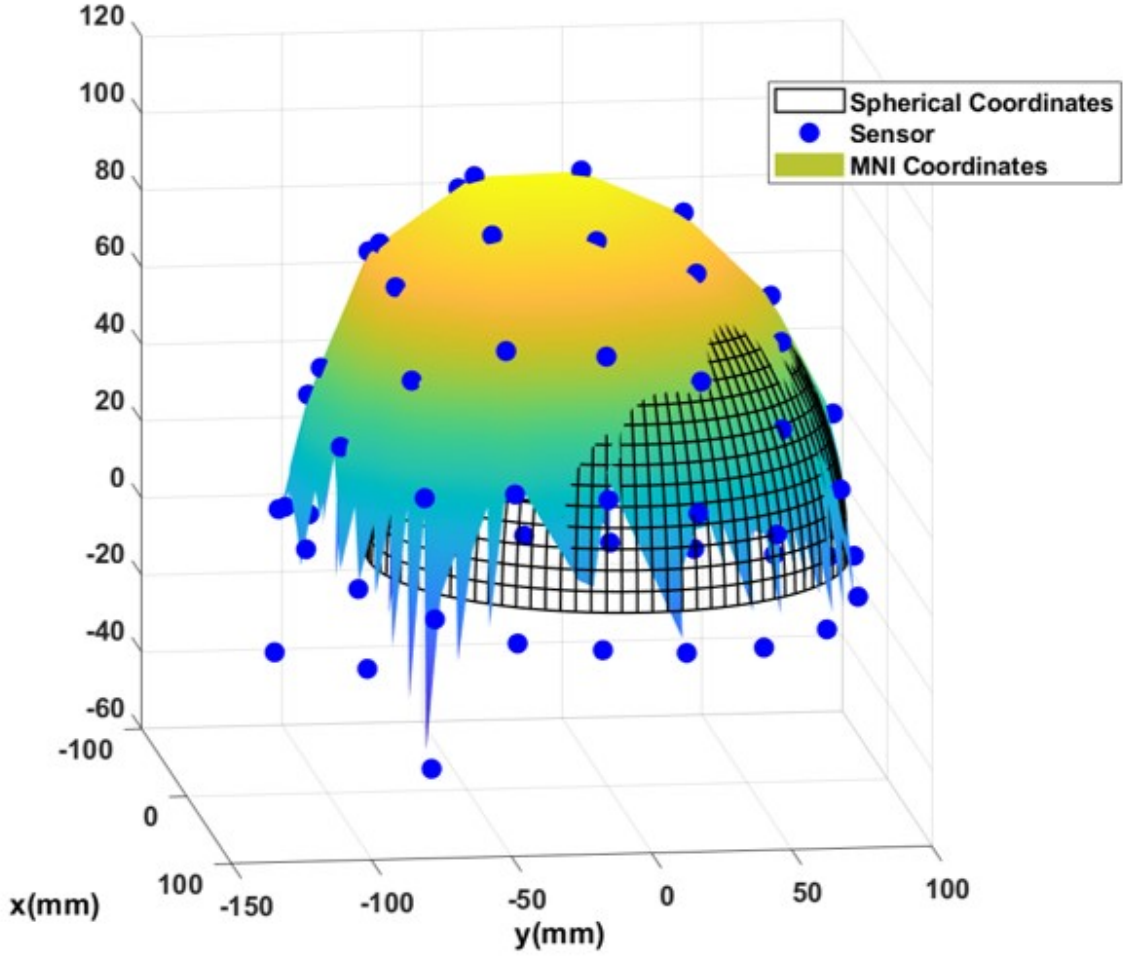
Figure 2.2: MNI and Spherical head model in a same figure

The vector $\boldsymbol{s}_i = s_i \, \boldsymbol{\mu}_i \in \mathbb{R}^{3 \times 1}$ is the dipole signal strength (with units as Coulomb-meter), $\boldsymbol{\mu}_i \in \mathbb{R}^{3 \times 1}$ is the unit vector denoting the orientation of the dipole, and $s_i \in \mathbb{R}$ is the magnitude. An alternate representation could be, $\boldsymbol{s}_i = [s_{x_i} \; s_{y_i} \; s_{z_i}]^T$. Note, the latter requires 3 parameters to specify the i-th dipole as opposed to 4 parameters for the former. However, for this study, the 4 parameter representation is used since it provided better estimates of the dipole orientation.

23

Fig. 2.1.[b] also shows the distance between a dipole and two different sensors, that is denoted by d_{ji} where j is the sensor number, and i the dipole number.

2.1.2   EEG signal measurement

The mathematical model for the measured EEG signal is derived by using a quasi-static approximation of Maxwell's equations and the Biot-Savart law as presented in [9,10]. This forward model is shown in Eqns. 2.3, and 2.4, where n_j denotes the measurement noise. This model represents the values of measured signals (in μV) that would have been obtained using electrodes located on the patient's scalp and is shown below,

$$f_{j,i} = \boldsymbol{g}_{j,i} s_i \boldsymbol{\mu}_i + n_j \tag{2.3}$$

$\boldsymbol{n} \in \mathbb{R}^{m \times 1}$ represents Gaussian white noise process with some specified covariance. Thus $f_{j,i} \in \mathbb{R}$ is the signal strength of the ith dipole received at the jth sensor and $\boldsymbol{g}_{j,i}$ is given as,

$$\boldsymbol{g}_{j,i} = \frac{1}{4\pi\zeta} \left[\frac{w_{x_j} - l_{x_i}}{d_{ji}^3} \frac{w_{y_j} - l_{y_i}}{d_{ji}^3} \frac{w_{z_j} - l_{z_i}}{d_{ji}^3} \right] \tag{2.4}$$

where d_{ji} shows the distance between the ith dipole and the jth sensor.

Further, denote $\boldsymbol{G}_i \in \mathbb{R}^{m \times 3}$ as the gain matrix for the ith dipole with m sensors, and constant brain conductivity ζ ($\mu S/cm$) [9]. Thus:

$$\boldsymbol{G}_i = \frac{1}{4\pi\zeta} \begin{bmatrix} \frac{w_{x_1} - l_{x_i}}{d_{1i}^3} & \frac{w_{y_1} - l_{y_i}}{d_{1i}^3} & \frac{w_{z_1} - l_{z_i}}{d_{1i}^3} \\ \vdots & \vdots & \vdots \\ \frac{w_{x_m} - l_{x_i}}{d_{mi}^3} & \frac{w_{y_m} - l_{y_i}}{d_{mi}^3} & \frac{w_{z_m} - l_{z_i}}{d_{mi}^3} \end{bmatrix} \tag{2.5}$$

The EEG signals as received by the m sensors are then compactly represented as,

$$\boldsymbol{F}_i = s_i \boldsymbol{G}_i \boldsymbol{\mu}_i + \boldsymbol{n} \tag{2.6}$$

This model illustrates the relationship between the dipole properties and the collected EEG signals, considering the noise of the sample collecting process. Note, $\boldsymbol{F} \in \mathbb{R}^{m \times n}$

To account for the fact that the conductivity of the brain material is non-uniform, we propose a piece-wise constant conductivity to account for the soft matter, as well as the skeletal tissue before the dipole signal is received at the sensor. This is modeled as follows to present a more realistic conductivity:

$$f_{j,i} = \rho_{j,i} s_i \left(\frac{1}{4\pi \zeta_{j,i}} \right) \boldsymbol{g}_{j,i} \boldsymbol{\mu}_i + n_j \tag{2.7}$$

In what follows, each of terms introduced in Eq. 3.1 such as $\zeta_{j,i}$ and $\rho_{j,i}$ will be elaborated upon.

- *Variable conductivity ($\zeta_{j,i}$) within the head model*: It is assumed that a dipole can be located anywhere in the brain (half-sphere head model), and the sensors are located on the patient's scalp. This means the generated signals from dipoles pass through different parts of the head, such as the brain's soft tissue, the spongy bone, the compact bone part, and the skin, to reach the sensors. Since each of these materials have different conductivities, the signal conduction is affected accordingly. In order to model this changing conductivity, the $\zeta_{j,i}$ is modeled as a uniformly distributed random variable between 0.1 and 0.9 all though the head (including the soft parts to the hard parts like the bone).

- *Sensor distribution*: Several methods are available to locate the electrodes on the patient's scalp, usually named by numbers indicating the standard locations. For instance, the two most popular sensor distributions are 10-10 and 10-20 [68]. This study aims to find a precise estimation of the dipole properties, regardless of how the sensors are distributed. In order to fulfill this goal, a random distribution of sensors is considered in this chapter. Note that the sensors are uniformly randomly distributed over the scalp. Fig. 2.3 illustrates a sample of uniform random distribution for 128 sensors.
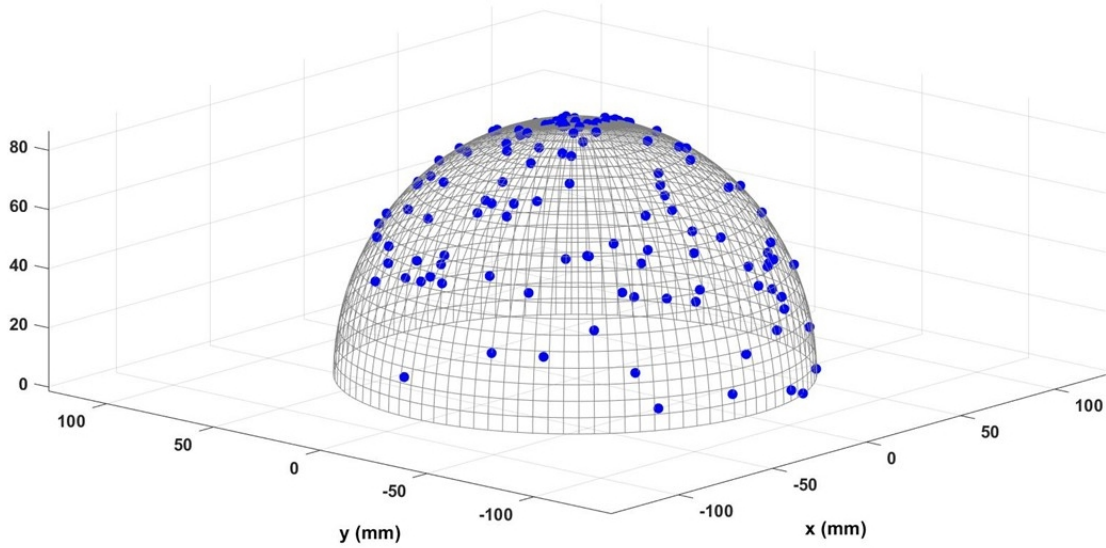
Figure 2.3: Uniform random distribution of sensors located on the hemisphere head model

- *The adjacency of the dipoles to the sensors and varying Received Signal Strength (RSS) as a function of the location of the dipoles with respect to the sensors ($\rho_{j,i}$):* The accuracy of the collected signals is directly related to the distance between the source and the sensor. In this section, the location of sensors is assumed to be uniformly randomly distributed. Thus, the distance between the dipole to each sensor can be varying from 0 (co-located source and sensor) to the brain's diameter (i.e., $2r = 20$ cm in this research). Thus getting closer to the sensor, translates to a better RSS value of the EEG signal. In order to consider this, a distance-based signal strength attenuation term $\rho_{j,i}$ is modeled as follows

$$\rho_{j,i} = -\alpha d_{ji} + \beta \tag{2.8}$$

Where α and β are constants and chosen such that the coefficient $\rho_{j,i}$ lies within 0.01 and 1.0.

26

Note, these coefficients eliminate the effect of weak and noisy data and keep the high strength signals. In order to illustrate this concept, consider the following example. For the closest distance (the dipole is right under the sensor), the collected value will be the same as the real value generated by the dipole, which means the coefficient exactly equals 1.0. With the same approach, for the longest distance (the brain diameter), the collected value will be 0.01 times the real value, which means one can neglect it.

The synthetic signals generated using the aforementioned EEG measurement model are shown in Fig. 2.4.

In this study, to illustrate the effectiveness of the measurement model as well as the estimation algorithm, it is assumed that the dipoles are fixed in orientation and magnitude. The head is modeled as a half-sphere with a diameter of 20 centimeters as it is suggested in [42]. Fig. 2.5 shows a comparison of BESA[1] data, with specific Head Model parameters (conductivities) shown in Fig. 2.5a against that synthesized using our method assuming that ζ is uniformly distributed between 0.2 and 0.4 S/m. The results are in very good agreement. Henceforth, all synthetic data was generated using the proposed mathematical model following this verification.

---

[1]`https://www.besa.de/products/besa-research/features/head-model-selection/`
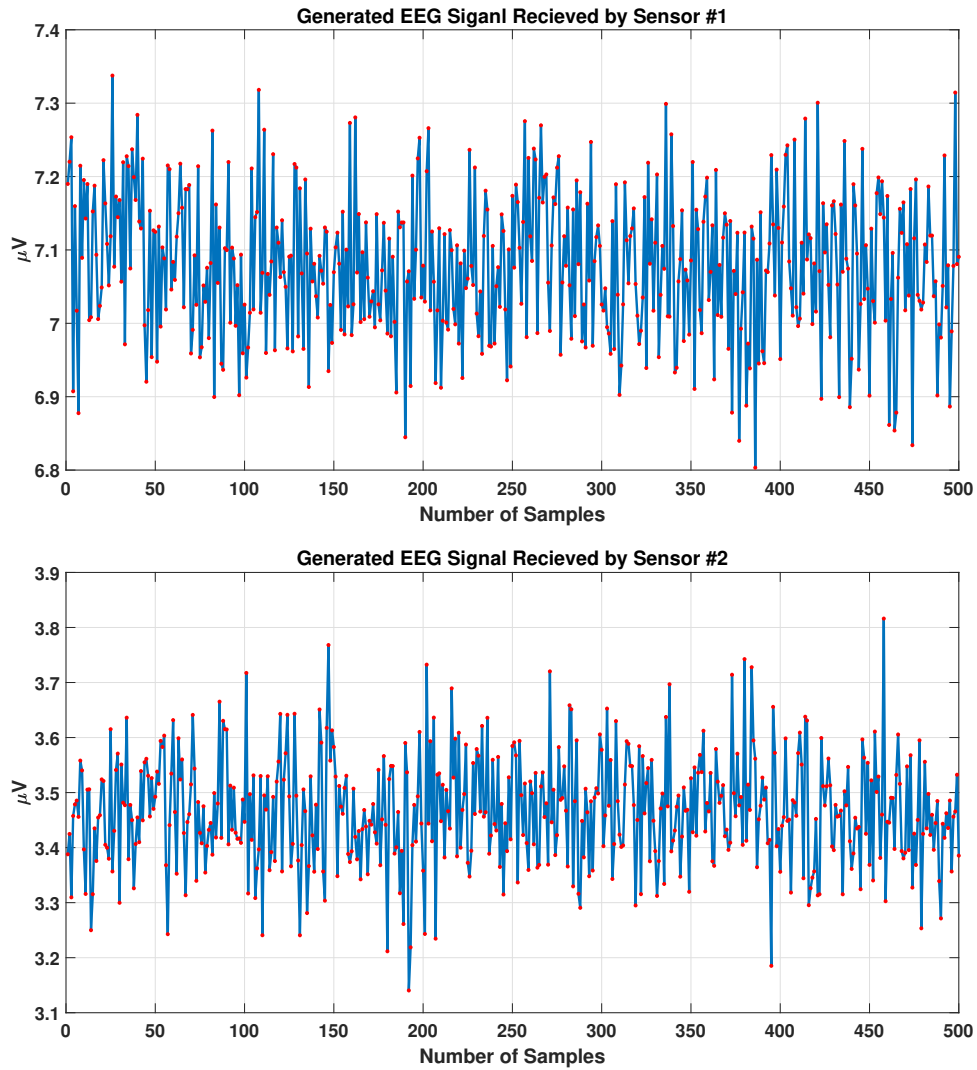
Figure 2.4: Synthetic EEG signals recorded by two different sensors. Signal 1 has a higher mean absolute strength compared to signal 2.
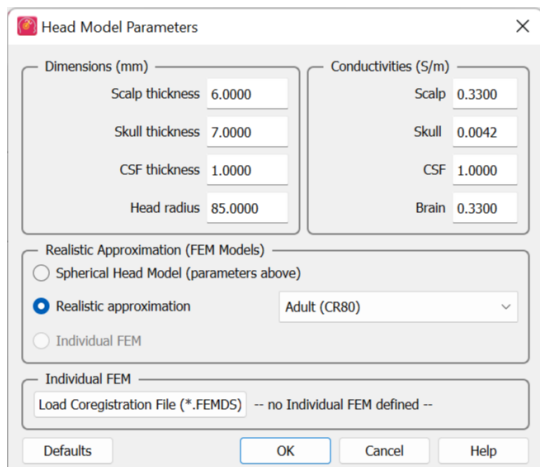
(a)
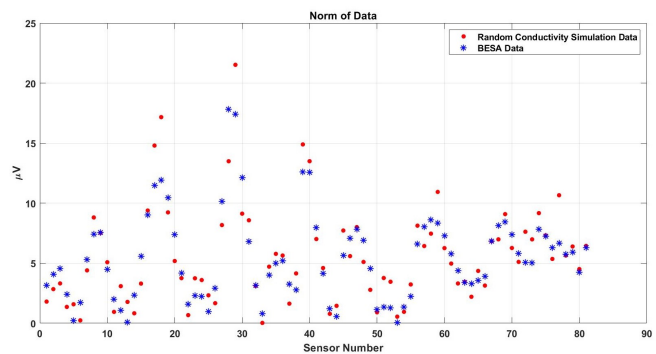
(b)

Figure 2.5: BESA comparison: [a] Model parameters for the BESA data, [b] Comparison of BESA data with our synthetic EEG signal based on random conductivity head model.

2.2 Problem Statement

Succinctly stated, the problem that is solved in this study is as follows. "Assuming multiple dipole sources (n) with fixed orientations and strengths, and given m noisy synthetic EEG signal measurements, we seek to find an accurate estimate of the unknown parameters that characterize the dipoles, such as their distinct locations, orientations, and the strengths of the dipoles using a simple phenomenological measurement model provided in Eq. 2.6". This section presents the **Constrained Nonlinear Least-squares-based Source Characterization (CNLSC)** algorithm to solve the mentioned problem.

2.3 Solution Methodology

The parameters to be estimated for the i-th dipole are denoted compactly as the vector $\boldsymbol{p}_i \in \mathbb{R}^{7 \times 1}$:

$$\boldsymbol{p}_i = [l_{x_i} \ l_{y_i} \ l_{z_i} \ \mu_{x_i} \ \mu_{y_i} \ \mu_{z_i} \ s_i]^T$$

The above-mentioned unknowns, all appear on the right side of the Eq. 2.6. Thus, The inverse problem is solved to obtain the unknown components in the $\boldsymbol{p}$ vector.

Among different approaches to solving an inverse problem, this study chooses an optimization method where the L_2 norm of the estimation error is minimized. The estimation error is defined as the difference of the real measured signals and those predicted by the estimated values of the unknown parameters using the measurement model in Eq. 2.6.

$$\hat{\boldsymbol{p}}_i = \left[\hat{l}_{x_i} \ \hat{l}_{y_i} \ \hat{l}_{z_i} \ \hat{\mu}_{x_i} \ \hat{\mu}_{y_i} \ \hat{\mu}_{z_i} \ \hat{s}_i\right]^T$$

The predicted value of the EEG signal from the parameter estimates is given by,

$$\hat{\boldsymbol{F}}_i(\hat{\boldsymbol{p}}_i) = \hat{s}_i \hat{\boldsymbol{G}}_i \hat{\boldsymbol{\mu}}_i \tag{2.9}$$

The objective of the inverse problem is to minimize the weighted L_2 norm of the measurement residuals, shown as:

$$J = \frac{1}{2} \sum_{i=1}^{i=n} \left(\boldsymbol{F}_i(\boldsymbol{p}_i) - \hat{\boldsymbol{F}}_i(\hat{\boldsymbol{p}}_i) \right)^T \mathbf{W} \left(\boldsymbol{F}_i(\boldsymbol{p}_i) - \hat{\boldsymbol{F}}_i(\hat{\boldsymbol{p}}_i) \right) \tag{2.10}$$

Where, $\mathbf{W}$ is a symmetric weighting matrix. In this study, $\mathbf{W}$ is chosen to be an Identity matrix. The cost function is augmented with the unit norm constraint of the dipole orientation, i.e $\|\hat{\boldsymbol{\mu}}_i\|_2 = 1$.

$$J_a = J + \sum_{i=1}^{i=n} \left(\lambda_i (\|\hat{\boldsymbol{\mu}}_i\| - 1) \right)$$

where λ_i is the Lagrange Multiplier corresponding to the ith dipole orientation constraint in the equation above. Note, the procedure to solve this problem would be to set up the necessary conditions (from the gradient of the cost), and determine an update for the parameters from one iteration to the next using the gradient and the Hessian (second derivative of the cost function with respect to the decision variables), and the application of the Karush Kuhn Tucker (KKT) conditions. These procedures are built into a nonlinear solver such as 'fmincon' in the Optimization Toolbox of MATLAB, which allows for an explicit specification of the cost to be minimized, nonlinear constraints that the decision variables satisfy, as well as any bounds on the decision values that need to be respected. The results obtained are discussed in the next section.

2.4   Simulation Results

Before presenting the detailed simulation results, a thorough sensitivity and characteristics analysis of the solution to the inverse problem with regards to the number of sensors to be employed and the number of samples required to reliably provide a convergent solution was performed. The signals generated for the analysis have an average Signal to Noise Ratio (SNR) of about 20 dB.

2.4.1 Model Sensitivity and Characteristics Analysis Using Synthetic Data and the Spherical Head Model

Table 2.1 provides the results of the simulation in this study. As shown in the table, the source localization process uses an initial guess and iteratively converges to the actual values. As shown in table 2.1, the estimated value is very accurate for all three selected dipoles, indicating that the source localization algorithm is consistent. In addition to this table, Fig.2.6 visually illustrates the estimation result and the random distribution of the sensors on the scalp.

Table 2.1: Source Localization result for Multi-dipole case where three dipoles are active simultaneously. The simulation is for 250 samples and 36 sensors.

Dipole Param.	Dipole #1			Dipole #2			Dipole #3		
	Real Value	Initial Guess	CNLSC Result	Real Value	Initial Guess	CNLSC Result	Real Value	Initial Guess	CNLSC Result
$l_x(cm)$	2.25	3	2.25	2.37	1	2.37	2.18	1	2.18
$l_y(cm)$	0.82	2	0.82	1.37	-3	1.37	2.18	0	2.18
$l_z(cm)$	6.58	3	6.58	7.52	3	7.52	8.46	4	8.46
μ_x	0.32	0	0.32	0.29	0.43	0.29	0.24	0.43	0.24
μ_y	0.12	0	0.12	0.17	-0.75	0.17	0.24	0.25	0.24
μ_z	0.94	1	0.94	0.94	0.50	0.94	0.94	0.87	0.94
$s(A.cm)$	0.1	0.3	0.10	0.2	0.3	0.20	0.3	0.1	0.3

To study the sensitivity of the estimation algorithm to the number of sensors and samples, the simulation is performed for different numbers of sensors, and samples for three different dipoles, and the results are shown in Figs. 2.7 - 2.9. These 3D plots show the changes in the total error percentage of the estimated values in terms of increasing number of sensors and samples simultaneously. Note that the average error of all seven unknowns, including the location, orientation, and magnitude, is presented in these figures. As expected, by growing the number of samples and sensors, the amount of collected data increases. Consequently, the estimation of unknown values is more accurate. Moreover, one can determine the least value of

32
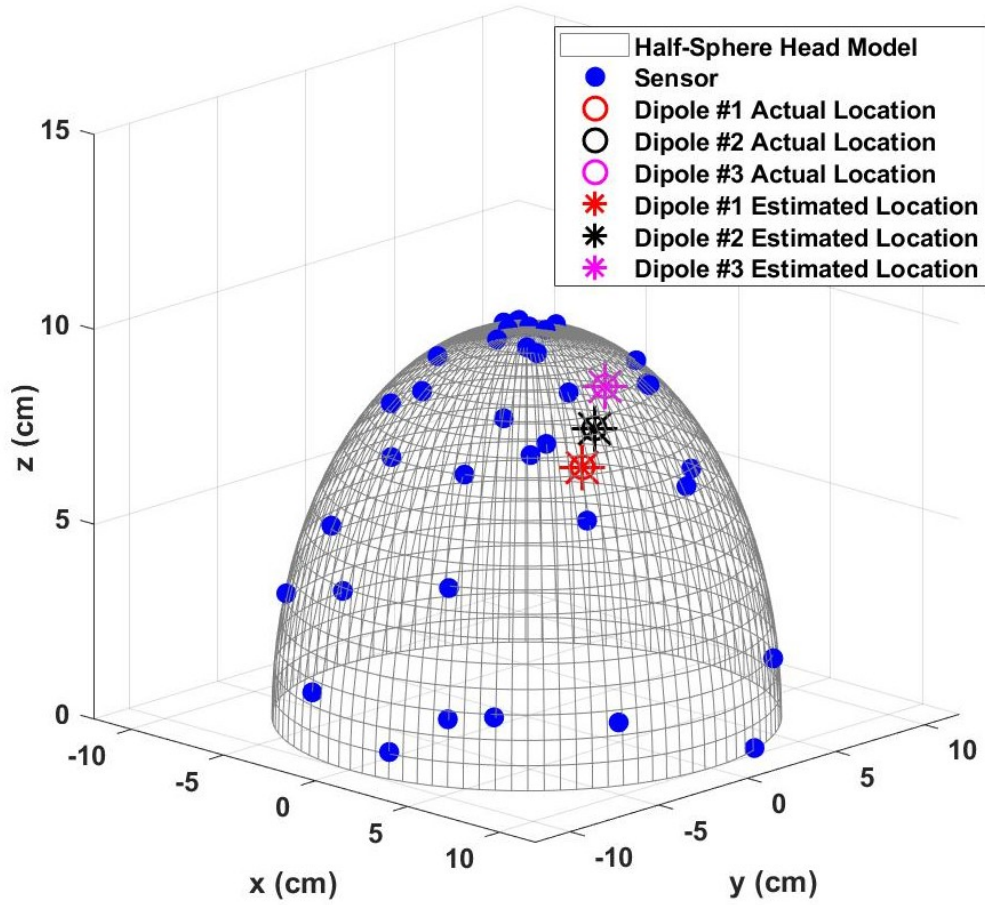
Figure 2.6: Visual representation of estimation result associated with numerical results provided in Table 2.1

error and the corresponding number of samples and sensors. For instance, *in this simulation, 48 sensors and 350 samples gave us the least error percentage.* It is essential to mention that the error might be higher than expected in a few cases due to the random distribution of sensors on the scalp. In other words, in these cases, the number of sensors close to the dipoles is less than usual, and as a result, the collected data is not reliable enough.

In order to study the effect of the distance between dipoles and sensors, three different locations are chosen for the simulation, one deeper in the brain, one closer to

the scalp and sensors, and one dipole is chosen somewhere in between the locations of the other two. Based on the estimation algorithm described in the previous section, sensors receive weaker signals from the deeper dipoles. This leads to a higher amount of estimation error for the deeper dipoles, i.e. dipole # 1 in this study. Considering this information regarding the location of the dipoles, one can interpret Figs. 2.7 to 2.9 more accurately. This case can be observed by comparing the magnitude of the estimation error for each dipole from these three figures.
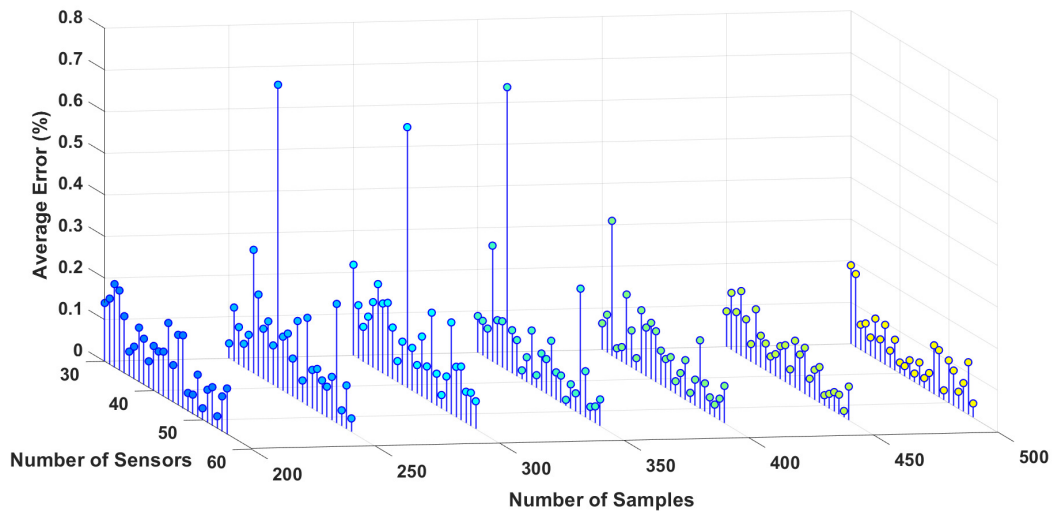
Figure 2.7: Error percentage of estimated variables in terms of number of sensors and samples, Dipole number 1

Figs. 2.10-2.14 present the error percentage for estimating each variable in the parameter vector $\boldsymbol{p}_i$ separately, where the error bar is the confidence interval value. It was mentioned previously that the electrodes are located randomly on the patient's scalp to make sure this simulation is working correctly regardless of the sensors' location. However, in some cases, the sensors could be located somewhere far from the dipole, and as a result, the collected data is noisier and weaker. Clearly, this
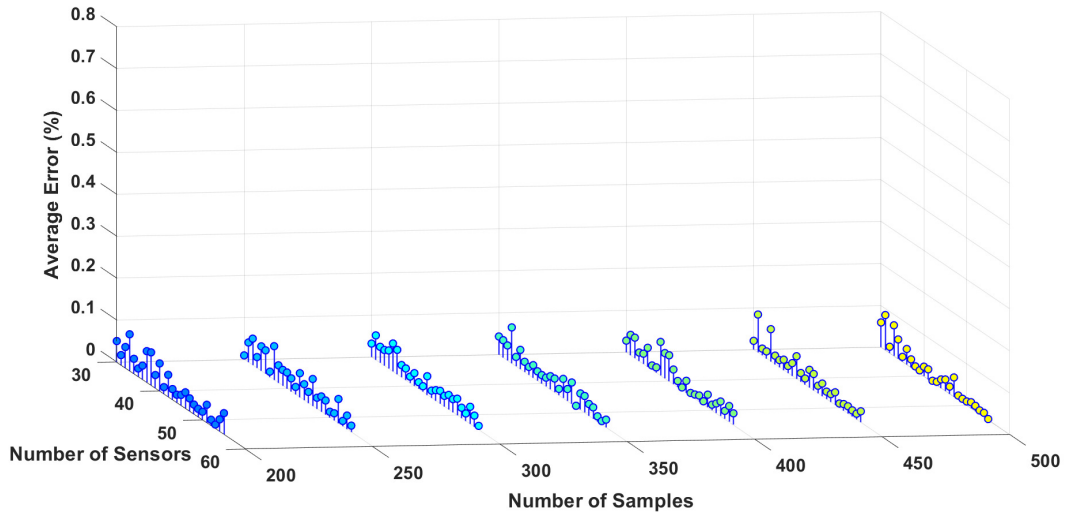
Figure 2.8: Error percentage of estimated variables in terms of number of sensors and samples, Dipole number 2
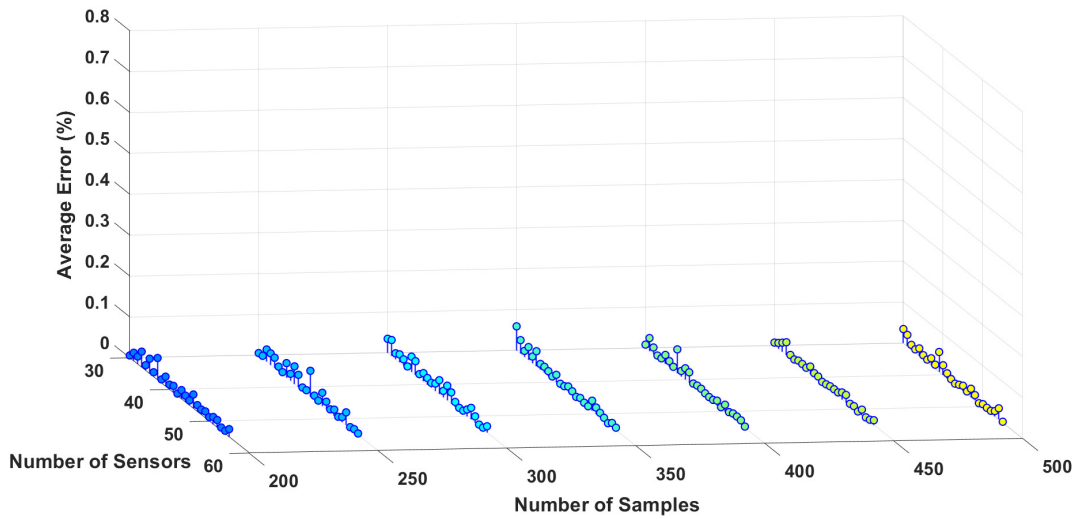
Figure 2.9: Error percentage of estimated variables in terms of number of sensors and samples, Dipole number 3

happens when the number of sensors is too low and they can not cover the scalp adequately. As a result, the confidence intervals for the low number of sensors are more significant. In other words, if the small number of sensors are located in some place near the dipoles, the result is still acceptable.

Figs. 2.10-2.12 show the error percentage for each variable. There is a lower error for each variable in terms of the number of sensors. Thus it is not possible to choose the optimum number of sensors using just the error in each variable. To address this problem, an average error of all the parameters is studied as shown in Fig. 2.13 which provides a more robust estimate for the optimum number of sensors required. We note, (a) the minimum error percentage occurs when around 19 sensors are used; (b) the error percentage reduces as the number of sensors increase (in general). This occurs because higher number of sensors cover more of the scalp area, and as a result, the collected EEG data has more information. To summarize then, Fig. 2.13 represents a converged and consistent value of error after a specific number of sensors (20 sensors) are used. This means a specific amount of collected data is enough to make the model equations well-defined, and the estimation problem well-posed to find a consistent estimate. Thus, one can use the minimum number of sensors as indicated by these numerical experiments and conduct a simpler actual experiment (in terms of cost and the computational burden). In order to further test this hypothesis, this simulation was performed using up to 100 sensors, and the result is provided in Fig. 2.14.

It was discussed previously that 19 sensors would be good enough for this study to estimate the dipole properties. Similarly, a sensitivity study with respect to the number of samples is carried out. Fig. 2.15 shows the changes in error percentage by increasing the number of samples. It was determined that 400 samples were sufficient to estimate all the dipoles' parameters.

The effect of distance between the sensor and a dipole is one of the important considerations in this study. In order to see this, two different sensors are considered, one closer to a specific dipole, and the other one far from the same dipole, as it is shown previously in Fig. 2.1. The collected EEG signal from these two dipoles is
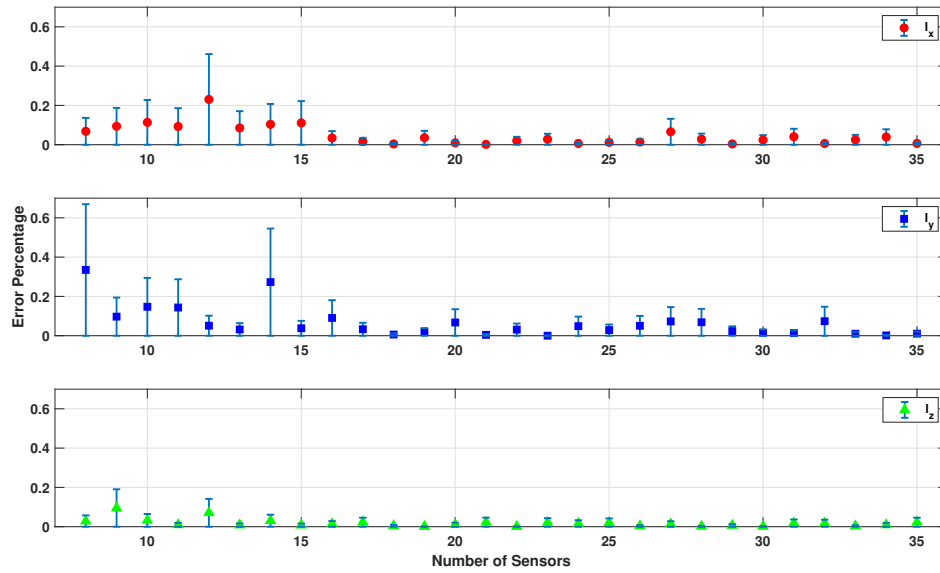
Figure 2.10: Error percentage of a dipole's location for different sensors and 500 samples
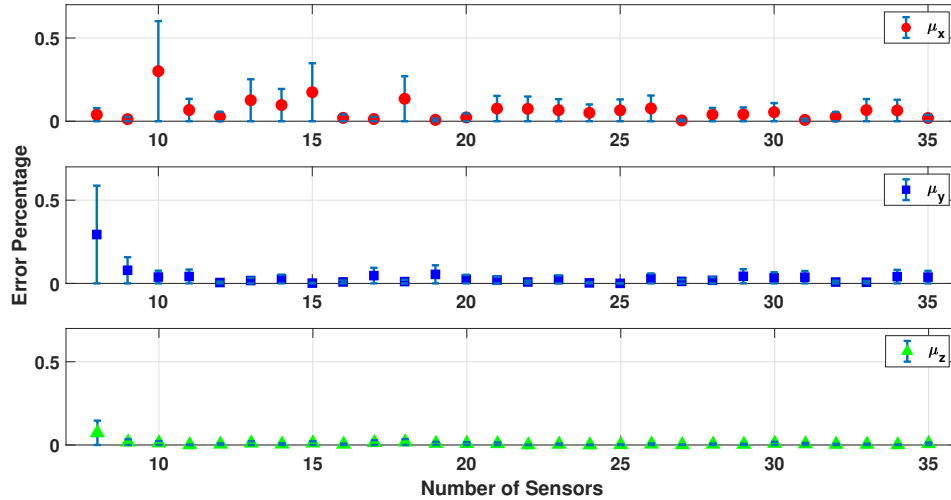
Figure 2.11: Error percentage of a dipole's orientation for different sensors and 500 samples

shown in Fig. 2.16. As seen from this figure, the sensor collected a stronger EEG
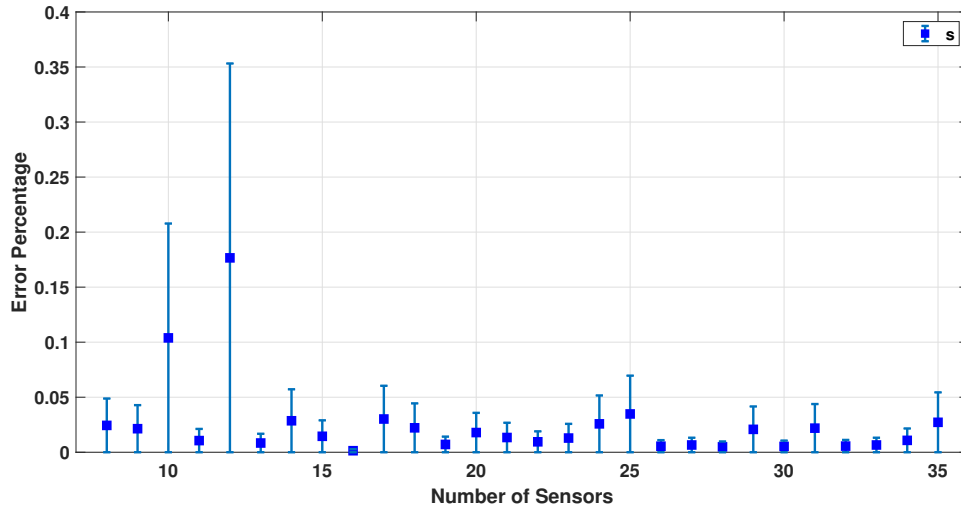
Figure 2.12: Error percentage of a dipole's magnitude for different sensors and 500 samples
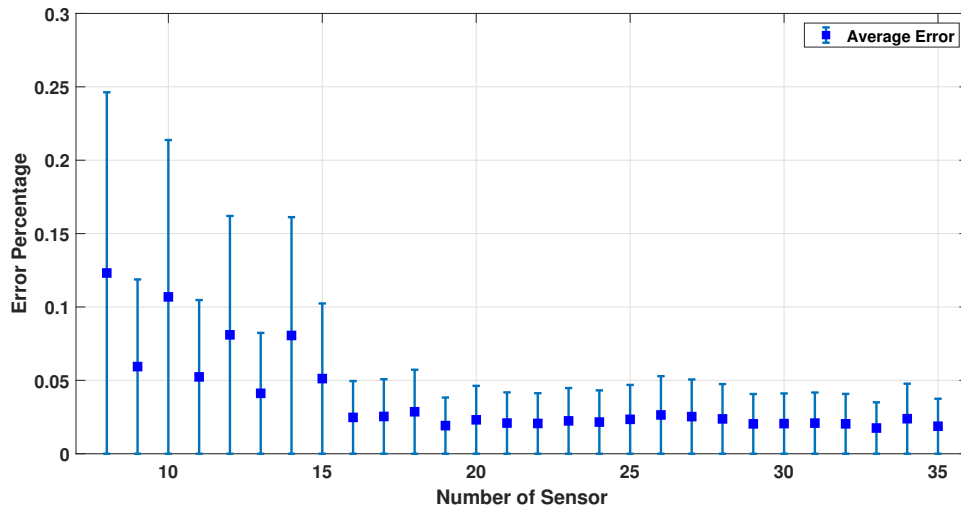
Figure 2.13: Average error percentage for different sensors and 500 samples

signal from the closer dipole (shown in blue) rather than the dipole far from the sensor (shown in red).

In conclusion, the proposed mathematical model for the dipole is very general and captures the key features of signal propagation from the source to the sensor. This
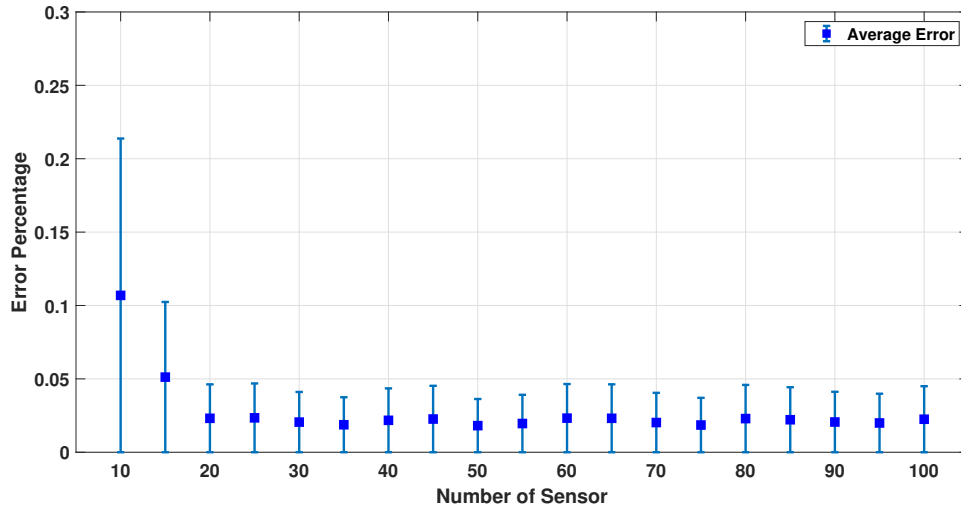
Figure 2.14: Average error percentage for different sensors (10 to 100) and 500 samples
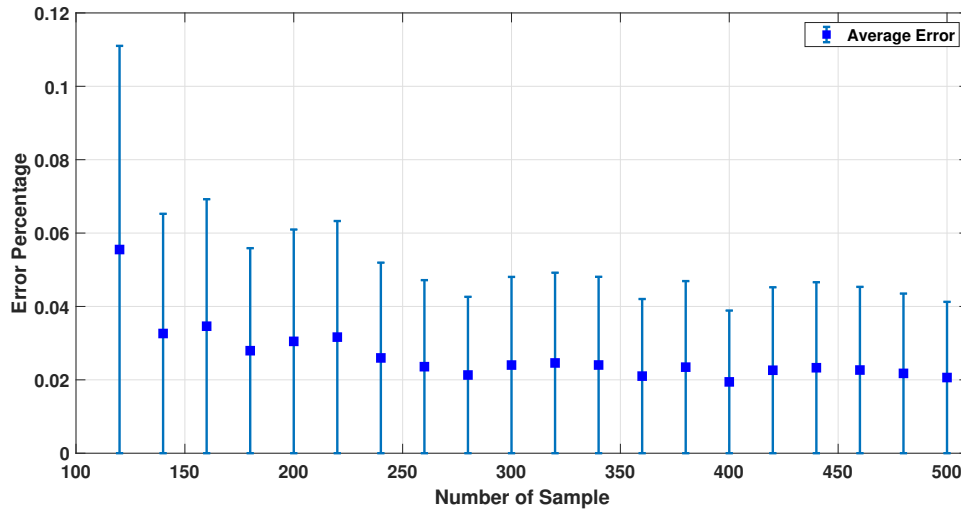
Figure 2.15: Error percentage for different number of samples and 19 sensors

simple model allows significant flexibility in terms of including medium dependent conduction, signal strength variation due to distance, as well as other un-modelled noise.
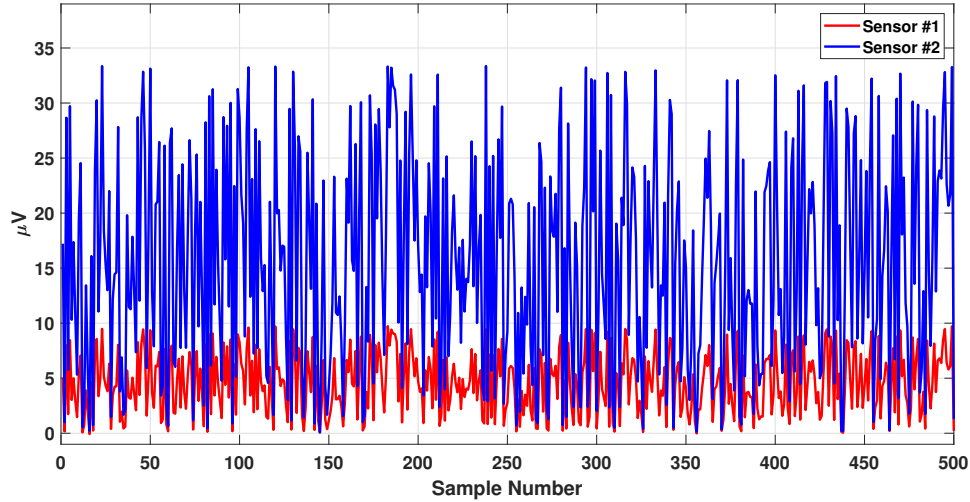
Figure 2.16: Generating EEG signals recorded by two different sensors

2.4.2 Model Performance for Source Localization Using EEGLAB

In this study, the half-sphere head model is used to simplify the simulation. Also, different parts of the brain's conductivity are assumed to be random numbers between 0.1 to 0.9 as mentioned before in section II.

In order to check how precise these assumptions are, one can compare the derived results provided by the present algorithm with the generated results from available open source software such as BESA, Cartool, EEGLAB, etc.[69]. In this study, the EEGLAB [70] software is chosen, with several options to choose the head model. The MNI head model is one of the most accurate ones and selected in this study to compare with the spherical head model.

The first step in using EEGLAB is to import the same generated signal used in the previous section. The location of sensors in the MATLAB-generated EEG signal are the standard 64 locations of BioSemi (known as 10-20 standard system), and the same locations will be considered in EEGLAB. The MNI head model in EEGLAB has a head radius of 85 mm. Note that, for having a more accurate comparison, the

head model in the previous sections that considered a half sphere is modified to an 85 mm radius as well.

Note, prior to the source localization step using clinical data in EEGLAB, the user has to reject certain data by visual inspection. *The CNLSC algorithm (discussed previously) on the other hand does not require this manual step.* Further, since only dipole activities generate the available EEG data, there is no need to denoise or cancel any other 'artifact' in this case. The DIPFIT toolbox is used in EEGLAB to generate the source localization results. This MNE-based toolbox is designed by Robert Oostenveld and is available at Fieldtrip [71]. Applying the DIPFIT function in EEGLAB gives the dipole's location in Talairach coordinates, which is shown in Fig. 2.17a. Furthermore, Figs. 2.17a and 2.17b are located next to each other to show the similarity of the source localization from the CNLSC algorithm and the result obtained from EEGLAB. Given the differences between these two approaches and those associated with the representations (Talairach coordinates vs the Cartesian coordinates), the results are in close agreement. Besides the visual presentation of the results, Table 2.2 provides the numerical results for three dipoles located in the head model. The error mentioned in this table is the distance between the actual source and the source localization result in mm, which is defined in Eq. 2.4.2.

$$\text{error}_i = \sqrt{(l_{x_i} - \hat{l}_{x_i})^2 + (l_{y_i} - \hat{l}_{y_i})^2 + (l_{z_i} - \hat{l}_{z_i})^2}$$

Note that for all three dipoles, the error is significantly lower for the present algorithm compared to the EEGLAB result. We thus verify that the Constrained Nonlinear Least-squares-based Source Characterization (CNLSC) method's performance agrees well with that produced by EEGLAB.

41
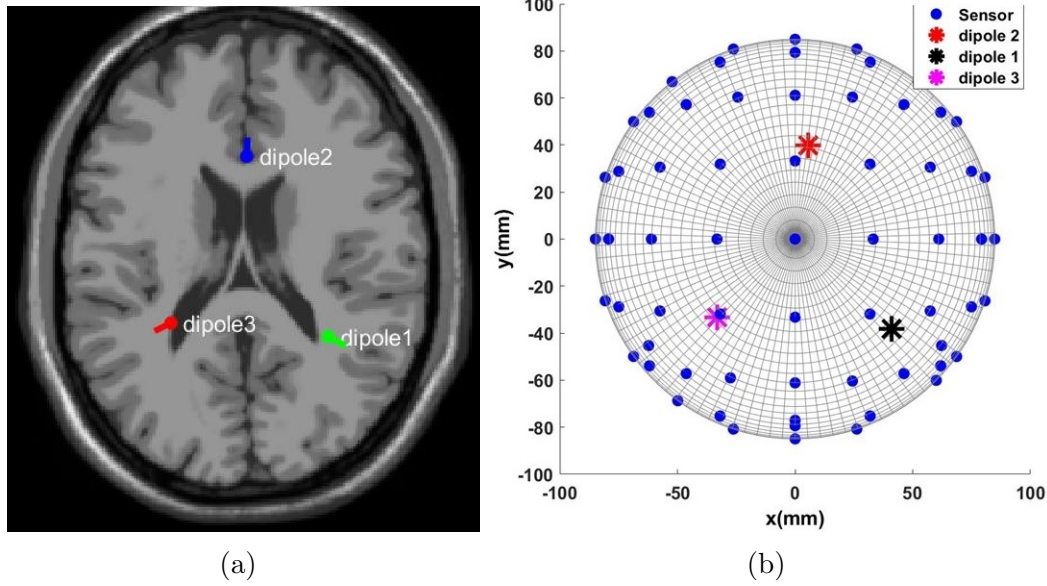
Figure 2.17: (a) Multiple dipoles' source localization result from EEGLAB where the Talairach coordinates are: dipole 1 (32,-40,72), dipole 2 (1,26,65), dipole 3 (-27,-35,73). (b) Multiple dipoles' source localization result from CNLSC algorithm

Table 2.2: Numerical Results

Dipole #1					
Talairach Coord.	Real Value	CNLSC Result	CNLSC Error (mm)	EEGLAB Result	EEGLAB Error (mm)
X (mm)	9.11	9.13		8	
Y (mm)	32.07	32.06	0.03	53	22.24
Z (mm)	38.54	38.52		46	
Dipole #2					
X (mm)	39.96	40.01		59	
Y (mm)	-54.43	-54.39	0.08	-53	19.92
Z (mm)	34.37	34.27		40	
Dipole #3					
X (mm)	-15.01	-15.01		-34	
Y (mm)	-29.78	-29.78	0	-17	24.81
Z (mm)	59.42	59.42		69	

2.4.3 Characteristics Analysis Using the Clinical Data and the MNI Coordinates

Now that the efficacy of the CNLSC algorithm has been proved in the previous sections, one can assess this algorithm using clinical sample data. Therefore, a sug-

gested dataset from EEGLAB is used in this section [67,72]. This dataset belongs to a visual attention task. In this task, each event is a three seconds time interval where the subject should press a button right after seeing a square on a screen in front of them. Given the quality of the dataset and the presence of bad quality signals, it is suggested to select good quality time intervals rather than using the whole dataset. Thus, in this study, two different time intervals are selected to quantify the source localization algorithm. As illustrated in Fig. 2.18, one of the selected events is from 113 to 116 seconds. The other data set, which is not shown here, is selected from 146 to 149 seconds.
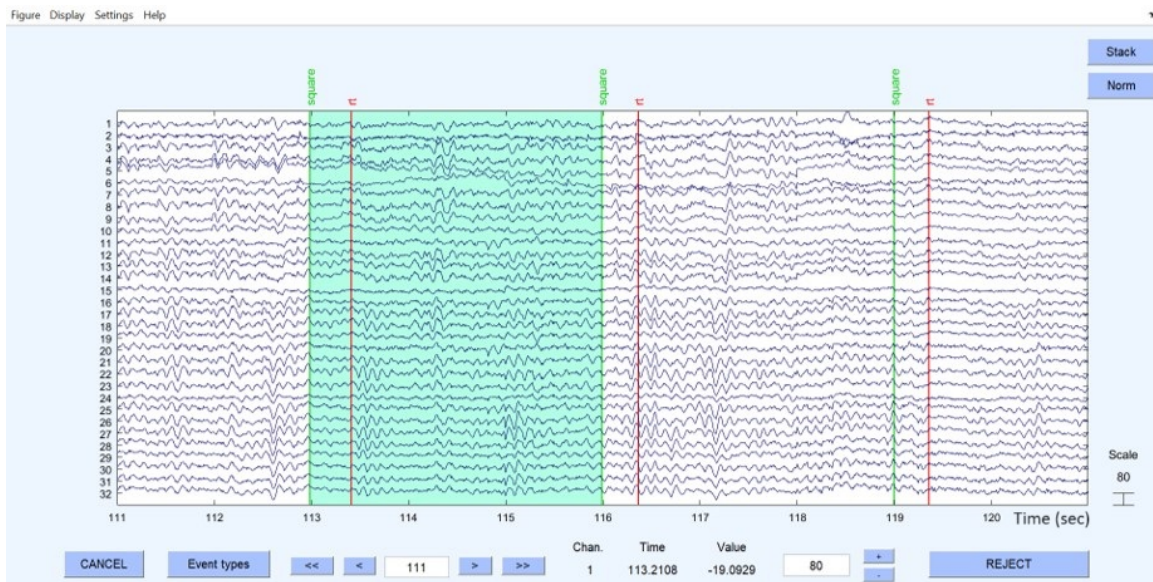
Figure 2.18: Selected time range from the original data set

The selected events are utilized to generate the source localization results on both EEGLAB software and the introduced algorithm. The EEGLAB source localization algorithm suggests the number of dipole locations to be as many as the channel numbers. In other words, for this specific data set that was recorded by 30

EEG signals, EEGLAB found 30 possible dipoles that generate this signal. However, only the results with Residual Variances (RV) less than 15% are acceptable according to EEGLAB [73]. The residual variance in EEGLAB software is defined based on matching the dipole projection to the EEG electrodes. In other words, the variance of the undefined EEG signal generated from the estimated dipole (using the forward model) is called the Residual Variance. Based on this definition, it is also important to mention that smaller numbers of RV indicate the most accuracy, and the results are more reliable.

Figs. 2.19 and 2.20 represent the source localization results for the event that started at 113 seconds and finished at 116 seconds. Fig. 2.19 illustrates all the dipole estimations simultaneously. Given this general presentation of results, one can see the similarity between the EEGLAB result and the introduced algorithm result. Note that, as mentioned earlier, Fig. 2.19(b) is the general result by EEGLAB where all the dipole estimations are not necessarily correct. Fig. 2.19(c) is the final result where any estimation with the RV over 15% is filtered out.

EEGLAB usually utilizes an MRI scan to show the source localization result, making the comparison less convenient. This suggests providing another method to compare the results, and Fig. 2.20 is provided to compare the dipole estimations individually in the same brain map using the Talairach coordinates.

Among 24 dipoles from EEGLAB results, there are 18 similar results available from the present algorithm. The average distance of the EELAB estimation to the CNLSC algorithm's result for these 18 dipoles is only 17.7 mm, and the standard deviation is 7.4 mm. This result clearly illustrates the accuracy of the introduced algorithm when using the clinical data.

Similar to the sample data for the $113 - 116$ second time interval, Fig. 2.21 and 2.22 illustrate the source localization result for the $146 - 149$ second time interval.

It should be noted that for this time interval, 27 out of 30 dipole estimations from EEGLAB are acceptable with RV less than 15%. Also, the number of similar results from the present algorithm is 19 dipoles.

Finally, the algorithm is also tested on clinical data collected from a patient with an active seizure case. The Temple University Hospital provides the EEG data used in this section as their open-source database [74]. This data is collected by 19 EEG sensors with the international 10–20 EEG electrodes as shown in Fig. 2.24.(b).

After applying the EEG source localization to the seizure EEG data, the comparison in Fig. 2.23 shows that the EEGLAB provides 19 estimated dipoles, and only four have RV<15%. However, the CNLSC algorithm results in 35 dipole estimations, including the four dipole results from EEGLAB. Fig. 2.25 presents the four similar results compared individually.

Given more significant number of dipole estimations from MATLAB simulation compared to the EEGLAB, the accuracy of this result is illustrated by providing the channel data. As shown in Fig. 2.24, The highest brain activity occurs around sensors Fp1, Fp2, and F3, which matches both the EEGLAB and MATLAB simulation result. On the other hand, there are other channels with noticeable brain activity, such as Cz, C3, Pz, and P4. This means there could be other sources of brain activity around the central area, even though they are not as strong as the frontal head area. These sources are also discerned by the CNLSC algorithm's result as is shown in Fig. 2.23.(a). In other words, the introduced algorithm is more sensitive to all the brain signals and covers a broader range of source localization.

(a) Matlab Simulation Result using CNLSC algorithm (b) EEGLAB Result, All Estimations (c) EEGLAB Result, RV<15%
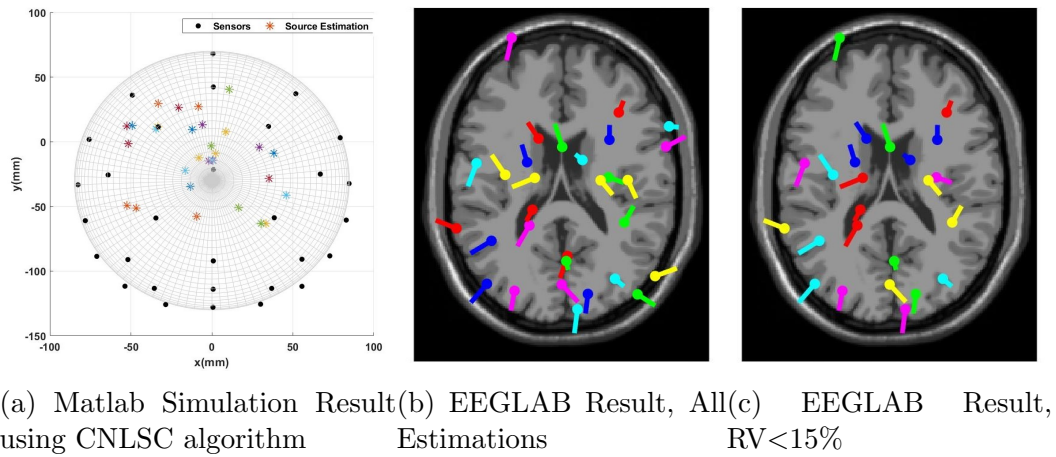
Figure 2.19: The source localization result from the proposed algorithm (CNLSC) vs EEGLAB
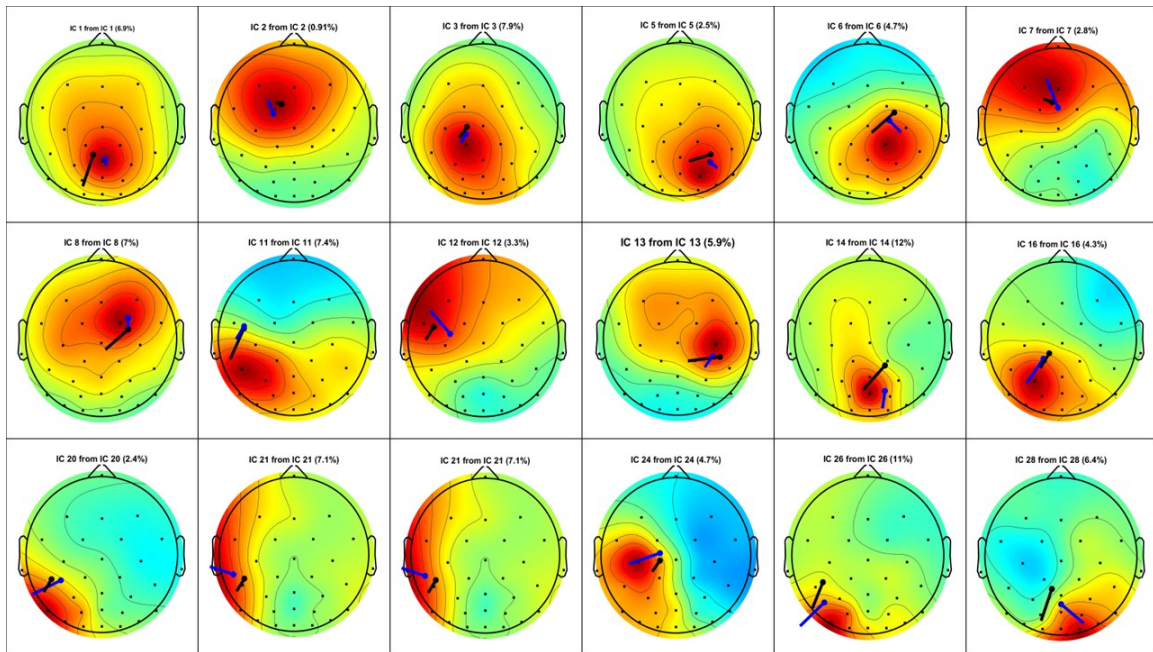
Figure 2.20: Multiple dipoles' source localization result from the proposed algorithm (CNLSC)

(a) CNLSC Algorithm's Result (b) EEGLAB Result, All(c) EEGLAB Result,
Estimations   RV<15%

Figure 2.21: The source localization result from the CNLSC algorithm vs EEGLAB
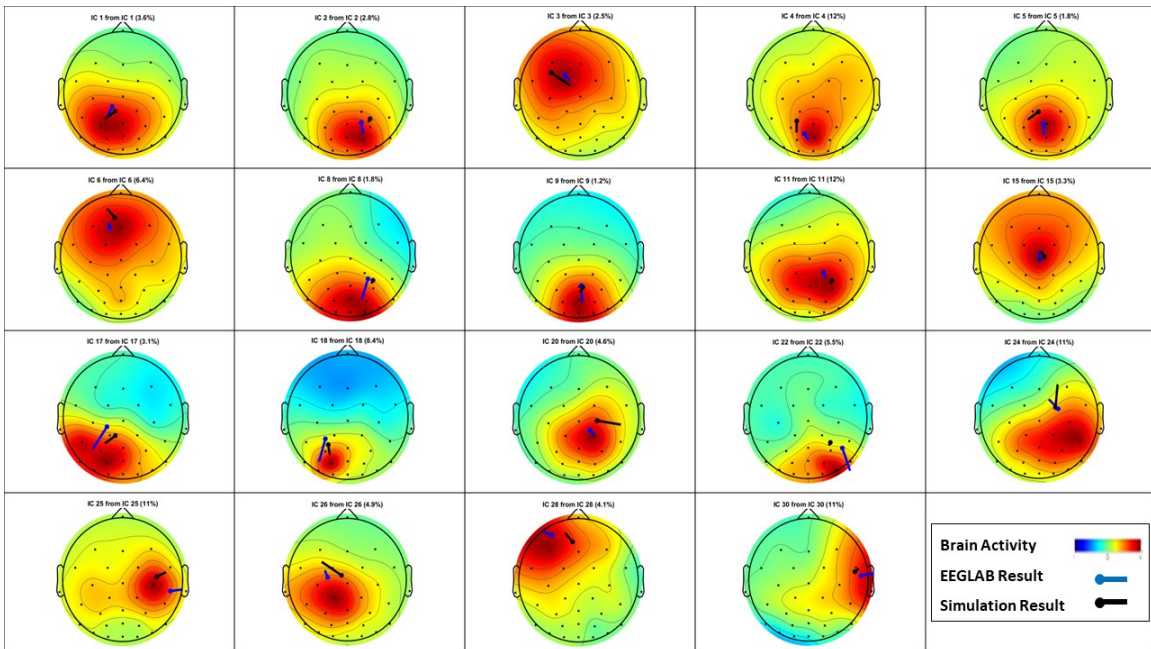
Figure 2.22: Multiple dipoles' source localization result from the CNLSC algorithm

47

(a) CNLSC Algorithm's Result (b) EEGLAB Result, All (c) EEGLAB Result,
                                   Estimations   RV<15%
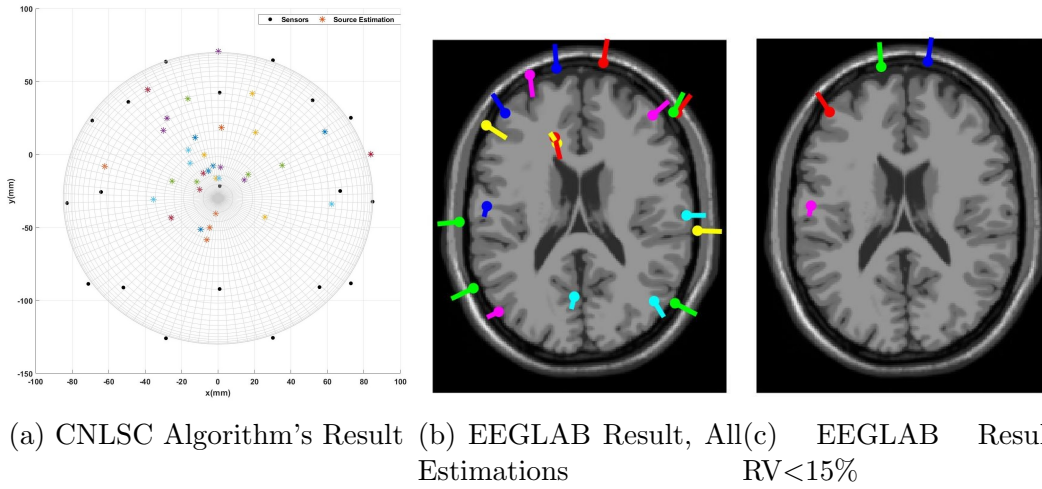
Figure 2.23: The source localization result from the CNLSC algorithm vs EEGLAB

(a) Channel Data   (b) Channel Location
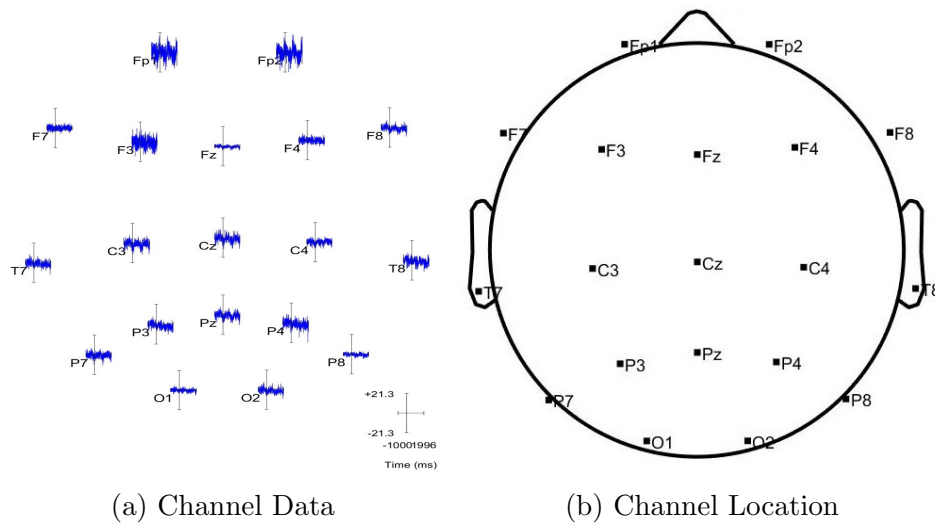
Figure 2.24: The Event Related Potential (ERP) data is shown for each channel which helps to validate the source localization result
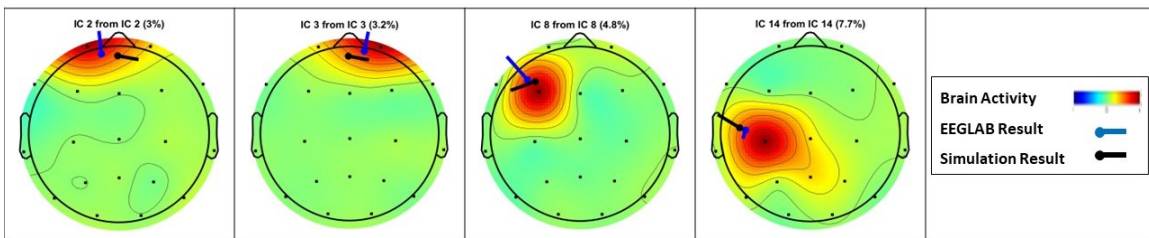
Figure 2.25: Multiple dipoles' source localization result from the CNLSC algorithm

48

2.5   Statistical Analysis of Initial Guess Impact on Estimation Result

As mentioned in previous sections, the CNLSC algorithm needs an Initial Guess (IG) for all seven unknowns to start the estimation process. Therefore, the IG is picked randomly for each source identification problem. This section aims to statistically analyze the relation between the IG and the estimation result. To quantify this relation, the synthetic EEG data that is generated by three dipoles, presented in Fig. 2.6 is utilized.

In order to consider various IG cases, the Latin Hypercube Sampling (LHS) is employed to generate the Monte Carlo simulation. Unlike the uniform distribution, LHS prevents any clustering of sample points in a certain region by dividing the desired range into intervals and ensuring that the sample points are picked from each interval. This technique provides more unique data points while maintaining an even distribution.

To implement the LHS, one must first define a range from which to select the IGs. Regarding the dipole's location Cartesian coordinates, we assume a range of $2\sqrt{3}cm$ around the actual dipole's location, as expressed by Eqn. 2.11. Moreover, the orientation's IG is selected approximately 10 degrees away from the actual dipole's orientation. Lastly, the magnitude is chosen within ± 1 nA/m of the actual dipole's magnitude. Fig. 2.26 is an illustration of the LHS-generated IGs for the location, which are inside a sphere with the radius of $2\sqrt{3}cm$ around the actual dipole's location.

$$
\begin{aligned}
\hat{l}_x &\in [l_x - 2, \quad l_x + 2] \\
\hat{l}_y &\in [l_y - 2, \quad l_y + 2] \\
\hat{l}_z &\in [l_z - 2, \quad l_z + 2]
\end{aligned}
\tag{2.11}
$$

As illustrated in Fig. 2.27, the average estimation error for all seven parameters is less than 0.3%. These results are generated by using 20 Monte Carlo simulations.
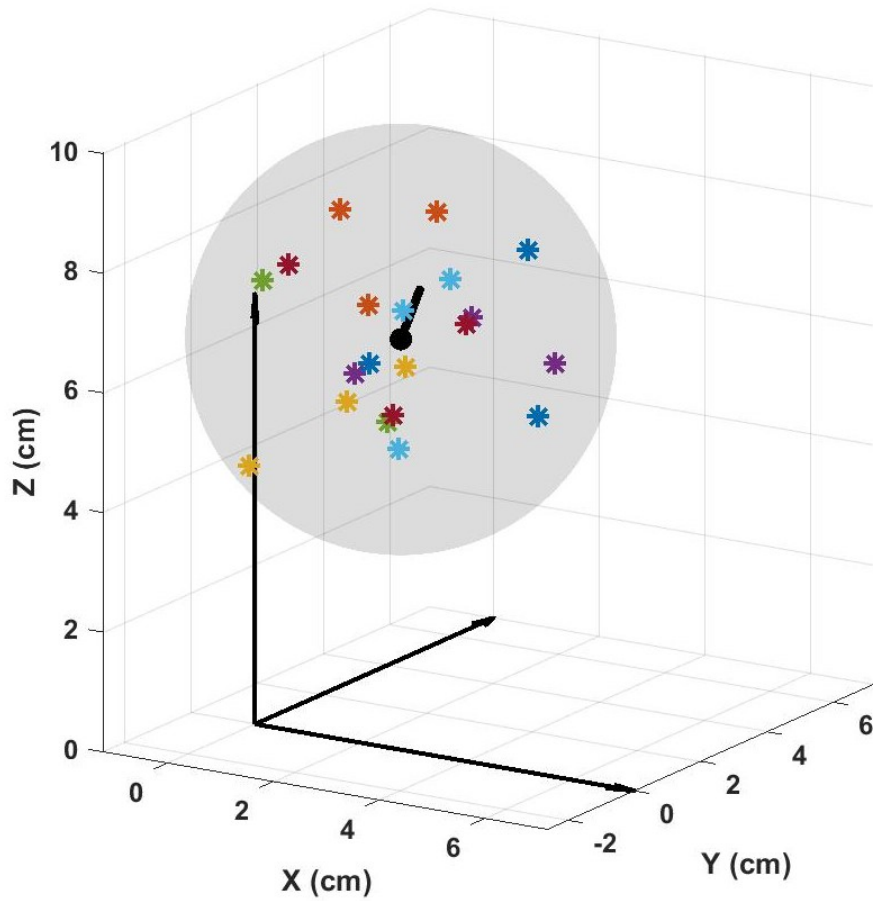
Figure 2.26: An illustration of initial guesses (colorful stars) within the desired range (gray sphere) around the actual dipole's location.

Moreover, The error bar shows the standard deviation, and the red dot represents the average error for each parameter. In conclusion, the source identification result is robust to a specific range of initial guess.
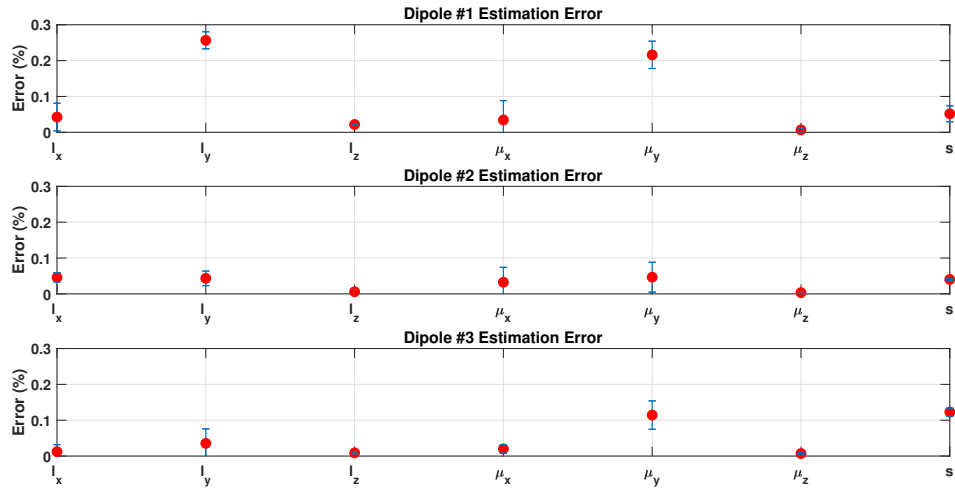
Figure 2.27: Estimation error result generated by 20 Monte Carlo simulations. The error bar presents the standard deviation, and the red dot denotes the average error.

2.6 Conclusion

This study introduces a constrained nonlinear least-squares algorithm to estimate the dipole properties based on the collected EEG signals. The mathematical model for a signal from the dipole is shown to be very flexible and includes features that model piece-wise conductivity, varying Received Signal Strength (RSS), and random sensor distribution on the scalp. This model flexibility enables one to solve the inverse problem for many different head types and/or numbers or sensors and samples. To give an illustration of this fact, this algorithm is applied to two different types of EEG data: 1) Synthetic data generated by the forward model; and 2) Clinical data. The results emphasize the accuracy and performance of the present algorithm for both EEG signal categories. The source localization error for the synthetic data is less than 0.1 percent. In the case of testing the clinical data, this algorithm works as accurately as EEGLAB, which is illustrated in the figures. The results also show that the presented algorithm performs extremely well for the localization of multiple

dipoles and is verified with the results obtained from EEGLAB. Notably, the introduced algorithm can be more sensitive to different sources in the head model. As a result, for some cases, such as the seizure data utilized in this study, the proposed source localization algorithm can find more active dipoles compared to EEGLAB. Future work will focus on optimizing the number of sensors further, decreasing the computation load of source localization algorithms where the FEM and BEM are used, and prototyping the algorithm on a chip that can be embedded in an EEG helmet.

2.7   Future Work

As mentioned earlier, the Constrained Nonlinear Least-squares-based Source Characterization (CNLSC) algorithm employs the random conductivity head model to reduce the computation complexity. This feature helped to expand and develop devices that can analyze real-time EEG data. For instance, a helmet that has embedded EEG sensors can monitor neural activity and the brain condition continuously. In case of any brain injury or abnormal neural activity, this helmet will send an error to the person who wears it. This type of helmet can be highly functional for specific situations, such as football and boxing, where brain injury is common.

As a step toward making such a helmet, we have made a new experimental setup as illustrated in Fig.2.28. In this setup, EEG sensors are located on the scalp to measure the EEG data. After passing the data to the AD converter, it is transferred to a microprocessor, which is a Raspberry Pi model 4b in this case. This microprocessor analyzes the EEG data instead of the PC/laptop. To open and read the data recorded by EEG sensors, Raspberry Pi uses BioSemi software. Moreover, the MATLAB code introduced in this chapter is converted to Python, so the Raspberry Pi 4b microprocessor can utilize it to analyze the data. In this Python code, instead of using the

MATLAB function "*fmincon*," the "*scipy*" library is called to employ the "*minimize*" function. Finally, the microprocessor generates the EEG source identification results and displays them on the attached screen, as illustrated in Fig.2.28. The results generated by this setup are identical to the MATLAB source identification code, which confirms the new setup efficiency.

In the future, this setup can be reduced to a single microprocessor attached to the back of the helmet. This way, the subject wearing the helmet can do daily work and freely move with this helmet, which makes it more functional.
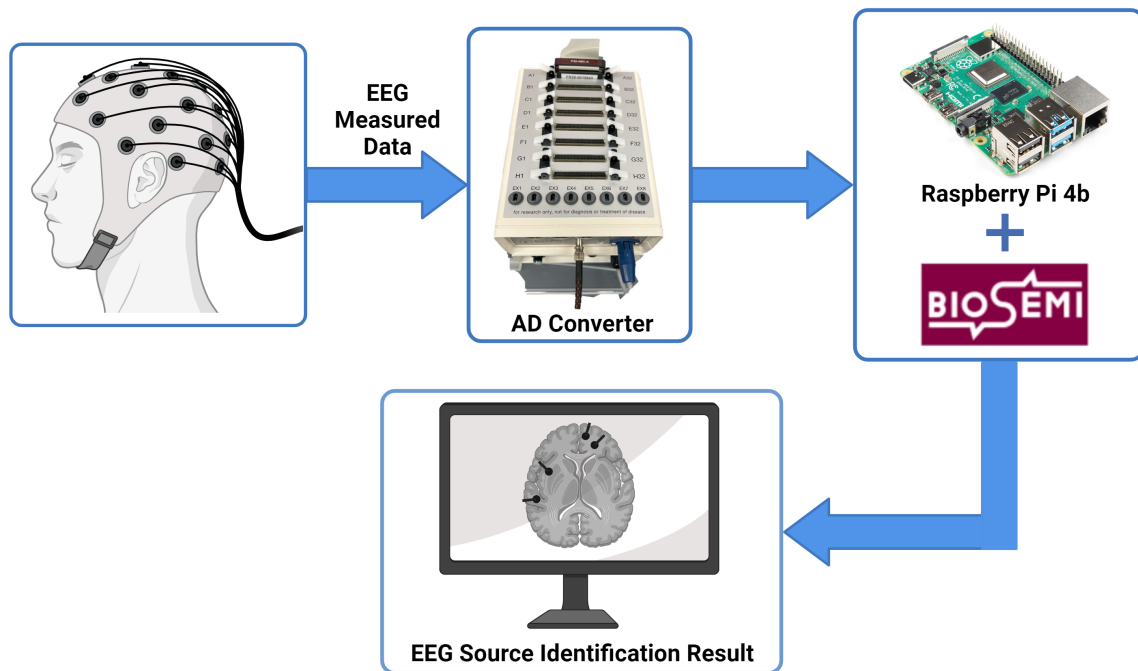
Figure 2.28: Experimental setup to employ real-time EEG data analysis

Chapter 3

Method for Identification of Multiple Low-Voltage Signal Sources Transmitted

Through a Conductive Medium[1]

Detecting the specific location of an electrical signal source immersed in a conductive medium is one of the critical problems in signal identification applications. Most prominent applications include underwater source localization [21, 22] and the Electroencephalography(EEG)/Magnetoencephalography(MEG) signal source localization [23]. The underwater source localization application can vary from underwater vehicle tracking to a vital task like an underwater rescue mission. The EEG/MEG source localization is also important since it is directly related to neurological disorders and can affect human health. It is certain that the application of optimized source localization algorithm is versatile and can be used to solve many critical problems including the ones mentioned. In the mentioned cases, the process starts with an electrical signal source that generates an electrical signal. Then signal transmits through a medium from the source to the sensors. Next, the signal is analyzed. These steps collectively provide the spatial location of the electrical source. Since each application involves different environmental conditions, the source identification algorithm must be adapted to ensure accuracy.

The EEG/MEG source localization process is essential in detecting different neurological diseases. In principle, an EEG is used to detect brain signals [24] and an

---

[1]Part of the material reported in this chapter is reprinted with permission, from "Namazifard, Saina, et al. "Method for Identification of Multiple Low-Voltage Signal Sources Transmitted Through a Conductive Medium." IEEE Access 10 (2022): 124154-124166." (reference [75]).

MEG is used to detect the magnetic fields produced by the electrical current inside the brain [25]. In both detection processes, the human head acts as a conductive medium where its outer surface is used for sensors (i.e. electrodes) to sense signals that are generated somewhere beneath the inner surface (i.e. specific brain signals) [26, 27]. In other words, the human head transmits the source generated inside the brain to the electrodes attached to the head. Then recorded data is used for source localization of that electrical signal source. A healthy human brain generates brain waves with a specific range of frequencies and amplitudes [28, 29]. Following some specific motor or sensory activities, the frequencies and amplitudes of the brain waves change. By comparing and analyzing the recorded EEG data, before and after the specific activities, any sign of abnormalities at a particular region of the brain can be predicted [30]. Over the past several years, various methods have been used to solve the localization problem [31]. Note that, there are different applications such as image processing [32–34], fault location in grounded/ungrounded and high-resistance systems [35], and sound source localization [36, 37]. Depending on the application, the solution methodologies are different. In principle, all these methods solve an inverse problem. Nevertheless, all methods have their own advantages and limitations.

The Minimum Norm (MN) method for this application was first introduced in 1994 [38] to solve the specific inverse problem and source localization from EEG signals. This method is proper for noise-free signal analysis, but it does not provide a good result for the deep source localization cases where noise can be inherently present in the signal source. In the same year, a new algorithm called Low Resolution Electromagnetic Tomography (LORETA) was introduced [39]. The LORETA can be considered as an integrated method that combines the weighted minimum norm (WMN) technique [40] with the Laplacian operation. It resolves the deep source

localization problem of the MN method. However, the low spatial resolution can be the main disadvantage of this algorithm.

Implementing the recursive steps in solving the inverse source localization problem has significantly improved the results. FOCal Underdetermined System Solution (FOCUSS) is one of these methods which utilizes the WMN to solve the recursive process. FOCUSS could solve the problem of low-resolution result with the LORETA algorithm properly [41].

The other popular EEG source localization method is the Recursive multiple signal classification (MUSIC) [42]. This method defines the source (dipole) in a 3D grid head model. The algorithm is based on the idea of finding a signal subspace and addressing if it works the best for the forward model.

Often the existing EEG source localization methods are modified or combined to generate new algorithms. Examples include methods such as Exact low resolution brain electromagnetic tomography (eLORETA), standardized low-resolution electromagnetic tomographic analysis (sLORETA), RAP MUSIC, LORETA FOCUSS, etc [31]. The new methods offer applications beyond the traditional EEG source localization algorithms. For instance, the MUSIC method can also be used in the sound source localization, as illustrated in [43].Another application is the acoustic source localization problem. This usually addresses the source localization for the 2D case (both isotropic and anisotropic plates) and the 3D structures. One of the most famous methods is Beamforming which is also utilized in the EEG source localization problems [44]. The advantage of using such methods over traditional EEG source localization methods is the robust behavior of the noisy data with the White Gaussian noise. Also, a few source localization methods depend on knowing the Time of Arrival (TOA) information [45]. In other words, the time a specific signal needs to travel from the source until it reaches the sensor should be available. However, the

Beamforming method works appropriately regardless of having the precise Time of Arrival (TOA). Thus, depending on the situation, these methods can not only be for source localization inside human brain but also used for similar kind of application.

The Least-squares method uses the real collected signal and the signal generated by the hypothetical electrical source to identify the electrical source. Finding the global minimum of these two signal differences provides the final answer to the source estimation [46].

As mentioned earlier, MUSIC [47] is one of the common methods in different application areas and is not only limited to the EEG source localization problems. It should be noted that most of the algorithms mentioned earlier can only detect the location of the sources but not the other features such as the simultaneous detection of frequencies, phases, and amplitudes of the multiple active electrical signal sources. More information about the electrical source can be important for many reasons. For instance, in the case of a rescue mission, there might be other active electrical sources in the water. The specific amplitude and phase information can help distinguish the emergency pulse-generating device from the other electrical sources.

In this study, we have proposed an optimized constrained Least Squares based method to detect the location of multiple signal sources immersed in a conductive medium. This algorithm not only locates the source but can also estimate other oscillatory signal features, such as frequency and phase. Without losing any generality, we applied our algorithm for low-voltage source localization. For experimental verification, we have used a low-voltage signal source and evaluated the effectiveness of our algorithm. The signal sources used were in the mV range. A small lab-scale experimental setup has been developed for validation that includes a system for generating electrical signals, a conductive liquid medium for signal transmission and EEG-based electrodes for detecting signals. To verify the algorithm, input data has been collected

from the experiment. The remainder of the manuscript is outlined as follows. First, a mathematical model is defined to simulate the signal measurement process in the Method section. Afterward, an algorithm based on the Least Squares error is introduced to solve the feature identification problem. The Experiment section describes the experimental setup used to generate the data in detail. Finally, the data from the experimental setup is passed to the introduced algorithm to assess its accuracy.

3.1 Method

In a source localization algorithm, it is desired to find a precise estimation of the actual source location. Fig.3.1 schematically defines the problem. It can be inferred from Fig. 3.1 that while the exact location of the electrical source is fixed at a point (identified as a red dot), the typical source identification algorithms can only estimate the source location within an area (the green circle). The ideal goal is to reduce the radius of the estimation result (i.e. radius of the green circle) until it gets as small as the red dot. When this happens, it means the source localization method works accurately.

This study aims to introduce an algorithm that not only can precisely detect the source location of an oscillatory signal but also estimate all other characteristic signal features such as the frequency, phase, and amplitude. In general, any source identification problem is solved in two steps. The first step is called the Forward Problem, where the measured signal is simulated mathematically. According to Fig.3.2, a Forward Problem starts with all the known experimental parameters, such as the location of the sensors, the properties of the electronic signal source (location, frequency, phase, and amplitude), and the medium conductivity. All the mentioned properties are passed to a proper mathematical model that can simulate the signal

measured by each sensor. In other words, a forward problem describes the known experimental procedure using mathematical equations.

The second step is the Inverse Problem, which aims to predict the source location. As indicated in Fig.2, this problem starts in the opposite direction to the Forward Problem. In this case, it is assumed that the collected signals from the sensors are available, and by utilizing the present mathematical model, one should be able to find the source location and other features.
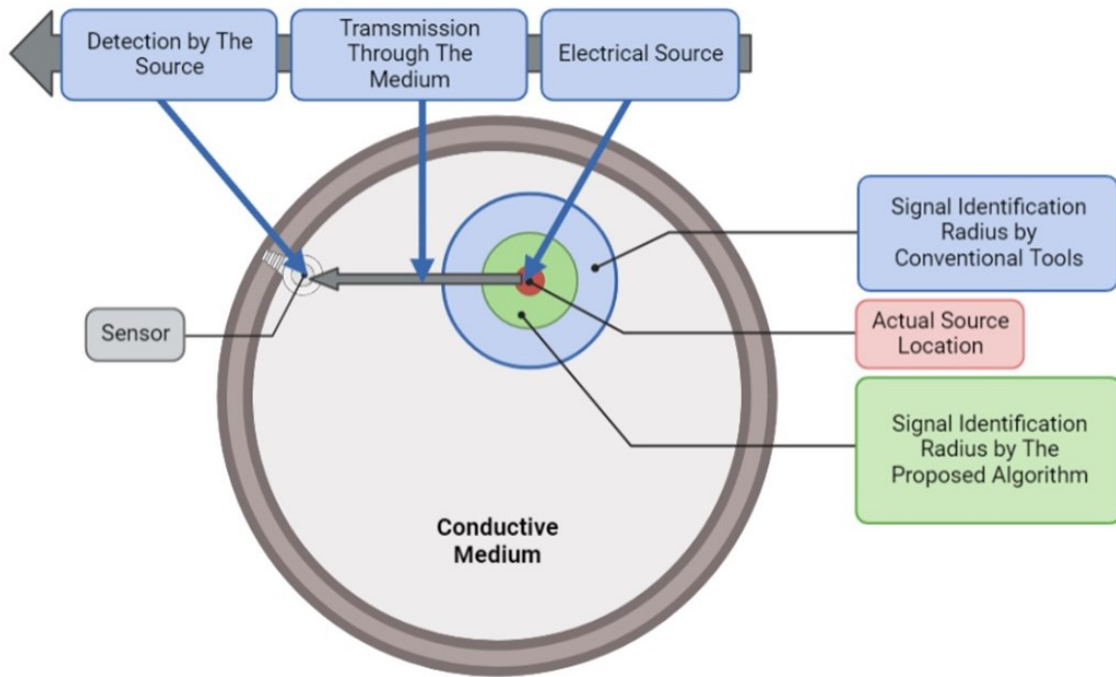
Figure 3.1: An illustration of the general form of the source localization problem

3.1.1 Forward Problem: Source and Sensors Mathematical Modeling

As described earlier, the forward problem begins with determining the source and the sensors model. In our case, we adopted a 2D circular area model with a radius,
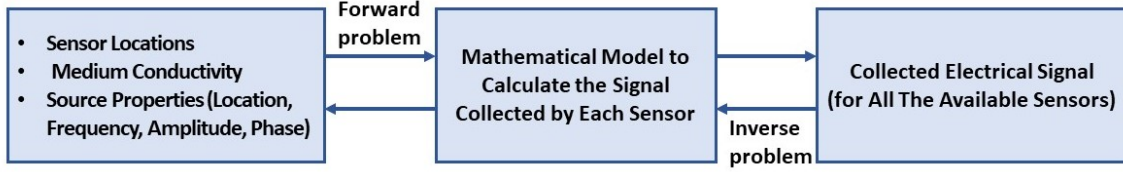
Figure 3.2: Definition of the Forward and Inverse problem

$R = 88.9mm$. It will be discussed later that the radius R in our model reflects the radius of the experimental bucket we used for validation. For precise comparison, the exact dimension of the radius is maintained in our model. Figure 3.3 is a schematic representation of the source and sensors in our 2D space. According to Fig. 3.3, the locations of the sources and sensors are described by the polar coordinates system. As an example, the location of the ith sensor and j^{th} source are shown as (r_{s_i}, θ_{s_i}) and (r_{c_j}, θ_{c_j}) respectively.

As described later in the experimental setup section, the sensors are located on the circumference of a circle (i.e, the experimental bucket) where the first one is at $(R, \frac{\pi}{2})$. The other sensors are labeled in the CCW direction, as it is shown in Fig. 3.3. It should be noted that a total number of 32 sensors are considered in our study.

To quantitatively describe the signal generations and detections, one needs to use Maxwell's equations and the Biot-Savart law [9], [10]. In our case, we have combined the two equations, and after some simplification, the expression for describing the measured signal in a 3D half-sphere model is defined as

$$\mathbf{f}_{i,j} = \frac{g_j}{4\pi\zeta} \frac{\left(\boldsymbol{r}_{c_j} - \boldsymbol{r}_{s_i}\right)}{\left\|\boldsymbol{r}_{c_j} - \boldsymbol{r}_{s_i}\right\|^3} \boldsymbol{\mu_j} + \boldsymbol{n_i} \tag{3.1}$$

where $\mathbf{f}_{i,j} \in \mathbb{R}^n$ represent the collected signal from the jth source to the ith sensor. Also, in this model, it is assumed that the jth source signal has a specific direction which is identified by a unit vector $\boldsymbol{\mu}_j \in \mathbb{R}^3$ and a magnitude $g_j \in \mathbb{R}$. In
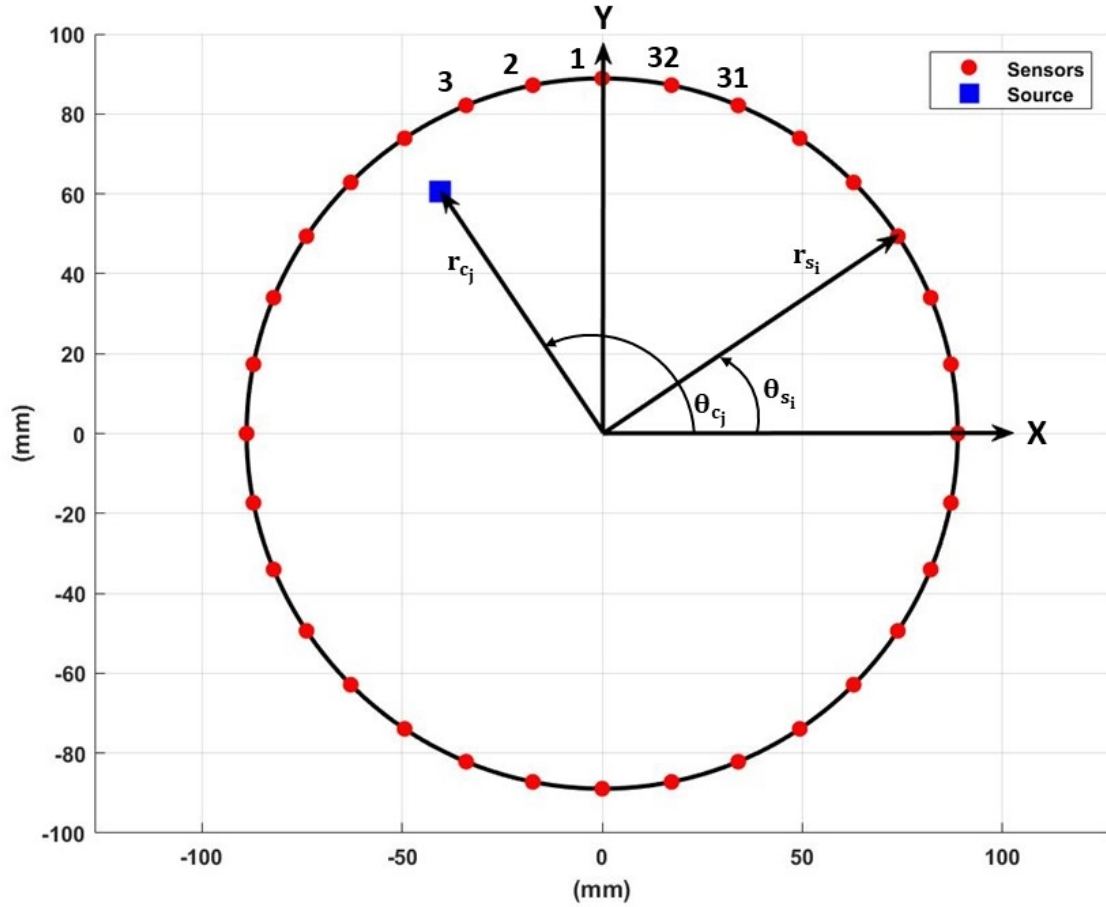
Figure 3.3: The 2D model of the sensor and source locations

order to make the model more realistic, a white Gaussian noise $\mathbf{n}_i \in \mathbb{R}^n$ generated from each sensor is added to the model.

This mathematical model however needs to be updated based on the experimental setup and assumptions considered in the present study. Since the source is assumed to generate sinusoidal signals in all directions in the 2D plane while the data samples are recorded. Two significant changes are made to the forward model: 1) The unit vector $\boldsymbol{\mu}$ is eliminated and re- placed with a sine wave signal to eliminate

the effect of the direction. 2) the vectors $(\mathbf{r}_{c_j} - \mathbf{r}_{s_i})$ are used to calculate the distance between different sources and sensors using the 2-norm as

$$d_{i,j} = \left\| \mathbf{r}_{c_j} - \mathbf{r}_{s_i} \right\| \tag{3.2}$$

where $d_{i,j} \in \mathbb{R}$ indicates the distance between j^{th} source to the ith sensor.

The above-mentioned changes state that the new mathematical model of the collected signal can be described as shown in Eqn. 3.3. This model is generated by considering all present parameters in the experiment. The parameters g_j, ζ, ω_j, and ϕ_j are the jth gain, conductivity, j^{th} frequency, and j^{th} phase of the source signal, respectively. Note that these values can be different from each source. Moreover, this model is written in the discrete form to show the collected signals for the kth measured data.

$$f_i(k) = \frac{1}{\zeta} \sum_{j=1}^{P} \frac{g_j}{d_{i,j}^2} sin\left(\omega_j k + \phi_j\right) + \boldsymbol{n_i}, i = 1, \cdots, 32 \tag{3.3}$$

This equation is the general form for the present study in the presence of P different sources. Eventually, one can put all the collected signals from sensors together to form the general matrix of the measured data for all available N data samples.

$$\mathbf{F} = [\boldsymbol{f_1} \boldsymbol{f_2} \cdots \boldsymbol{f_M}] \tag{3.4}$$

where $\mathbf{F} \in \mathbb{R}^{N \times M}$. Also, in this study $M = 32$.

Now, one can solve the forward problem by knowing the location of the sources and sensors, the magnitude and frequency of the sources, and the conductivity. This is helpful since a well calibrated forward model can be used to predict the expected output.

3.1.2 Inverse Problem: Source Localization Algorithm

The objective here is to utilize the proposed mathematical model (assumed to be calibrated) to find the location of the source. For this, one should solve an inverse problem where the measured signal Matrix **F** as in Eqn. 3.4, the location of the sensors, and the conductivity are available. As mentioned in the introduction section, several different algorithms are available to quantify the source location by solving the inverse problem. This study introduces a new approach based on the Least Squares error. Ultimately, the results from the experimental data illustrate the efficiency of this proposed algorithm.

3.2 Solution Methodology: A Least Squares error based Source Localization Algorithm

This section illustrates the details of the Least Squares error source localization algorithm (LSSL). The idea of implementing this algorithm comes from the EEG source localization problem, which is addressed in [76]. All steps of the LSSL algorithm are briefly shown in a flowchart form in the Fig.3.4.

In this study, there are a total of five unknowns $(r, \theta, \omega, \phi, g)$ for each source. We estimate these unknown parameters while the estimation problem is optimized and leads to the least estimation error possible.

As it is illustrated in Fig. 3.4, the estimation process is started with the data from the experiment. The experiment setup is described thoroughly in the following sections. After reading the experimental data, one of the most crucial steps is to determine an initial guess for the frequency of the generated signal from the sources. As outlined in Eqn. 3.3, the frequency appears in the nonlinear term that makes the estimation process very sensitive to its initial value. Moreover, missing data

points while recording the experimental data samples sometimes can occur. Thus, the initial guess process should be robust to an uneven sampling rate. Considering all the mentioned factors to estimate the source frequencies, the Lomb-Scargle Spectral Analysis is the proper method in this study. This method is described by details in [77], where the periodogram for N number of samples is presented in Eqn. 3.2. In this equation, μ, σ, and τ represent the mean, standard deviation, and time shift, respectively.

$$P(\omega) = \frac{1}{2\sigma^2} \left\{ \frac{(\sum_n (x_n - \mu) cos(\omega(t_n - \tau)))^2}{\sum_n cos^2(\omega(t_n - \tau))} + \frac{(\sum_n (x_n - \mu) sin(\omega(t_n - \tau)))^2}{\sum_n sin^2(\omega(t_n - \tau))} \right\}$$

Following the Lomb Scargle Spectral Analysis, a guessed value of $\hat{\omega}_0$ for each source is obtained. It is assumed that each source generates a sine-wave with one particular frequency. However, this method can identify multiple frequency components in a signal, which helps identify multiple frequency components in signal. The next step of estimation is using all five initial guesses $(\hat{r}_0, \hat{\theta}_0, \hat{\omega}_0, \hat{\phi}_0, \hat{g}_0)$ to substitute them in the forward model (Eqn. 3.3) and generate the first estimated signal matrix $\hat{\mathbf{F}}$. This synthetic signal is based on the assumed features, and it does not necessarily contain the features present in collected signals. To quantify the difference of the estimated signal and the actual data from the experiment, a cost function is defined. The cost function J is based on the measurement residuals of all 32 available sensors in this study. Now, denoting the decision vector $\hat{\mathbf{x}} = \begin{bmatrix} \hat{r}_1 & \hat{\theta}_1 & \hat{\omega}_1 & \hat{\phi}_1 & \hat{g}_1 & \cdots & \hat{r}_P & \hat{\theta}_P & \hat{\omega}_P & \hat{\phi}_P & \hat{g}_P \end{bmatrix}^T$, the goal is to minimize the L_2 norm of the cost function, which is defined as

$$J(\hat{\mathbf{x}}) = \left\| \mathbf{F} - \hat{\mathbf{F}}(\hat{\mathbf{x}}) \right\| \tag{3.5}$$

Note that the estimation result for the radius of the sources cannot be any number larger than the bucket's radius $R = 88.9mm$. Thus the optimization of the

64

cost J is subject to the M inequality constraints, $\|\hat{\mathbf{r}}_j\| - R < 0$, for $j = 1, \ldots, P$. The constrained optimization then proceeds along the typical steps outlined in [78] (Chapter 1, section 1.7) by formulating the constraints augmented cost, and deriving the necessary conditions (Kuhn Tucker conditions).

The constrained optimization problem is solved using MATLAB's FMINCON function, with a function tolerance value set to $\epsilon = 1e - 6$. The update to the decision vector between iterations uses the the Gauss-Newton method (selected in the FMINCON options). The update steps repeat until the cost function reaches its minimum (set to the function tolerance). Eventually, the converged parameters are taken as the final estimation result for all five unknowns for each of the sources.
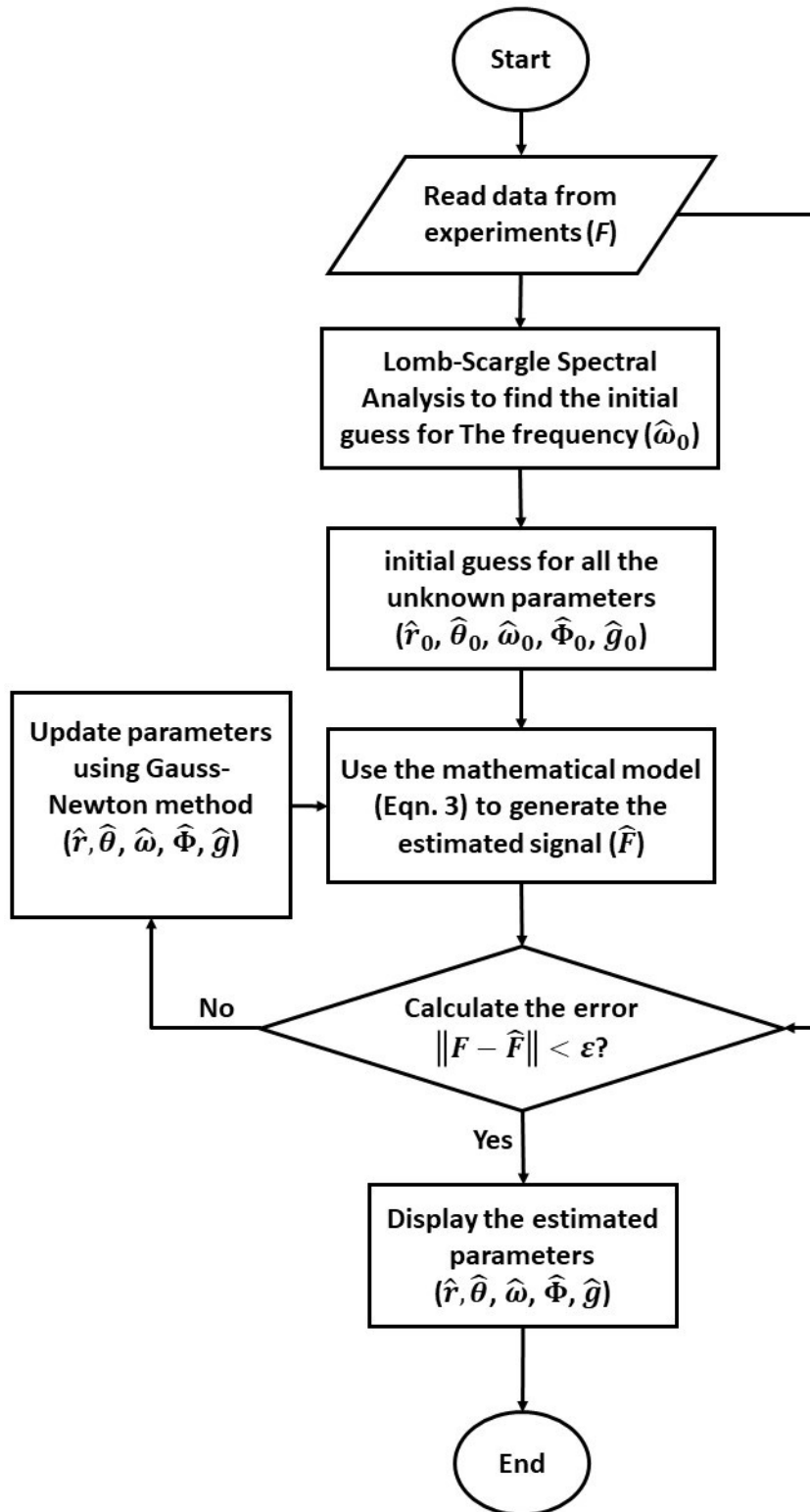
Figure 3.4: Inverse problem solution using LSSL algorithm illustrated by a flowchart

3.3   Experimental Setup

The experimental setup includes a plastic bucket, 32 sets of scalp electrodes as sensors, and artificially produced electrical signal sources as shown in Fig. 3.5a. Figure 3.5 shows the overall set up of the experiment. In this study, wet electrodes have been used [79]. As a conductive medium between the sensors and the source, we use saline water. It should be noted that the experimental technique is applicable to a broad range of conductive mediums. Without losing generality, we have maintained the conductivity of our saline water based on the data presented in [80], and [61]. Accordingly, appropriate salt concentration [81] was used to prepare the desired conductive medium between the sensor and the source. For record keeping purposes, the 32 electrodes are indexed as $A_1 - A_{32}$. Considering the equidistance method used in positioning the electrodes in the electrode-cap, the 32 electrodes were placed radially equidistant from each other. Note that the bucket radius is 88.9 mm. The angle between the two consecutive electrodes was kept at 11.25 degrees. The position of the electrodes inside the bucket was measured using a protractor and marked for future analysis. A signal generator is used to produce some analog signals inside the conductive saline water. The analog signals were entitled as the source. The distance from the center of the bucket to the point where the source/signal generator is generating the signal is considered as distance 'r'. We have arbitrarily selected the sensor A_{25} as the reference source, and all other subsequent measurements were based on the position and angle of this sensor. As shown in Fig. 3.5, A_{25} position coincides with the reference axis 'x' and the sensor A_1 is aligned with the reference axis 'y'. As such, the angle for sensor A_{25} is measured as zero degrees. Essentially, A_1 and A_{25} are orthogonal to each other. The angle between sensor A_{25} and An in the counterclockwise direction is described by positive angle θ. Here n is the number of any sensors between $A_1 - A_{32}$.

The rounded part of the electrode was considered as the head of the electrode, and the side that connects with the analog-to-digital (AD) converter was considered as the tail of the electrode (Fig. 3.5b). The positioning of the electrodes was such that the head of the electrodes would be touching the bottom of the bucket. The tip of the electrode will be aligned with the angular marked-up lines. Each of the electrodes was attached to the bucket using insulation tape. All the output from these receiving sensors was connected to the AD converter of a complete EEG system. A silver chloride stick was used as a signal generator. Silver chloride (AgCl) stick was connected with the data acquisition system (DAQ) through a wire as shown in Figs. 3.5c and 3.6a. To make it function like a conductive wire, the AgCl stick was covered everywhere with insulation tape except at the tip. The stick was also inserted inside a plastic straw for added rigidity and ease in handling as shown in Fig. 3.5c.

Using PATRIOT RS- 232 digitizer which is a serial port connector with a 38400 baud rate, a stylus, and Locator software, we scanned the positioning of each electrode. The scanned data was recorded and applied for the source localization method we used. The electrodes/ sensors keep sensing the data inside the experimental bucket while turned on. Using Biosemi ActiView810-Beta1 software, those sensed data can be observed and recorded. As needed, the EMSE (ElectroMagnetic Source Estimation) Data Editor Software was used for converting the collected data into suitable file formats for subsequent analysis. It should be noted that the entire experimental setup, as shown in Fig. 3.5 and 3.6, is utilized for both single source and multisource experiment. In other words, the positions of the 32 sensors, the bucket and its medium, tools for sensor scanning as well as software for experimental data collection – all were identical throughout the single source and multisource experiments.

The whole experimental setup was covered with RF blocking cloth to minimize any interruption while recording. The sensors are sensitive to electromagnetic fields,

strong jerking, vibration, etc. In particular, the sensors that are located in closer proximity with the AD converted appear to be heavily impacted by the undesirable disturbances. As shown in Fig. 3.6, the experimental setup placed sensor $A_{16} - A_{19}$ closer to the AD converter. All the wiring from 32 sensors was also passed through the side of sensors $A_{16} - A_{19}$. So keeping the signal sources near that section of the bucket always cause some extra cautions and human errors in recorded data. Considering all factors, benchmark trial experiments were conducted to identify the suitable source position that ensures reproducible experiment. It was observed that source located as far as far possible from the AD converter is most suitable for the experiment. For this study, it means the source positioned between A_9 to A_{15} and A_{20} to A_{23} is the best position to use.

3.3.1   Source Generation

For the experiments, a simple sine wave was used as oscillatory signal source. The 781442-01 — NI USB-6361, X series multifunctional I/O DAQ module (16 AI, 24 DIO, 2 AO) from National Instrument was used for signal generation. Using LabView the system allows pulse width modulation, encoding and frequency measurements and many other functions. The amplitude and frequency were chosen randomly but kept constant for a similar category of experiments. For the single source experiments, a sine wave of frequency 10Hz and amplitude 10 mV was generated. We used two signal sources for multi-source experiments, and two different configurations were also used. Specifically, in the first set of experiments (referred as category 'a'), same amplitude and frequency for both sources are used. For second set (category 'b') different frequencies but same amplitude for each source is used. For category 'a', a set of 10Hz-10Hz frequencies was used. Category 'b' frequency pairs were 31 Hz-10 Hz, 10Hz-31Hz, 40-10Hz, and 10-40Hz. The selection of frequency pairs was random.
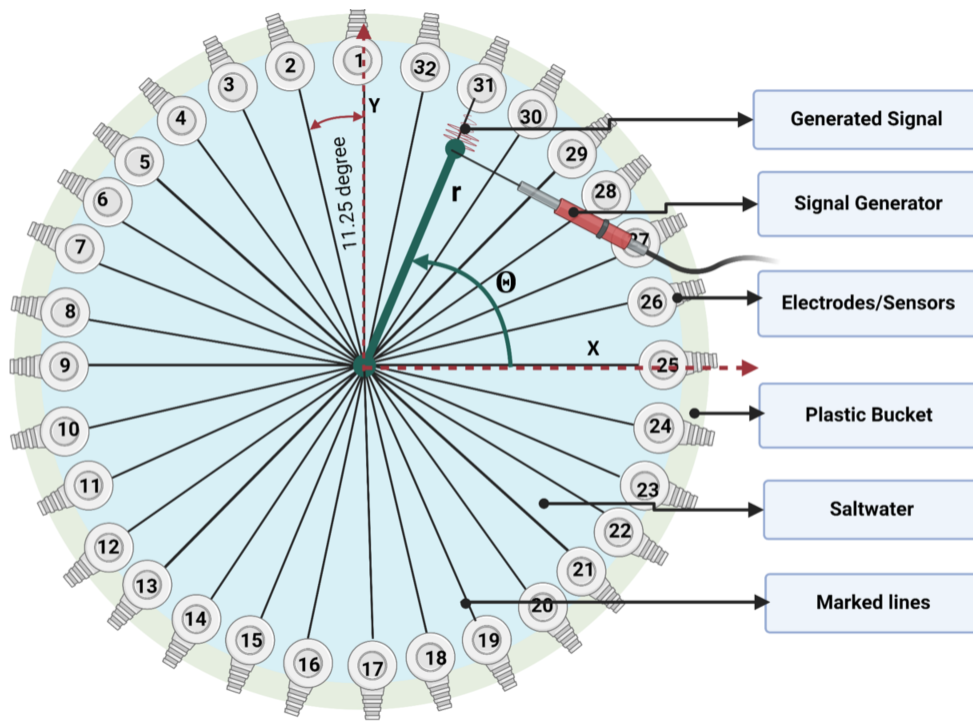
(a)
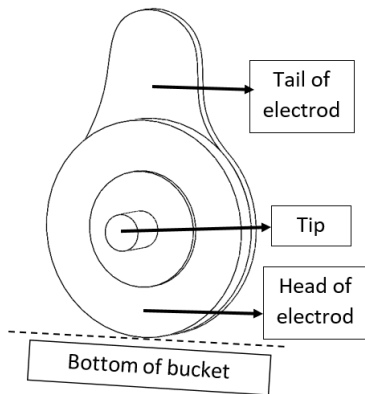
(b)
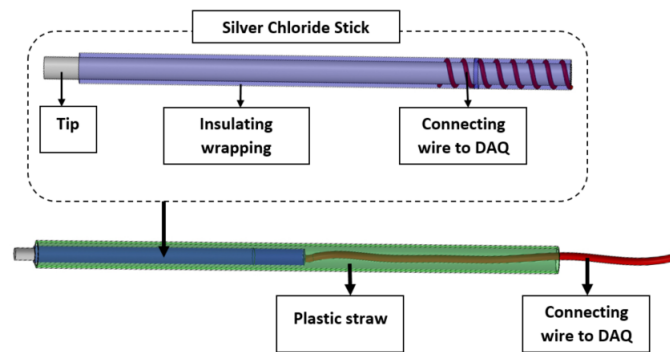
(c)

Figure 3.5: (a) Top view of the experimental bucket of radius R = 88.9 mm showing the 32 sensors, saline water as conductive medium and the artificially generated signal source. (b) Detail view of each electrode/sensor. The electrodes/ sensors are divided into two parts. The Head part of all the sensors makes contact with the bucket. The tail of the electrode is used to attach the electrodes to the surface of the bucket. This tail part also contains wires that connect the electrodes with the AD converter. (c) Detail view of the signal generator.

Table 3.1: Summary of Sensors, signal amplitude, and frequencies used in the experiment

Experiment type	Sensors used		Signal amplitude (mV)		Signal frequency (Hz)	
Single source	A_9		10		10	
	A_{10}		10		10	
	A_{11}		10		10	
	A_{12}		10		10	
Multiple sources	Sensors pairs		Signal amplitude (mV)		Signal frequency (Hz)	
Category 'a'	A_9	A_{23}	10	10	10	10
	A_9	A_{10}	10	10	10	10
	A_9	A_{13}	10	10	10	10
Category 'b'	A_9	A_{13}	10	10	31	10
	A_9	A_{13}	10	10	40	10
	A_9	A_{23}	10	10	10	31
	A_9	A_{23}	10	10	10	40

The tips of the electrodes used as receiving sensors are also made of silver chloride. Using any other material as a source generator creates a change of conductivity in the medium. This affects the homogenous nature of the medium. So the source/ signal generator we used was also made of AgCl. Each source is controlled independently. Table 3.1 shows the summary of experimental variables.

3.3.1.1   Single Source

For four sensors, $A_9 - A_{12}$, a total of 220 experiments have been conducted. Our experiments have been done for four different conductive mediums. The conductivities of the medium chosen were 2 mS/cm, 4.35 mS/cm, 15 mS/cm, and 20 mS/cm. The values are selected based on [80] and [61]. The single source/signal generator's distances were chosen randomly. The distance was marked and measured before the bucket was filled with the saline water. For convenience, the signal generator was always placed along the radial path of each sensor, as shown in Fig. 3.5a. For each source position shown in table 3.2, experiments were done in four of the

71

Table 3.2: Source positioning

Experiment Type	Positioning of the signal generator closer to sensors		r (mm)		$\theta(deg)$	
Single Source	A_9		70		180	
	A_{10}		70		191.25	
	A_{11}		77		202.5	
	A_{12}		73		213.75	
Multiple sources category 'a'	Source 1	Source 2	$r_1(mm)$	$r_2(mm)$	θ_1	θ_2
	A_9	A_{23}	70	73	180	337.5
	A_9	A_{10}	70	70	180	191.25
	A_9	A_{13}	70	73	180	225
Multiple sources category 'b'	A_9	A_{13}	70	73	180	225
	A_9	A_{13}	70	73	180	225
	A_9	A_{23}	70	73	180	337.5
	A_9	A_{23}	70	73	180	337.5

different conductive mediums. Following each experiment, the source position coordinates, source amplitude and frequency, the conductivity of the medium, and sensor data were recorded. These recorded data are used for validation of our mathematical model.

3.3.1.2 Multiple Sources

As outlined in Table 3.2, seven pairs of electrode positions were selected – three of which are for category 'a' and the rest are for category 'b'. For this, a total of 30 experiments for category 'a' and 40 experiments for category 'b' were conducted. The conductivity for the medium was kept constant at 4.35 mS/cm for category 'a' and 15.2 mS/cm for category 'b'. The distance and the angular position of the sources for both of the categories are shown in table 3.2.

(a)

(b)
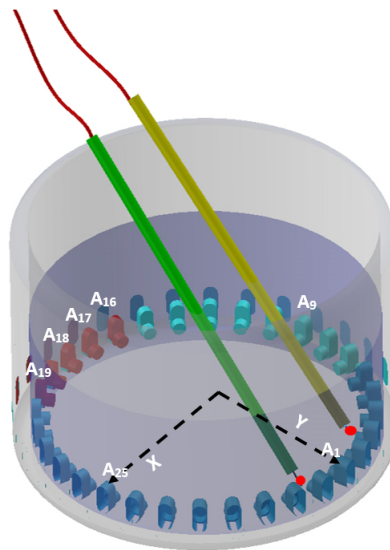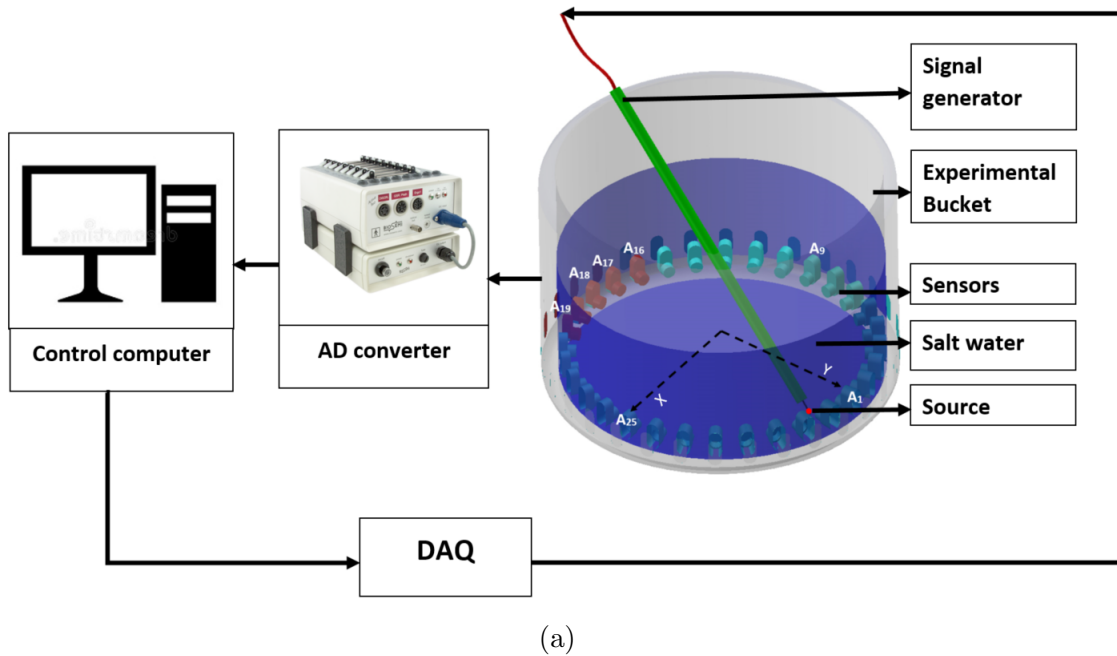
Figure 3.6: (a) The experimental setup. The experimental bucket is connected with an AD converter through 32 sensors. The AD converter helps to record real-time data on the computer. The computer is also the controller for the source supply. The amplitude and frequency details are maintained as shown in Table 3.1. The amplitude and frequencies are controlled through DAQ. For a single source experiment, only one signal generator remains active. For the multi-source experiment, both sources are active. (b) Experimental bucket with two signal generators for multisource experiments.

3.4   Results and Discussion

The validation experiments for source identification simulation includes three steps – signal source generation, processing and analysis. Parallelly, the simulation steps are divided into two parts. The first part is called coarse localization. This is also known as visual analysis. The second part is point localization. This step quantitatively determines the near exact location of the source(s) with minimum error.

3.4.1   Coarse Localization

We considered the A_{25} position as 0 degrees or the reference. The angle was measured in the counter-clockwise direction. So, the angular position of the 'A_n' sensor will be

$$[(n-1) \times 11.25] + 90 \tag{3.6}$$

Here n is the number of the sensor that shows the highest signal strength in visual analysis. The simulation result for a single source is shown in Fig. 3.7a and 3.7b. It should be mentioned that, the source was kept at $r = 73mm$ and $\theta = 213.75$ degree near sensor A_{12} and the conductivity of the medium was 4.35 mS/cm. It is evident from Fig. 3.7b that the amplitudes of the signals picked up by the sensors are greatly dependent on the distance between the sensor and the source. It can be observed from Fig. 3.7b that the signal strength of sensor $A_{11} or A_{12}$ is the highest as it is located closest from the signal source. The signal intensities gradually reduce on the adjacent sensors as the distances between the source and the sensors increase. Using Eqn. 3.6, it can be found that the source must be located between $\theta = [202.5, 213.75]$ degrees near sensor $A_{11} or A_{12}$. However, this technique is unable to specify the radial

position of the source. As such, the estimation of source location is not a point but a covered area, as shown in Fig. 3.7a and 3.7b. The "out-of-range" area shown in the Figs. 3.7a and 3.7b refers to the region where a presence of source within the area is not reliably detectable by the sensor. For our case, the radius of this "out-of-range" circle is about 50 mm.

For multiple source cases, two different source locations are considered. In the first case, as shown in Figs. 3.7d, the coarse identification process locates the positions of the sources near sensors $A_9 - A_{13}$ and $A_{12} - A_{21}$, respectively. Similarly, for the second case, as shown in Fig. 3.7f, the positions of the two sources are within the areas covered near $A_9 - A_{13}$ and $A_9 - A_{23}$, respectively. It can be inferred from Figs. 3.7d, and 3.7f that, like the single source case, the highest amplitudes recorded by the sensors are near the position of the source. As the distance between the sensor and the source increases, the amplitude of the signal drops. Such trend in signal amplitude variation is also clearly visible when multiple sources are present. As such, the coarse localization method provides a clear indication that the source is located somewhere within the localized region. However, there is a limitation in the coarse localization method. The method is suitable for sources that are located relatively far from each other. In such cases, the two sources only weakly interact with other. As a result, the signal strengths in the adjacent sensors are only affected by the nearest source. This is evident in Fig. 3.7f. When sources are close to each other, then the sources interact strongly with each other. Therefore, the signal strengths in the adjacent sensors are affected by the signals from both sensors. As a result, the coarse method fails to identify the approximate areas of any of the sources, as evident from Fig. 3.7d. To determine the specific location of the source or sources, regardless the sources are strongly or weakly interacting, a finer identification technique is required.

This is the basis for our mathematical model based on the LSSL method. The results are discussed in the following section.

3.4.2   Identification using LSSL Method

Now that the experimental data is available, the accuracy of the proposed algorithm can be determined. As mentioned in the previous section, three general cases are considered in these experiments, including 1) single source, 2) strongly interacting multiple sources and 3) weakly interacting multiple sources. Fig.3.7 represent the source localization results for these three cases.

While Fig.3.7 is only a representation of the source localization, Tables 3.3, and 3.4 provide more details regarding the estimation result of unknown parameters for Single-source and Multi-Sources case, respectively. This table illustrates the details in Figs.3.7a1, 3.7b1 and 3.7c1. In this table, it is important to note that the initial guess for the frequency is significantly close to the real value. This confirms the effectiveness of the Lomb-Scargle method in frequency estimation. To demonstrate the implementation of the Lomb-Scargle algorithm, Fig.3.8 is also provided. Moreover, to clarify the accuracy of the phase and gain estimation, Fig.3.9 is provided. This figure shows the estimated signal in blue and the measured signal in red. Note that these two signals completely cover each other, and the only difference is the noise in the measured data.

Comparing the provided results in the mentioned figures and table illustrate that by increasing the number of sources, the error of the estimation result increases as well. Two main reasons describe this observation. First, by increasing the number of sources, the number of electronic parts increases, leading to more significant noise. Secondly, having more than one source means the unknown variables increase while the amount of the collected signals and the number of sensors remain the same. This

76

means the measured data might not be enough to estimate all the unknowns for a large number of sources.

Table 3.3: Simulation result for Single-Source case

Source #1				
	Initial Guess	Estimation Result	True Value	Error %
r (mm)	85	72.33	73	0.92
theta (deg)	133.75	121.02	123.75	2.21
frequency (Hz)	10.001	10.75	10	7.4952
phase (rad)	0.28	-1.72	N/A	N/A

Table 3.4: Simulation result for Multi-Source case

Source #1				
	Initial Guess	Estimation Result	True Value	Error %
r (mm)	75	63.47	70	9.33
$\theta(deg)$	182	178	180	4.81
frequency (Hz)	40.04	40	40	0.00
phase (rad)	-1	-3.01	N/A	N/A
Source #2				
r (mm)	75	68.69	73	5.90
$\theta(deg)$	330	338.46	337.5	7.20
frequency (Hz)	10.03	9.99	10	0.04
phase (rad)	-0.5	0.18	N/A	N/A
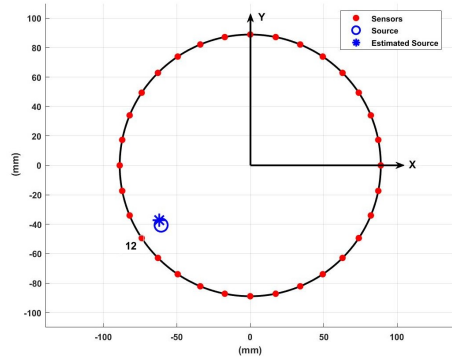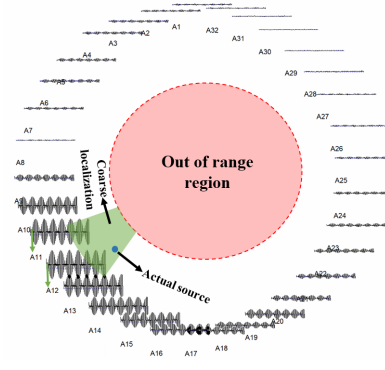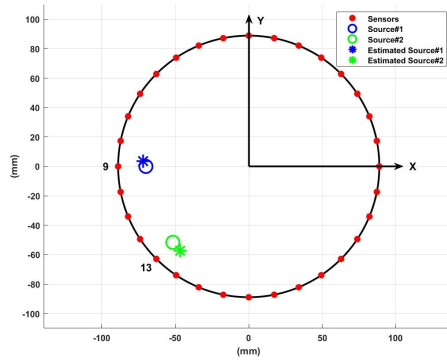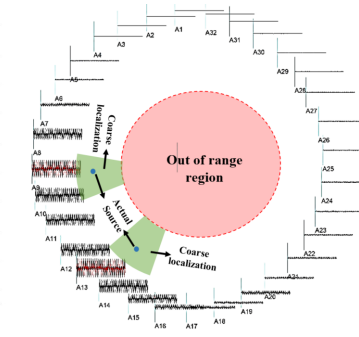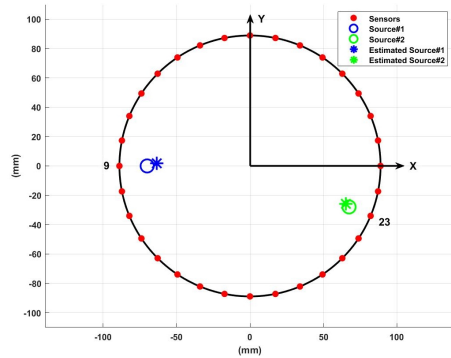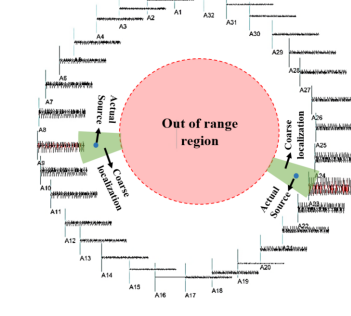
Figure 3.7: The effectiveness of the source identification model for (a), (b) single source near sensor A_{12}. (c), (d) multi-sources near the sensor A_9 and sensor A_{13} and (e), (f) multi-sources near the sensor A_9 and sensor A_{23}. Note that the actual data point is marked by open circles, and estimation is marked by the symbol '*'. Also note the sources in (d) represent strongly interacting sources, whereas the sources in (f) represent weakly interacting sources.

78
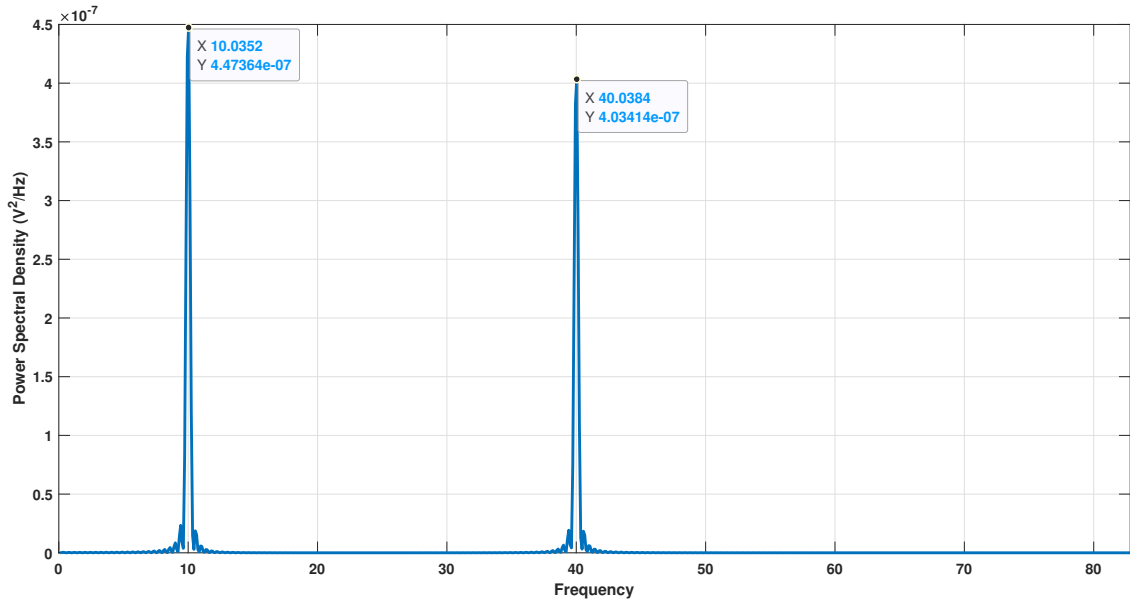
Figure 3.8: Lomb-Scargle Power Spectral Density for two sources with different frequencies.
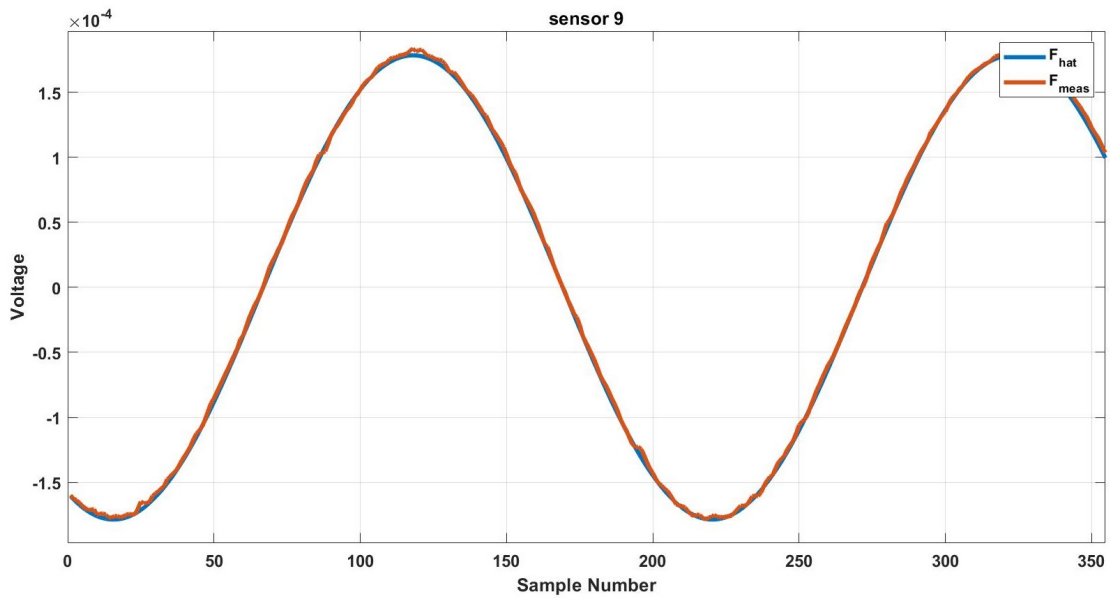
Figure 3.9: Comparing the measured signal ($\mathbf{F_{meas}}$) and the estimated signal result ($\mathbf{F_{hat}}$)

3.5   Experiment Limitations

Although it is shown that the introduced algorithm is efficient in estimating the electrical source properties, it is essential to mention that there are limitations to the present experimental setup. Since the number of sensors is fixed in this experiment, any increase in the number of unknowns can affect the estimation result accuracy. Note that each electrical source has five unknowns to estimate, and this section focuses on the effect of a few of these parameters on source identification results.

3.5.1   Effect of Distance Between The Source and Sensors on Source Localization
        Result

In this experiment, a round bucket filled with salt and water is used to simulate transmitting an electrical signal through a medium. Based on the geometry of this bucket, if the source is located at the center of the bucket, all the sensors will collect the identical signal since the distance between the source and the sensors is the same. Moreover, increasing the distance between the source and the sensors decreases the signal's strength. Given these two factors, it is expected to have more source localization errors by moving a single electrical source toward the center of the bucket. To quantify the effect of this factor, a new set of experiments is done where the source is moved every $10mm$ toward the center. The associated results of this experiment are provided in Fig.3.10. As it was expected, The best result belongs to where the source is almost touching the tip of sensors at $r = 62mm$. Note that in this experiment, the electrical source could not located precisely at the center of the bucket since the CMS sensor is attached to the center. Thus, the highest distance is considered where the source is located at $r = 5mm$. Note that although this section focuses on the limitations of this experiment, the algorithm still provides a proper result for the

source localization. The highest error for this set of experiments is still less than $1cm$, which shows the efficiency of the introduced algorithm.
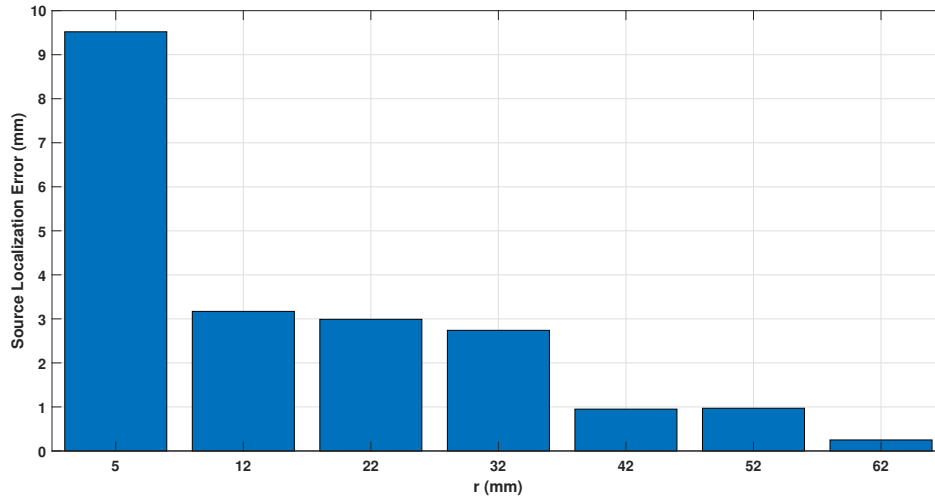
Figure 3.10: Moving the electrical source toward the center in the present experimental setup leads to higher error in source localization result.

3.5.2 Effect of SNR on Source Localization Result

Signal to Noise Ratio (SNR) is one of the essential factors that needs to be considered in signal analysis subjects. An ideal algorithm is one with noise robustness, which means the signal analysis result (in this case, source localization) will not be changed for a wide range of SNR.

In order to check the noise robustness of the proposed source localization algorithm, a white Gaussian noise is added to the electrical signal in this experiment. The range of SNR has been changed from -3 to 25, and the results are provided in Fig.3.11. As illustrated in this figure, the source localization error is lower for the SNR range of $5 - 25dB$. However, compared to less SNR, the source localization error is only $0.4mm$ lower. Given this slight difference and the fact that the source

localization error is approximately less than $1mm$ for different values of SNR, one can say the proposed algorithm is robust to noise.
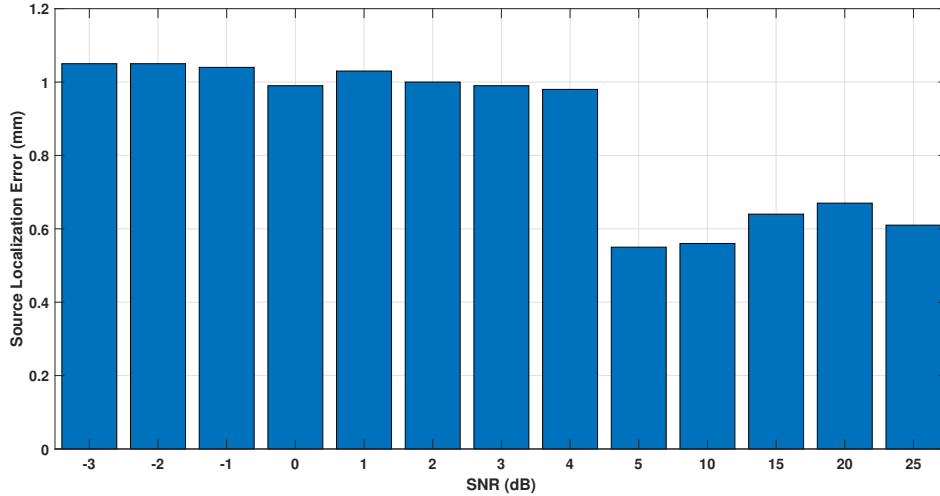
Figure 3.11: Decreasing the SNR slightly increases the source localization error.

3.6   Summary and Conclusion

In this study, the problem of source localization is addressed in detail. The solution is solving the inverse problem where the data is available and the source is unknown. We choose the Least Square Error-based algorithm among all the proposed methods to solve this problem and locate the source of signals. This algorithm is unique as it is not limited to only estimating the location of the source. It is shown that other source parameters, such as the frequency and the phase, can be determined using the present algorithm.

As described in this chapter, a bucket filled with salt and water is used as an experimental setup. To collect the generated signals, 32 sensors are located inside the bucket. The signal is generated in the sinusoidal form with a specific frequency

and location. After collecting the signals, they are used in the LSSL algorithm to solve the inverse problem and find the source properties. All the provided figures and the table in this chapter state the presented algorithm's accuracy. Regarding the source localization error, the distance between the source and the estimation results is not greater than 1cm. Comparing this promising result with similar studies like [47] implies the added advantage of the LSSL algorithm.

In Conclusion, the Least Square error-based algorithm can be introduced as an efficient way to solve the inverse problem. Not only the estimation error is significantly lower than the other common methods, but other features like frequency can also be estimated along with the source localization. This study paves the way for further study in signal source localization, where a significantly large number of sources are present, and a non-invasive method is essential for source detection. In other words, in applications where only a forward problem is not practical, this inverse problem method can provide a reliable solution.

Chapter 4

EEG Forward Modeling Using Random Conductivity[1]

Brain activity analysis has been an essential subject for researchers and scientists for a long time. The goal is to study different aspects of neurological disorders such as sleep disorders, Alzheimer's disease, Parkinson's disease, etc. [82]. It has been shown in many different studies that Electroencephalography (EEG) is a proper way to collect brain signals and analyze them for various research and clinical purposes [83, 84]. Generally, analyzing the EEG signal has been conducted in a two-step process. The initial step is the forward problem which includes finding a proper head model and a mathematical formula to model the EEG measurement. The second step, called the inverse problem, involves solving the problem to estimate the source properties, including the location, orientation, and magnitude [75]. Despite the importance of both steps while analyzing the EEG signals, it is essential to note that any error on the forward problem will directly affect the accuracy of the inverse problem [85, 86]. Therefore, it is critical to determine a proper forward model before solving the inverse problem.

Various factors can affect the accuracy of the forward model, including the shape of the head model (spherical and/or realistic) [87], the number of tissues considered in a head model (skull, scalp, CSF, etc.), and the conductivity of the considered tissues in the head model [86, 88]. This study focuses on a recent factor, which is the conductivity of the different parts of the head model. The variety of this topic can be changed from considering a single-material head model [89] to studies where they

---

[1]Part of the material reported in this chapter is submitted to the Sensors journal.

considered up to 13 different tissues for the head model [7, 90]. There are also different studies where the author considered the layered head model and addressed the effect of the thickness of each layer [91], especially the skull, on the accuracy of both forward and inverse problems [92]. The common factor among mentioned studies is not considering any uncertainty for the available model and conductivities. However, a few studies addressed the influence of head tissue conductivity uncertainties on the forward/inverse problem. In [93], the author determines a conductivity range for each head tissue. This interesting assumption has been used in other studies such as [86], where only five tissues, including the skull, scalp, white matter, gray matter, and CSF, are considered. However, in this study, the conductivity is selected randomly for each tissue from the determined range. The result indicates that the uncertainty of CSF has the most negligible effect on the accuracy of the source localization result. In contrast, the conductivity uncertainties of the scalp and skull play a significant role in the inverse problem accuracy.

Regardless of the number of head tissues and the accuracy of tissue conductivity that is considered in different studies, they mostly employ Finite Element Method (FEM) to apply the conductivities in their forward model calculation. While this method is proven to generate precise results, it has some disadvantages. One of the essential difficulties that FEM can add to the problem is being computationally expensive. In other words, there is a trade-off between accuracy and the computation load while using the FEM. For instance, decreasing elements' size leads to a more accurate model and more computation simultaneously [94]. Although studies like [95] introduce an optimized form of FEM with higher accuracy and fewer computations, the problem of considering thousands of elements is still unsolved.

Considering the importance of head tissue conductivity accuracy and the complexity of applying the FEM to the head model brings a new problem, and this study

aims to address this problem. Among all the solutions to fill this research gap, considering the random conductivity all over the head is rare and has not been appropriately covered. The random tissue in the head model can diminish the computation complexity and might be helpful for cases when analyzing time is significantly essential, such as the real-time source localization problem. Moreover, to address the effect of this random conductivity on the simulation result, one can use the Monte Carlo Simulation, which is used in many different studies [96, 97].

In order to address the mentioned problem, firstly, the FEM method is provided in detail to emphasize the complexity of the calculation. Afterward, a new head model given the randomly distributed conductivity is introduced. Eventually, to compare the accuracy of the present model to the FEM model, a simulation will be provided to illustrate the similarity of the generated EEG signal from the realistic head model (using FEM) and the randomly distributed conductivity.

4.1 Problem Description

As it is stated earlier, the problem that is solved in this chapter is to reduce the computation load of the FEM head model while maintaining the accuracy of any EEG signal processing, e.g., Forward Problem and Inverse Problem. Finding a proper substitution for the FEM-based head model with less complexity can improve a wide range of EEG signal processing applications. For instance, the real-time EEG signal analysis needs an algorithm that can process the EEG data as fast as possible.

To solve the mentioned problem, this chapter introduces a novel head model based on random conductivity instead of implementing the FEM-based layered head model. The details of this method are addressed with details in the following sections.

4.2   Solution Methodology

This section first provides a brief review of the forward problem definition. Afterward, the FEM approach to solving the forward problem is presented to show its strengths and limitations. Eventually, our novel approach based on the random conductivity head model is introduced to illustrate how it can reduce the complexity of the FEM approach.

4.2.1   EEG Forward Problem

The neural activity in the head generates an electrical voltage that is too small to measure by electrodes. However, if a group of neurons simultaneously generate signals in the same direction, they can induce a noticeable voltage that is measurable on the scalp. These neurons, which are the source of electrical potentials, can be simulated by dipoles. The electrical signals generated from these active dipoles transmit through different head tissues such as gray matter, skull, and scalp until they reach the sensors. This process is illustrated in Fig.4.1.

Simulating this process as a mathematical model is called an EEG forward model, also known as the forward problem. One needs a proper mathematical forward model to quantify the measured EEG signal. The quasi-static approximation of Maxwell's equations and the Biot-Savart Low leads to a general formula to calculate the EEG signal generated from dipoles in the head model, transmitted through the head tissues, and eventually collected by EEG sensors located on the scalp [9, 10]. This equation, which is used as the forward model in this study, is represented as below:

$$v_{j,i} = \frac{1}{4\pi\sigma(\boldsymbol{r})}\boldsymbol{g}_{j,i}\boldsymbol{\mu}_i s_i + n_j \tag{4.1}$$
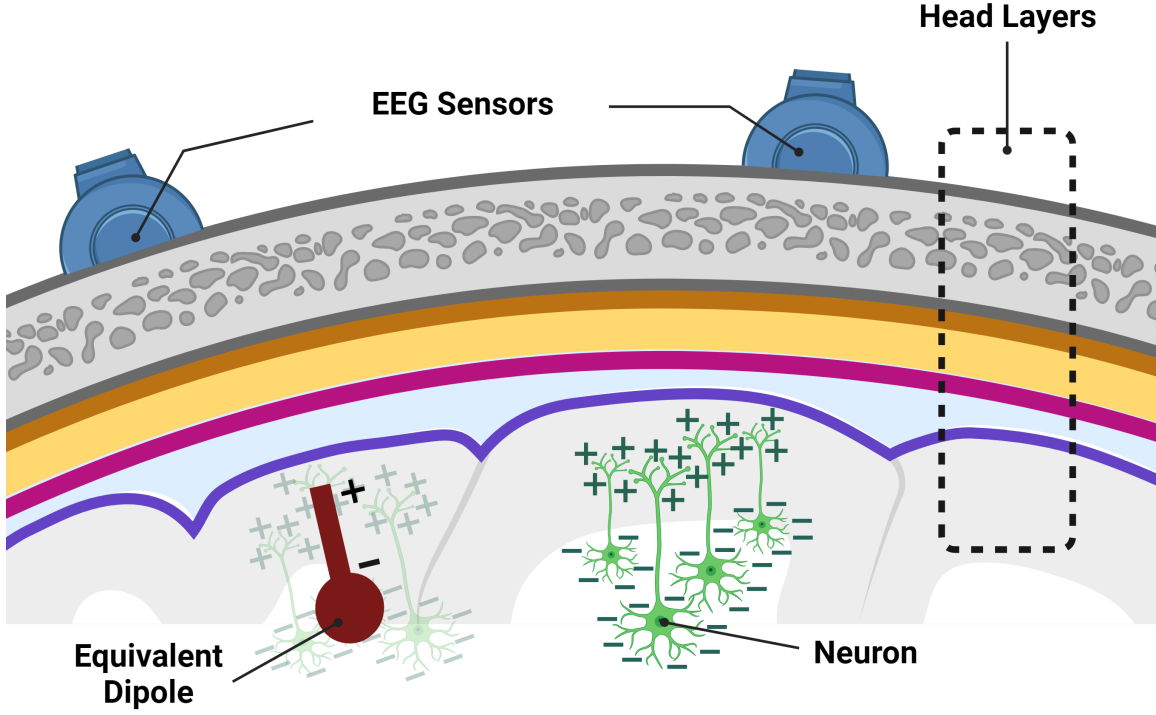
Figure 4.1: Illustration of the neural activity and the equivalent dipole as a source of electrical signal [1].

where,

$$\boldsymbol{g}_{j,i} = \begin{bmatrix} \frac{w_{x_j} - l_{x_i}}{d_{ji}^3} & \frac{w_{y_j} - l_{y_i}}{d_{ji}^3} & \frac{w_{z_j} - l_{z_i}}{d_{ji}^3} \end{bmatrix} \qquad (4.2)$$

In this equation, $v_{j,i} \in \mathbb{R}$ represents the measured EEG signal generated from the ith dipole, transmitted through the tissue with conductivity $\sigma(\boldsymbol{r})$, and received by the jth sensor. The Cartesian Coordinates of sensors and dipoles are shown as (w_x, w_y, w_z) and (l_x, l_y, l_z) respectively. Moreover, the distance between the ith dipole and the jth sensor is shown by d_{ji}. Each active dipole in the simulation has a particular orientation and magnitude as well, which is shown by $\boldsymbol{\mu}_i \in \mathbb{R}^{3 \times 1}$ and $s_i \in \mathbb{R}$. In order

to make the forward model more realistic, the Gaussian white noise n_j is added to the equation.

In order to find the signal generated from all active dipoles and measured by each sensor, one can use the summation of the signal generated by each dipole, as presented below:

$$\boldsymbol{v}_j(k) = \sum_{i=1}^{P} v_{j,i}(k) \tag{4.3}$$

Where P and k are the total number of dipoles and the sample number, respectively.

Eventually, by putting the data collected from each sensor for all the sample points together, the measured matrix $\mathbf{V} \in \mathbb{R}^{M \times N}$ is generated. An example of $\mathbf{V}$ matrix for N sample point and M sensors is presented in Equation 4.4.

$$\mathbf{V} = \begin{bmatrix} v_1(1) & v_1(2) & \cdots & v_1(N) \\ \vdots & \vdots & \vdots & \vdots \\ v_M(1) & v_M(2) & \cdots & v_M(N) \end{bmatrix} \tag{4.4}$$

Note that the presented forward model in Eqns.4.1 to 4.4, is generated for the homogenous isotropic conductor. This means that the provided equation needs a few changes, such as assuming the head tissues are inhomogeneous and anisotropic, to have a more realistic forward model. To do so, Let us first consider a dipole as a pair of monopoles, as illustrated in Figure 4.2 [98]. These two monopoles are located extremely close to each other with a distance of l. Moreover, they both have the same magnitude but opposite polarity of I. In the presence of this dipole model (or a pair of monopoles), there is a total current of $\vec{\boldsymbol{j}}$, which consists of the *primary current* $\vec{\boldsymbol{j}_p}$ and the *secondary current* $\vec{\boldsymbol{j}_s}$. The primary current can be calculated as below where

the $\vec{r}_{source}$ and $\vec{r}_{sink}$ are the location of the sink and source monopoles from the head origin, respectively. Also, δ is the Dirac distribution function.

$$\vec{j_p} = I \left[\delta \left(\vec{r} - \vec{r}_{source} \right) - \delta \left(\vec{r} - \vec{r}_{sink} \right) \right] \tag{4.5}$$
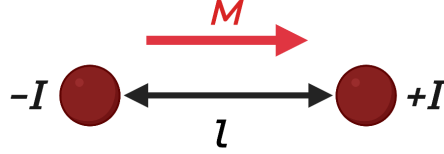
Figure 4.2: Illustration of a dipole, replaced by a pair of monopoles [1].

The secondary current is the associated current density in the conductor and is calculated by Ohm's law as shown below:

$$\vec{j_s} = \sigma(\boldsymbol{r})\vec{E} \tag{4.6}$$

Where the σ and $\vec{E}$ are the conductivity and the electric field, respectively.

Now that the current calculation is clear, one can use the quasi-static Maxwell equations presented in equations 4.7 and 4.8 to find Poisson's law given the Neumann boundary conditions as shown in equations 4.9 and 4.10. The head volume and the electric potential are shown by Ω and V, respectively [11, 99].

$$\partial \vec{j} = 0 \tag{4.7}$$

$$\vec{E} = -\nabla V \tag{4.8}$$

$$\nabla . (\sigma \nabla V) = \partial \vec{j_p} \quad \text{in } \Omega \tag{4.9}$$

90

$$\langle \sigma \nabla V, \mathbf{n} \rangle = 0 \quad \text{on } \Gamma = \partial\Omega \tag{4.10}$$

Now that the proper forward model is introduced, one should find a proper method to solve it and find the voltage generated by dipoles located inside the head model. First, we show the Finite Element Method, a popular method for solving Poisson's law. Afterward, a novel approach based on random conductivity is presented. Eventually, these two methods are compared to check for both accuracy and the computational load.

Note that in both approaches, it is essential to properly simulate the conductivity of different head tissues since it is a function of location. In other words, considering the head model consists of different layers, the dipole placement plays an important role in the signal path to reach the electrodes on the scalp. Fig.4.3 illustrates the layered head model and the variable conductivity in terms of the distance between the center of the head and the dipole's location.

4.2.2 Finite Element Method Application on EEG Forward Model

The concept of the Finite Element Method (FEM) is to divide the desired volume considered in a study into smaller elements. The most common shapes of elements for the 3D case are tetrahedra or hexahedra [11]. These shapes eventually form a mesh all over the desired volume, which is the head model in this study. This method helps to find the voltage on the scalp, generated from a dipole and transmitted through different tissues with various conductivities in the head model. The advantage of this method is to simulate the conductivity of different tissues very accurately using a massive number of elements.
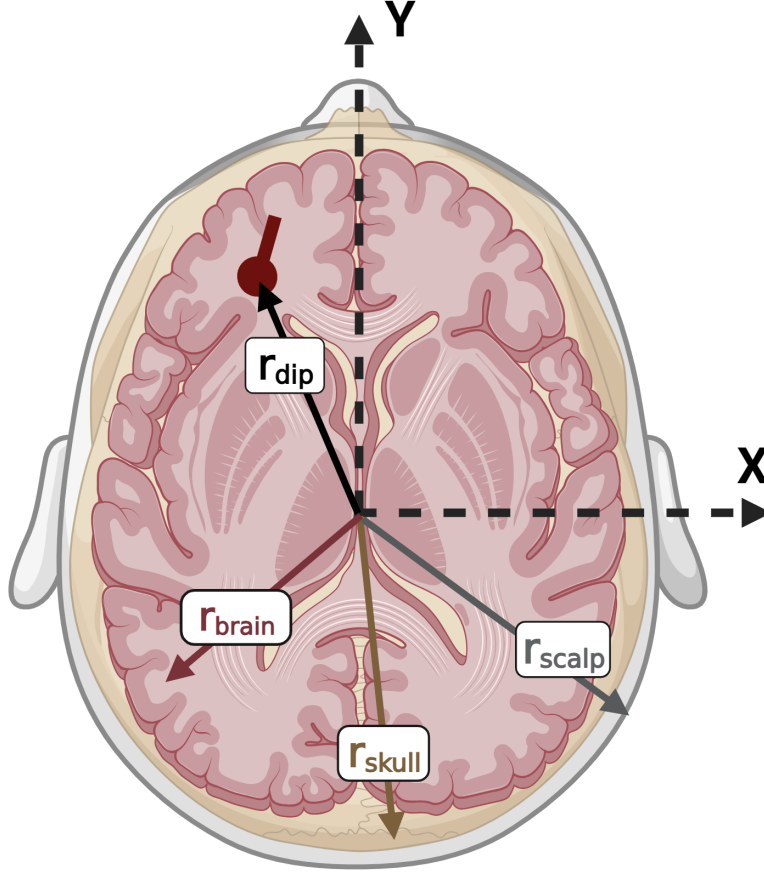
Figure 4.3: Illustration of a realistic layered head model [1]. The dipole's location ($\boldsymbol{r}_{dip}$) determines the head tissues that the electrical signal needs to go through to reach the electrodes.

In order to solve the FE model, one needs to discretize the equations and apply them to each element separately to calculate the nodal potential V_i (from node number 1 to n) as shown in equation 4.11, where φ_i is a set of test functions.

$$V = \sum_{i=1}^{n} V_i \varphi_i \tag{4.11}$$

Given the equations that are derived, the Galerkin approach [98, 100] is used to solve the proposed FE model as below:

$$\int_\Omega \nabla\varphi.\sigma(\mathbf{r})\nabla V d\Omega = \int_\Omega \varphi\partial\vec{\boldsymbol{j_p}}d\Omega \tag{4.12}$$

Substituting equation 4.11 in 4.12 leads to the equation 4.13, where $\mathbf{K}$ is the stiffness matrix, and $\mathbf{B}$ is the answer to the right-hand side of equation 4.12.

$$\boldsymbol{K}V_i = \boldsymbol{B} \tag{4.13}$$

Although the Galerkin FE is a proper approach to solving the forward problem, one should also consider solving the singularity problem. In other words, sometimes, the solution tends to generate an infinite value due to the minuscule gaps between monopoles. Among different methods to solve the singularity while utilizing the Finite Element Model, the Saint Venant approach is addressed in this study. This choice is because many available software, such as BESA, also use the Saint Venant approach to simulate the forward model [101], [102]. Later in this study, it is shown that BESA is used to validate the novel forward model presented in this study.

In Saint Venant's approach, a dipole located at $\vec{\boldsymbol{r_0}}$ is replaced by monopoles. These monopoles generate a new moment T and are placed at the closest nodes near the real dipole location (figure 4.4). In order to ensure that the new monopoles' model generates the same result as the dipole model, one needs to determine the monopoles' current so that it minimizes the difference between the dipole moment M and the new monopoles' moment T. The detailed calculation can be found in [98]. As a result, the associated current generated from these monopoles is called $\underline{\mathbf{j}}_{ven}$. Thus, the primary current is now calculated as presented in equation 4.14, which leads to a new Galerkin model shown in equation 4.15. The number of monopoles is presented by k in these equations. Finally, the solution of the equation. 4.16 leads to finding the potential on the scalp, which is the measured EEG signal.

$$\partial \vec{\boldsymbol{j_p}} = \sum_{v=1}^{k} \mathbf{j}_{\_ven} \, \delta \left(\vec{\boldsymbol{r}} - \vec{\boldsymbol{r}}_v \right) \tag{4.14}$$

$$\int_{\Omega} \varphi \partial \vec{\boldsymbol{j_p}} d\Omega = \sum_{v=1}^{k} \mathbf{j}_{\_ven} \int_{\Omega} \varphi \delta \left(\vec{\boldsymbol{r}} - \vec{\boldsymbol{r}}_v \right) \tag{4.15}$$

$$\int_{\Omega} \nabla \varphi . \sigma(\mathbf{r}) \nabla V d\Omega = \sum_{v=1}^{k} \mathbf{j}_{\_ven} \int_{\Omega} \varphi \delta \left(\vec{\boldsymbol{r}} - \vec{\boldsymbol{r}}_v \right) \tag{4.16}$$
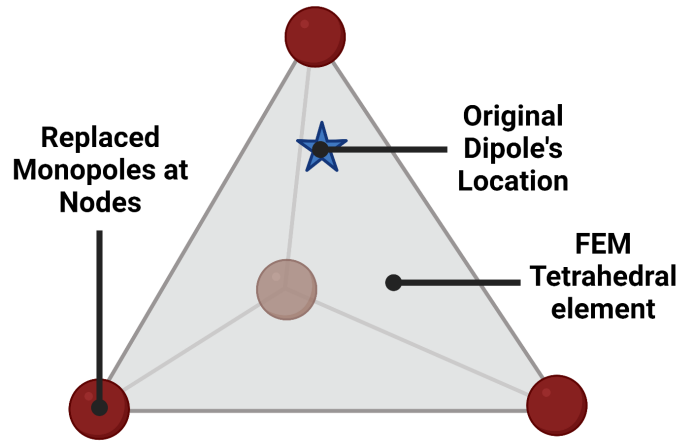
Figure 4.4: Illustration of a dipole in a tetrahedral mesh and the equivalent monopoles located at nodes [1].

4.2.3 Random Conductivity

As mentioned earlier, this chapter aims to address the effect of conductivity randomness all over the head model on the forward problem. To achieve this goal, the constant conductivity $\sigma(\boldsymbol{r})$ is replaced by $\sigma_{j,i}(\boldsymbol{r})$. In other words, the new head model consists of constant homogeneous paths between the dipole and the sensors. Fig.4.5 is provided to illustrate this new concept better.
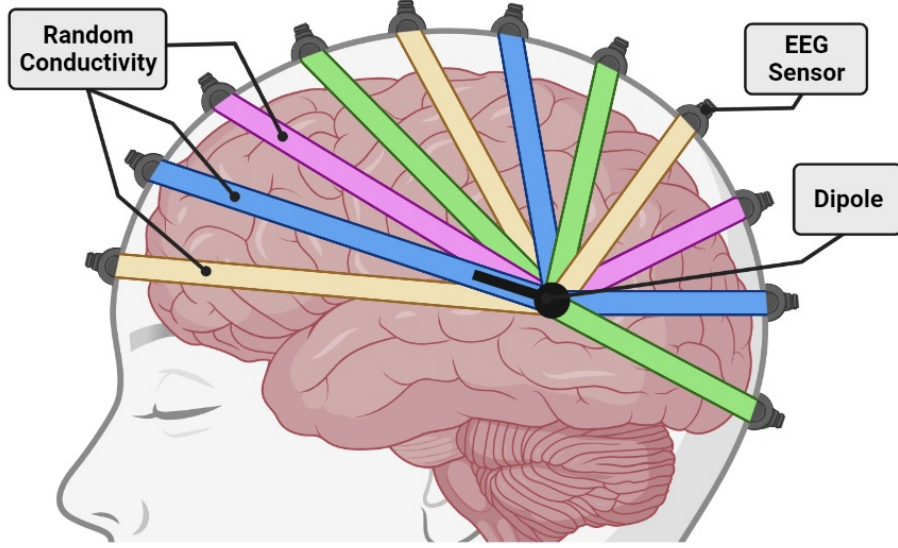
Figure 4.5: The head model with random conductivity paths [1].

Moreover, the modified forward model based on the random conductivity is provided in Eqn.4.17. Given this new circumstance, the EEG signal generated from the ith dipole will transmit through different conductivities to reach each different sensor. More details on how this assumption is added to the forward problem are described in the following section.

$$v_{j,i} = \frac{1}{4\pi\sigma_{j,i}(\boldsymbol{r})}\boldsymbol{g}_{j,i}\boldsymbol{\mu}_i s_i + n_j \tag{4.17}$$

4.3 Simulation Results

In order to compare the synthetic EEG signal generated by this novel method to conventional forward problems, one can use open-source software such as EEGLAB, BESA, etc. This study uses BESA to compare the EEG forward problem result for different circumstances, including single-source and multi-source.

Before generating the synthetic EEG signal with random conductivity using the forward model provided in Eqn. 4.1, it is essential to determine the range of

conductivity. In this study, the conductivity is uniformly distributed between 0.2 to 0.4 S/m. This conductivity range is selected based on the domain tissue conductivity in the head model. Referring to BESA software, the majority of head model tissue is the brain and scalp, with a conductivity of 0.33 S/m. Moreover, the skull has a low conductivity of 0.0042 S/m, and the CSF conductivity is 1 S/m. However, these tissues are less apparent in the head model compared to the brain. As a result, the conductivity range is between 0.2 to 0.4 S/m to include the effect of the skull and CSF.

We have shown the effect of random conductivity on the inverse problem, and EEG source identification previously in [48]. This study shows that this assumption works properly for dipole property estimation, including the location, orientation, and magnitude. Thus, this study focuses only on the effect of random head tissue conductivity on the EEG forward problem.

4.3.1 Synthetic Data Simulation Result

4.3.1.1 Single Dipole

The first simulation result is provided for the single dipole, located approximately at $(8, 31, 35)cm$ in the head model. The realistic forward model in BESA considers 81 different sensors, generating 200 samples. While BESA uses FEM to consider the head tissue conductivity and generate the EEG signal, the introduced model in this study employs the random distribution conductivity. As is shown in Fig. 4.5, a specific random conductivity is associated with each channel. Given this random conductivity distribution, the Monte Carlo simulation is done (100 times) to ensure an acceptable range of results is presented in this study. Thus, a total

of 8100 conductivities is generated for the simulation result, where this conductivity distribution is shown in a histogram in Fig. 4.6.
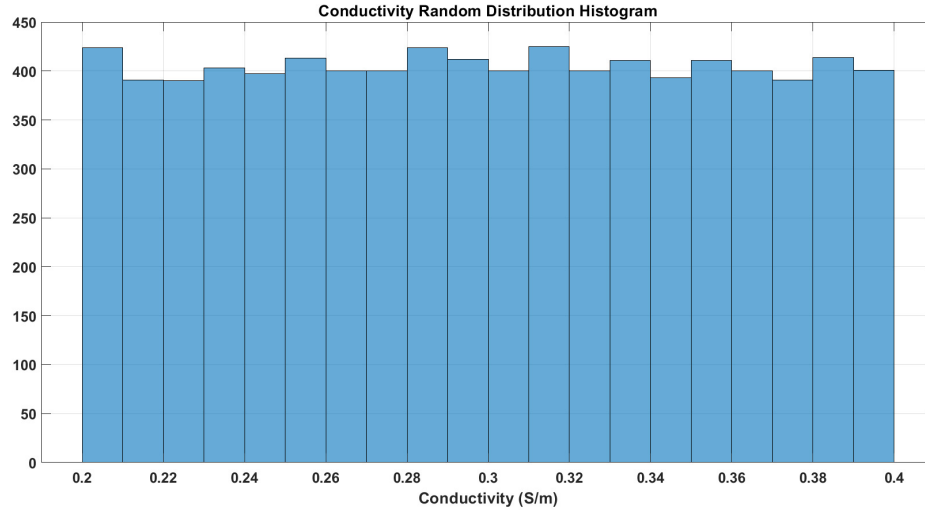
Figure 4.6: The randomly distributed conductivity histogram

In order to have a proper comparison between the BESA EEG data and the MATLAB simulated data, one can calculate the Euclidean norm of data for each channel (Eqn.4.18) and compare it this way. In this study, the Euclidean norm of jth channel data for BESA and MATLAB simulation are shown by $\left\|\boldsymbol{v}_j^B\right\|$, and $\left\|\boldsymbol{v}_j^M\right\|$, respectively. The result of this comparison is illustrated in Fig. 4.7. As is shown in this figure, the data generated from BESA and the random conductivity model are approximately similar. The average error of norms for this specific simulation is 3.67 μV, which means, on average, the norm of MATLAB simulated data is only 3.67 μV off from the BESA data. Considering a random head tissue conductivity, this slight difference confirms that this method works properly for applications that need a rough estimation in a short time, such as real-time EEG data analysis.

$$\|\boldsymbol{v}_j\| = \sqrt{\boldsymbol{v}_j^2(1) + \boldsymbol{v}_j^2(2) + \cdots + \boldsymbol{v}_j^2(N)} \tag{4.18}$$
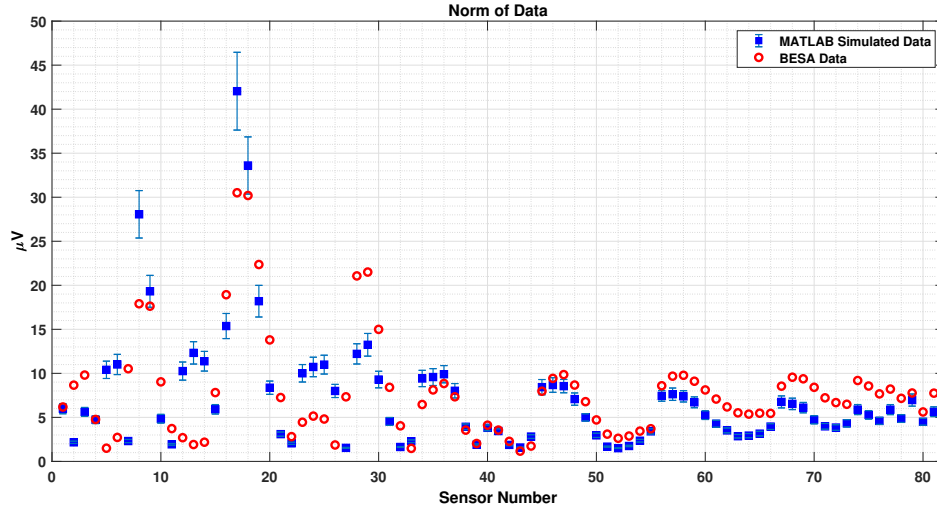
Figure 4.7: The EEG synthetic data generated by a single dipole. The norm of data for each sensor displayed for both MATLAB simulated data using the random conductivity and the data from BESA software.

4.3.1.2   Multi-Dipoles

In this section, the simulation result is generated for the multi-dipoles case where two dipoles are located at $(-33, 43, 38)cm$ and $(30, -10, 60)cm$ in the head model. The norm error for this case is $3.75\mu V$. Note that the BESA software uses the realistic head model with Talairach coordinates, where the head origin and axis direction are slightly different from the MNI coordinates that are used in MATLAB simulation. This difference in coordinates is one reason that makes the simulation result different in these two cases and increases the error.

Now that the two cases for synthetic data are addressed, and the result shows the efficiency of the proposed algorithm, it is time to check how this novel forward

model functions compared to the actual EEG data. The following section provides the result for this case.
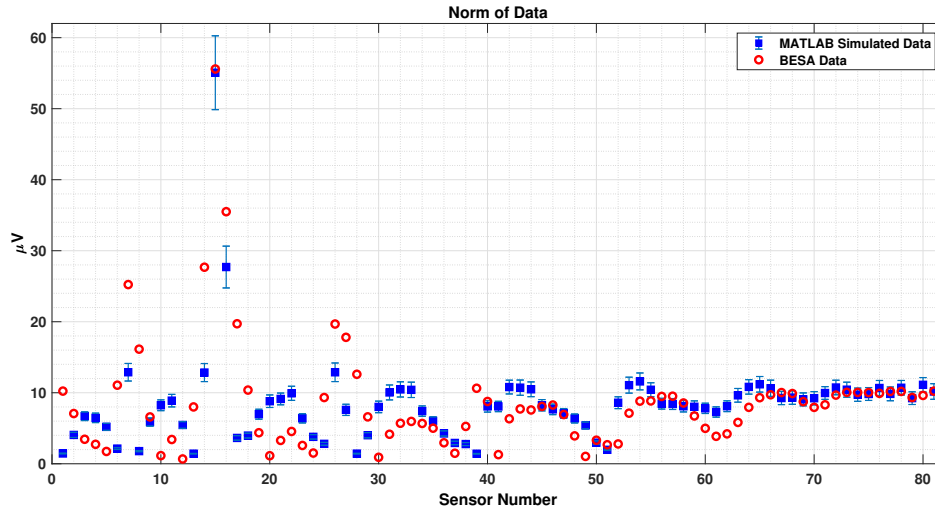
Figure 4.8: The EEG synthetic data generated by two dipoles. The norm of data for each sensor displayed for both MATLAB simulated data using the random conductivity and the data from BESA software.

4.3.2 Clinical Data Simulation Result

The EEGLAB website [67] provides different clinical EEG data sets. In this study, three of these data sets are selected and used to generate the simulation results. The first data set used in this study belongs to an experiment where the subject is asked to press a button when a square shape appears on the screen. More details of this experiment and how the data is collected are presented in [72]. The second data set is available for five subjects, who are asked to do an auditory task and detect the synonym or antonym of a word. Among these five subjects, the data from two different subjects are used to regenerate the EEG signal using the random conductivity forward model.

To generate the forward model, one needs the dipoles' properties associated with the EEG data set to substitute them in the forward model. Hence, the dipoles' properties are determined using the EEGLAB software inverse problem solution (DIP-FIT), and they are substituted in the forward problem presented in this study and BESA Simulator software. The reason to do so is to check if the presented algorithm can regenerate the EEG signal as well as software that employs the FEM model. Figs. 4.9a to 4.9c present the simulation result for these three clinical data sets. As mentioned before, since it is confusing to compare the data for all the sample points, the norm of data for each sensor is calculated and illustrated in these figures. For instance, $\left\|\boldsymbol{v}^E\right\|$, $\left\|\boldsymbol{v}^M\right\|$, and $\left\|\boldsymbol{v}^E\right\|$ implies the norm of data for EEGLAB, MATLAB simulation, and BESA data set respectively. Moreover, to have a better comparison of estimation errors, one can normalize the error by dividing them by the reference data range. In this case, the reference data set is from EEGLAB, and the goal is to find the simulation error of MATLAB simulation and BESA and compare it to the clinical data provided by EEGLAB. This Error Per Range is shown as EPR in this study and illustrated with an example in Eqn.4.19.

$$EPR_{BESA} = \frac{\left|\left(\left\|\boldsymbol{v}^B\right\| - \left\|\boldsymbol{v}^E\right\|\right)\right|}{Range(\left\|\boldsymbol{v}^E\right\|)} \times 100 \qquad (4.19)$$

Table 4.1 generated to show the numerical results for each simulation results. As shown in this table and the figures, the MATLAB simulated data using the random conductivity generates a better result than BESA, where they consider a more accurate head model. It is important to note that even though both BESA and EEGLAB use Talairach coordinates, the BESA forward problem result is not close to the actual EEG signal from EEGLAB. Besides the simulation error and the simulation EPR result, this table also provides the Root Mean Square Error (RMSE) calculated

by utilizing Eqn.4.20. Given the results in this table and the following figure, the MATLAB simulation result is significantly better than the BESA simulation result.

$$RMSE_{BESA} = \sqrt{\frac{\sum_{j=1}^{M} \left(\|\boldsymbol{v}^B(j)\| - \|\boldsymbol{v}^E(j)\| \right)^2}{M}} \tag{4.20}$$

Table 4.1: Numerical Results for Three Clinical Datasets

Data	Simulation error (μV)		Simulation RMSE (μV)		Simulation EPR (%)	
Number	MATLAB	BESA	MATLAB	BESA	MATLAB	BESA
1	41.79	142.17	48.99	179.44	15.95%	67.74%
2	151.87	371.00	461.52	1166.2	8.80%	21.51%
3	361.87	972.12	223.38	467.97	8.68%	22.23%
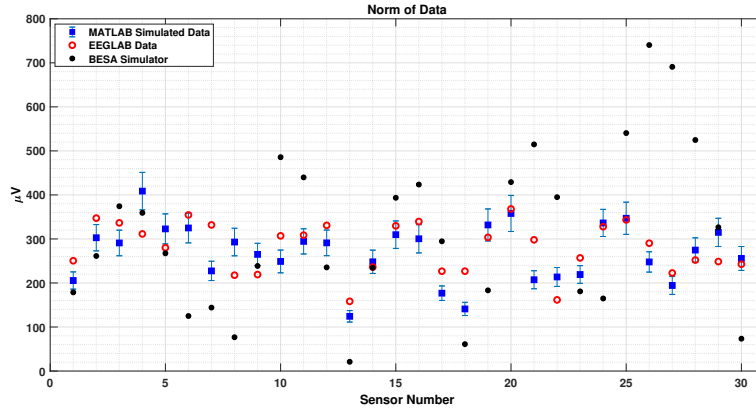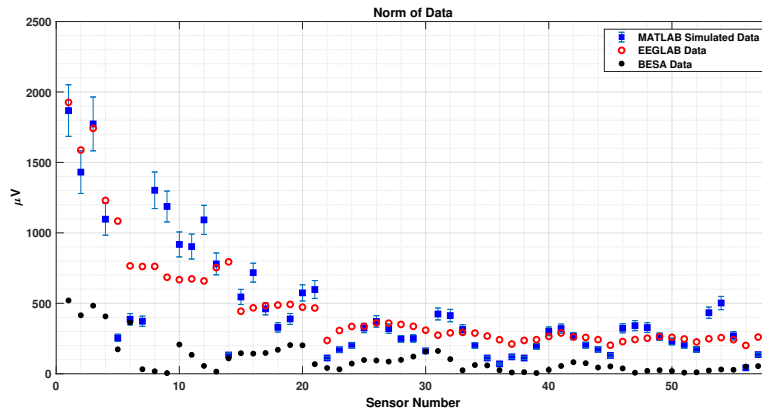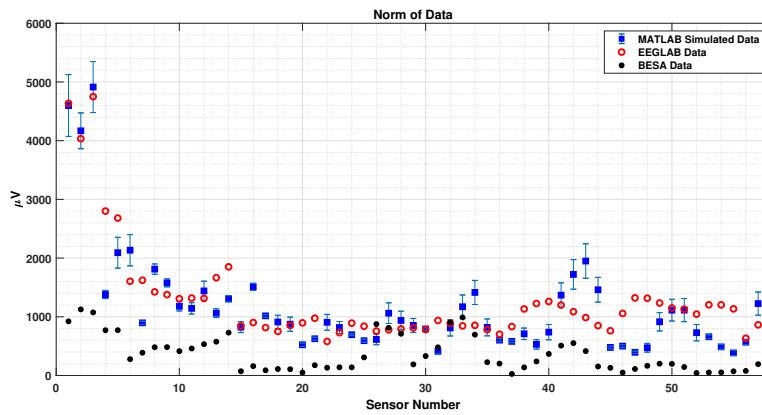
Figure 4.9: Comparison of EEGLAB clinical dataset to synthetic data generated from BESA using FEM head model and the proposed algorithm using random conductivity head model. The norm of data for each sensor displayed for all three data sets (EEGLAB, BESA Simulator, MATLAB simulation).

102

4.4   Conclusion

This chapter introduces a novel model based on random conductivity for solving the forward problem and generating synthetic EEG data. Unlike other standard forward models where different layers and materials of a realistic head model are considered, this novel forward model only uses the paths from the dipole in the head to each sensor on the scalp with their own random conductivity. It is essential to mention that this random conductivity is carefully chosen from $0.2S/m$ to $0.4S/m$ for optimal estimation of the real head model conductivity range. The idea of this randomly distributed conductivity head model comes from decreasing the computation cost of both the forward and inverse problems while analyzing the EEG data. In other words, using a realistic head model, as mentioned above, needs a computationally expensive algorithm such as Finite Element Method.

Regardless of the computational cost of a forward model, one should consider the method's accuracy too. Thus, to ensure the presented forward model is both fast and accurate, a set of simulations is provided in this chapter to generate an EEG signal and compare it to a well-known software where the FEM model is used. This simulation is done in two parts. First, a dipole is located in the head model to generate the synthetic EEG signal in both BESA Simulator software and MATLAB simulation using the random conductivity head model. This simulation is done for two cases of single-source and multi-source. For both simulations, the result shows that the generated EEG signal is approximately similar, considering totally different head models. Eventually, the same simulation is done on three sets of clinical EEG data sets. The EEGLAB website provides these data sets, and the same software is used to find the dipole properties associated with each data set. Afterward, these dipole properties pass to the MATLAB simulation and BESA Simulator to regenerate the same EEG clinical data. The results are compared to the actual EEG signal from

103

EEGLAB, and the random conductivity head model results are significantly better than the BESA Simulator.

In conclusion, a well-defined forward model considering a randomly distributed conductivity can be a proper substitute for the FEM head models, which need a higher computation load. This novel EEG forward model can be used for cases where the processing time is more important than the accuracy, for instance, the real-time EEG data analysis. Note that the presented forward model is still accurate enough and can generate roughly the same EEG signal as the clinical EEG data.

Chapter 5

Conclusions and Future Work

This thesis presented a novel algorithm to optimize the EEG source identification problem. This algorithm, which is based on constrained nonlinear least-squares, can estimate all the features of an electrical source (dipole), including the location, orientation, magnitude, and frequency. Given the absence of the physical source in the EEG-like signal, the actual values of source properties are unknown. Thus, to evaluate the accuracy of the proposed source identification algorithm and compare the estimation results to the actual values, one can use three main approaches.

Firstly, the forward model is utilized to generate synthetic EEG data associated with specific neural activities in the head model. In this case, it is assumed that all the dipoles' properties are available, and by substituting these values into the forward problem, the measured EEG data is generated. Thus, the source identification result can be compared to the assumptions that were initially made for the dipole properties.

Second, in this thesis, it is shown that our source identification results are accurate by comparing them to a well-known MATLAB-based algorithm called EEGLAB. Many different clinical and synthetic data samples are utilized to compare our simulation results to EEGLAB. As a result, it is shown that the proposed algorithm in this thesis can estimate all the dipole properties as accurately as EEGLAB. However, since our algorithm is based on the random conductivity head model, it has less computational complexity compared to EEGLAB.

Third, by providing an experimental setup, the efficiency of the proposed EEG source identification algorithm is assessed. The experimental setup consists of a

bucket filled with salt and water. This simple experimental setup is designed to be a prototype for the phantom head. Although this setup is simple and yet needs modifications to compare to a phantom head, it is very common for fundamental EEG signal tests. In order to have a setup with features close to an EEG signal study, the EEG sensors are used and attached to the bucket. Moreover, the conductivity of the salt and water is approximately $0.33S/m$, which equals the brain's conductivity. The electrical source generates a sine wave, and as mentioned previously, all the source properties are known. The generated sine wave electrical signals have different frequencies to make the test more complicated and challenge the least squares error based source identification algorithm. The proposed algorithm uses the measured data from different oscillatory signal sources and solves an inverse problem by minimizing a cost function to estimate all the signal properties, including the locations, frequencies, and phases. To increase the overall signal accuracy for a wide range of initial guess frequencies, we have utilized the Lomb-Scargle spectral analysis along with the Least Squares error optimization method. We observed that our algorithm can identify the source location within 10 mm from the actual source immersed inside the bucket of radius $=\sim$ 90 mm. Moreover, the frequency estimation error is nearly zero, which justifies the effectiveness of our proposed method.

Finally, we focus more on the novel introduced head model, which considered different conductivities without using Finite Element Method (FEM). This approach is based on random conductivity distribution and is computationally less expensive than FEM while providing an acceptable result to generate EEG signals using Forward Model. The generated EEG signals from this novel head model are compared to clinical EEG data sets and also to a well-known software called BESA. BESA is also generating the forward model using a FEM-based head model.

Since the introduced algorithm in this thesis has less computational complexity without sacrificing the accuracy of the EEG source properties identification, one can develop this research into a real-time EEG signal analysis algorithm. As a future work, this real-time algorithm can be useful in the creation of a helmet equipped with integrated EEG sensors. A microprocessor attached to this helmet can monitor and measure the real-time EEG data, process it utilizing our introduced source identification algorithm, and alert the person wearing the helmet in the event of any brain injury. An example of using this helmet could be in sports where brain injury is more common such as boxing, and football. A prototype of this idea is shown in Chapter 2 of this thesis, where a Raspberry Pi model 4b is used as a microprocessor (Fig.2.28).

References

[1] "Created with https://BioRender.com."

[2] P. J. Talairach, Co-planar stereotaxic atlas of the human brain. George Thieme Verlag, 1988.

[3] N. Makris, "Anatomical coordinate systems in brain analysis," in Advances in Magnetic Resonance Technology and Applications. Elsevier, 2023, vol. 6, pp. 83–95.

[4] L. Collins, "3d model-based segmentation of individual brain structures from magnetic resonance imaging data," Ph.D. dissertation, McGiII University, 1994.

[5] A. Warner, J. Tate, B. Burton, and C. R. Johnson, "A high-resolution head and brain computer model for forward and inverse eeg simulation," bioRxiv, p. 552190, 2019.

[6] L. M. Angelone, C. E. Vasios, G. Wiggins, P. L. Purdon, and G. Bonmassar, "On the effect of resistive eeg electrodes and leads during 7 t mri: simulation and temperature measurement studies," Magnetic resonance imaging, vol. 24, no. 6, pp. 801–812, 2006.

[7] J. Haueisen, C. Ramon, M. Eiselt, H. Brauer, and H. Nowak, "Influence of tissue resistivities on neuromagnetic fields and electric potentials studied with a finite element model of the head," IEEE Transactions on Biomedical Engineering, vol. 44, no. 8, pp. 727–735, 1997.

[8] J. J. Ermer, J. C. Mosher, S. Baillet, and R. M. Leahy, "Rapidly recomputable eeg forward models for realistic head shapes," Physics in Medicine & Biology, vol. 46, no. 4, p. 1265, 2001.

[9] Y. Wang, <u>Successive Estimation Method of Locating Dipoles based on QR Decomposition using EEG Arrays</u>. McMaster University, https://macsphere.mcmaster.ca/handle/11375/22455, 2007.

[10] S. Baillet, J. C. Mosher, and R. M. Leahy, "Electromagnetic brain mapping," <u>IEEE Signal processing magazine</u>, vol. 18, no. 6, pp. 14–30, 2001.

[11] J. Vorwerk, "New finite element methods to solve the eeg/meg forward problem," Ph.D. dissertation, Westfälische Wilhelms-Universität Münster, 2016.

[12] Ü. Aydin, J. Vorwerk, P. Küpper, M. Heers, H. Kugel, A. Galka, L. Hamid, J. Wellmer, C. Kellinghaus, S. Rampp <u>et al.</u>, "Combining eeg and meg for the reconstruction of epileptic activity using a calibrated realistic volume conductor model," <u>PloS one</u>, vol. 9, no. 3, p. e93154, 2014.

[13] S. Lau, D. Güllmar, L. Flemming, D. B. Grayden, M. J. Cook, C. H. Wolters, and J. Haueisen, "Skull defects in finite element head models for source reconstruction from magnetoencephalography signals," <u>Frontiers in neuroscience</u>, vol. 10, p. 141, 2016.

[14] F. Drechsler, C. H. Wolters, T. Dierkes, H. Si, and L. Grasedyck, "A full subtraction approach for finite element method based source analysis using constrained delaunay tetrahedralisation," <u>NeuroImage</u>, vol. 46, no. 4, pp. 1055–1065, 2009.

[15] J. Vorwerk, M. Clerc, M. Burger, and C. Wolters, "Comparison of boundary element and finite element approaches to the eeg forward problem," <u>Biomedical Engineering/Biomedizinische Technik</u>, vol. 57, no. SI-1-Track-O, pp. 795–798, 2012.

[16] H. Buchner, G. Knoll, M. Fuchs, A. Rienäcker, R. Beckmann, M. Wagner, J. Silny, and J. Pesch, "Inverse localization of electric dipole current sources in finite element models of the human head," <u>Electroencephalography and clinical Neurophysiology</u>, vol. 102, no. 4, pp. 267–278, 1997.

[17] S. Vallaghé and T. Papadopoulo, "A trilinear immersed finite element method for solving the electroencephalography forward problem," SIAM Journal on Scientific Computing, vol. 32, no. 4, pp. 2379–2394, 2010.

[18] S. Pursiainen, A. Sorrentino, C. Campi, and M. Piana, "Forward simulation and inverse dipole localization with the lowest order raviart—thomas elements for electroencephalography," Inverse Problems, vol. 27, no. 4, p. 045003, 2011.

[19] P. H. Schimpf, C. Ramon, and J. Haueisen, "Dipole models for the eeg and meg," IEEE Transactions on Biomedical Engineering, vol. 49, no. 5, pp. 409–418, 2002.

[20] J. Vorwerk, C. Engwer, S. Pursiainen, and C. H. Wolters, "A mixed finite element method to solve the eeg forward problem," IEEE transactions on medical imaging, vol. 36, no. 4, pp. 930–941, 2016.

[21] Y. Xu, W. Xue, Y. Li, L. Guo, and W. Shang, "Multiple signal classification algorithm based electric dipole source localization method in an underwater environment," Symmetry, vol. 9, no. 10, p. 231, 2017.

[22] Y. Xu, W. Shang, L. Guo, J. Qi, Y. Li, and W. Xue, "Active electro-location of objects in the underwater environment based on the mixed polarization multiple signal classification algorithm," Sensors, vol. 18, no. 2, p. 554, 2018.

[23] P. Mégevand and M. Seeck, "Electroencephalography, magnetoencephalography and source localization: their value in epilepsy," Current opinion in neurology, vol. 31, no. 2, pp. 176–183, 2018.

[24] I. Ullah, M. Hussain, H. Aboalsamh et al., "An automated system for epilepsy detection using EEG brain signals based on deep learning approach," Expert Systems with Applications, vol. 107, pp. 61–71, 2018.

[25] G. L. Barkley and C. Baumgartner, "MEG and EEG in epilepsy," Journal of clinical neurophysiology, vol. 20, no. 3, pp. 163–178, 2003.

[26] H. McCann, G. Pisano, and L. Beltrachini, "Variation in reported human head tissue electrical conductivity values," Brain topography, vol. 32, no. 5, pp. 825–858, 2019.

[27] L. Koessler, L. Maillard, A. Benhadid, J.-P. Vignal, M. Braun, and H. Vespignani, "Spatial localization of EEG electrodes," Neurophysiologie Clinique/Clinical Neurophysiology, vol. 37, no. 2, pp. 97–102, 2007.

[28] P. A. Abhang, B. W. Gawali, and S. C. Mehrotra, "Technological basics of EEG recording and operation of apparatus," Introduction to EEG-and Speech-Based Emotion Recognition, pp. 19–50, 2016.

[29] M. Teplan, "Fundamentals of EEG measurement. meas sci rev 2: 1–11," 2002.

[30] U. R. Acharya, H. Fujita, V. K. Sudarshan, S. Bhat, and J. E. Koh, "Application of entropies for automated diagnosis of epilepsy using EEG signals: A review," Knowledge-based systems, vol. 88, pp. 85–96, 2015.

[31] M. A. Jatoi, N. Kamel, A. S. Malik, I. Faye, and T. Begum, "A survey of methods used for source localization using EEG signals," Biomedical Signal Processing and Control, vol. 11, pp. 42–52, 2014.

[32] T. Wu, W. Li, L. Li, and T. Zeng, "A convex variational approach for image deblurring with multiplicative structured noise," IEEE Access, vol. 8, pp. 37 790–37 807, 2020.

[33] T. Tirer and R. Giryes, "Image restoration by iterative denoising and backward projections," IEEE Transactions on Image Processing, vol. 28, no. 3, pp. 1220–1234, 2018.

[34] Y. Tang, M. Wen, and T. Zeng, "Preconditioned three-operator splitting algorithm with applications to image restoration," Journal of Scientific Computing, vol. 92, no. 3, pp. 1–26, 2022.

[35] T. Baldwin, F. Renovich, L. F. Saunders, and D. Lubkeman, "Fault locating in ungrounded and high-resistance grounded systems," IEEE Transactions on Industry Applications, vol. 37, no. 4, pp. 1152–1159, 2001.

[36] X. Ding, H. Liang, A. Jakobsson, X. Tu, and Y. Huang, "High-resolution source localization exploiting the sparsity of the beamforming map," Signal Processing, vol. 192, p. 108377, 2022.

[37] N. Chu, Q. Huang, L. Yu, Y. Ning, and D. Wu, "Rotating acoustic source localization: A power propagation forward model and its high-resolution inverse methods," Measurement, vol. 174, p. 109006, 2021.

[38] M. S. Hämäläinen and R. J. Ilmoniemi, "Interpreting magnetic fields of the brain: minimum norm estimates," Medical & biological engineering & computing, vol. 32, no. 1, pp. 35–42, 1994.

[39] R. D. Pascual-Marqui, C. M. Michel, and D. Lehmann, "Low resolution electromagnetic tomography: a new method for localizing electrical activity in the brain," International Journal of psychophysiology, vol. 18, no. 1, pp. 49–65, 1994.

[40] O. Hauk, "Keep it simple: a case for using classical minimum norm estimation in the analysis of EEG and MEG data," Neuroimage, vol. 21, no. 4, pp. 1612–1621, 2004.

[41] I. F. Gorodnitsky, J. S. George, and B. D. Rao, "Neuromagnetic source imaging with FOCUSS: a recursive weighted minimum norm algorithm," Electroencephalography and clinical Neurophysiology, vol. 95, no. 4, pp. 231–251, 1995.

[42] J. C. Mosher, P. S. Lewis, and R. M. Leahy, "Multiple dipole modeling and localization from spatio-temporal MEG data," IEEE transactions on biomedical engineering, vol. 39, no. 6, pp. 541–557, 1992.

[43] J. Wind, E. Tijs, and H.-E. de Bree, "Source localization using acoustic vector sensors: A MUSIC approach," in Novem2009: Noise and Vibration: Emerging Methods. ISVR, 2009, pp. 1–10.

[44] T. Kundu, "Acoustic source localization," Ultrasonics, vol. 54, no. 1, pp. 25–38, 2014.

[45] H. C. So, "Source localization: Algorithms and analysis," Handbook of Position Location: Theory, Practice, and Advances, pp. 25–66, 2011.

[46] R. Grech, T. Cassar, J. Muscat, K. P. Camilleri, S. G. Fabri, M. Zervakis, P. Xanthopoulos, V. Sakkalis, and B. Vanrumste, "Review on solving the inverse problem in EEG source analysis," Journal of neuroengineering and rehabilitation, vol. 5, no. 1, pp. 1–33, 2008.

[47] Y. Xu, L. Guo, W. Shang, and Y. Li, "Underwater electro-location method based on improved matrix adaptation evolution strategy," IEEE Access, vol. 6, pp. 39 220–39 232, 2018.

[48] S. Namazifard and K. Subbarao, "Multiple dipole source position and orientation estimation using non-invasive eeg-like signals," Sensors, vol. 23, no. 5, p. 2855, 2023.

[49] M. Peivandi, S. Z. Ardabili, S. Sheykhivand, and S. Danishvar, "Deep learning for detecting multi-level driver fatigue using physiological signals: a comprehensive approach," Sensors, vol. 23, no. 19, p. 8171, 2023.

[50] X. Li, B. Hu, T. Xu, J. Shen, and M. Ratcliffe, "A study on eeg-based brain electrical source of mild depressed subjects," Computer methods and programs in biomedicine, vol. 120, no. 3, pp. 135–141, 2015.

[51] R. Cooper, J. W. Osselton, and J. C. Shaw, EEG technology. Butterworth-Heinemann, 2014.

[52] D. Cohen, B. N. Cuffin, K. Yunokuchi, R. Maniewski, C. Purcell, G. R. Cosgrove, J. Ives, J. G. Kennedy, and D. L. Schomer, "Meg versus eeg localization test using implanted sources in the human brain," Annals of Neurology: Official Journal of the American Neurological Association and the Child Neurology Society, vol. 28, no. 6, pp. 811–817, 1990.

[53] Z. J. Koles, "Trends in eeg source localization," Electroencephalography and clinical Neurophysiology, vol. 106, no. 2, pp. 127–137, 1998.

[54] H. Hallez, B. Vanrumste, R. Grech, J. Muscat, W. De Clercq, A. Vergult, Y. D'Asseler, K. P. Camilleri, S. G. Fabri, S. Van Huffel et al., "Review on solving the forward problem in eeg source analysis," Journal of neuroengineering and rehabilitation, vol. 4, no. 1, p. 46, 2007.

[55] Z. A. Acar and S. Makeig, "Effects of forward model errors on eeg source localization," Brain topography, vol. 26, no. 3, pp. 378–396, 2013.

[56] S. Tissari and J. Rahola, "Error analysis of a galerkin method to solve the forward problem in meg using the boundary element method," Computer methods and programs in biomedicine, vol. 72, no. 3, pp. 209–222, 2003.

[57] A. K. Liu, A. M. Dale, and J. W. Belliveau, "Monte carlo simulation studies of eeg and meg localization accuracy," Human brain mapping, vol. 16, no. 1, pp. 47–62, 2002.

[58] R. Schmidt, "Multiple emitter location and signal parameter estimation," IEEE transactions on antennas and propagation, vol. 34, no. 3, pp. 276–280, 1986.

[59] J. C. Mosher and R. M. Leahy, "Source localization using recursively applied and projected (rap) music," IEEE Transactions on signal processing, vol. 47, no. 2, pp. 332–340, 1999.

[60] F. Costa, H. Batatia, L. Chaari, and J.-Y. Tourneret, "Sparse eeg source localization using bernoulli laplacian priors," IEEE Transactions on Biomedical Engineering, vol. 62, no. 12, pp. 2888–2898, 2015.

[61] V. Montes-Restrepo, P. van Mierlo, G. Strobbe, S. Staelens, S. Vandenberghe, and H. Hallez, "Influence of skull modeling approaches on EEG source localization," Brain topography, vol. 27, no. 1, pp. 95–111, 2014.

[62] M. Dannhauer, B. Lanfer, C. H. Wolters, and T. R. Knösche, "Modeling of the human skull in eeg source analysis," Human brain mapping, vol. 32, no. 9, pp. 1383–1399, 2011.

[63] L. Rahmouni, R. Mitharwal, and F. P. Andriulli, "Two volume integral equations for the inhomogeneous and anisotropic forward problem in electroencephalography," Journal of Computational Physics, vol. 348, pp. 732–743, 2017.

[64] G. Lantz, R. G. De Peralta, L. Spinelli, M. Seeck, and C. Michel, "Epileptic source localization with high density eeg: how many electrodes are needed?" Clinical neurophysiology, vol. 114, no. 1, pp. 63–69, 2003.

[65] J. Song, C. Davey, C. Poulsen, P. Luu, S. Turovets, E. Anderson, K. Li, and D. Tucker, "EEG source localization: sensor density and head surface coverage," Journal of neuroscience methods, vol. 256, pp. 9–21, 2015.

[66] L. Beltrachini, N. von Ellenrieder, and C. H. Muravchik, "General bounds for electrode mislocation on the eeg inverse problem," Computer methods and programs in biomedicine, vol. 103, no. 1, pp. 1–9, 2011.

[67] "Eeglab tutorial data, https://eeglab.org/tutorials/tutorial_data.html."

[68] S. Y. Gordleeva, S. A. Lobov, N. A. Grigorev, A. O. Savosenkov, M. O. Shamshin, M. V. Lukoyanov, M. A. Khoruzhko, and V. B. Kazantsev, "Real-time eeg–emg human–machine interface-based control system for a lower-limb exoskeleton," IEEE Access, vol. 8, pp. 84 070–84 081, 2020.

115

[69] C. M. Michel and D. Brunet, "EEG source imaging: a practical review of the analysis steps," Frontiers in neurology, vol. 10, p. 325, 2019.

[70] A. Delorme and S. Makeig, "Eeglab: an open source toolbox for analysis of single-trial eeg dynamics including independent component analysis," Journal of neuroscience methods, vol. 134, no. 1, pp. 9–21, 2004.

[71] "Fieldtrip toolbox, http://www.fieldtriptoolbox.org/."

[72] S. Makeig, M. Westerfield, T.-P. Jung, S. Enghoff, J. Townsend, E. Courchesne, and T. J. Sejnowski, "Dynamic brain sources of visual evoked responses," Science, vol. 295, no. 5555, pp. 690–694, 2002.

[73] F. Artoni, D. Menicucci, A. Delorme, S. Makeig, and S. Micera, "Relica: a method for estimating the reliability of independent components," Neuroimage, vol. 103, pp. 391–400, 2014.

[74] I. Obeid and J. Picone, "The temple university hospital eeg data corpus," Frontiers in neuroscience, vol. 10, p. 196, 2016.

[75] S. Namazifard, R. R. Daru, K. Tighe, K. Subbarao, and A. Adnan, "Method for identification of multiple low-voltage signal sources transmitted through a conductive medium," IEEE Access, vol. 10, pp. 124 154–124 166, 2022.

[76] S. Namazifard and K. Subbarao, "Multiple dipole source position and orientation estimation using non-invasive EEG signals," submitted to IEEE Access (preprint on 10.36227/techrxiv.21049585), 2022.

[77] N. R. Lomb, "Least-squares frequency analysis of unequally spaced data," Astrophysics and space science, vol. 39, no. 2, pp. 447–462, 1976.

[78] A. Bryson and Y. Ho, Applied Optimal Control: Optimization, Estimation, and Control. Taylor & Francis Group, 1975.

[79] M. A. Lopez-Gordo, D. Sanchez-Morillo, and F. P. Valle, "Dry EEG electrodes," Sensors, vol. 14, no. 7, pp. 12 847–12 870, 2014.

[80] C. Ramon, P. Garguilo, E. A. Fridgeirsson, and J. Haueisen, "Changes in scalp potentials and spatial smoothing effects of inclusion of dura layer in human head models for EEG simulations," Frontiers in neuroengineering, vol. 7, p. 32, 2014.

[81] J. Kamcev, R. Sujanani, E.-S. Jang, N. Yan, N. Moe, D. R. Paul, and B. D. Freeman, "Salt concentration dependence of ionic conductivity in ion exchange membranes," Journal of Membrane Science, vol. 547, pp. 123–133, 2018.

[82] N. Shahcheraghi, H. Golchin, Z. Sadri, Y. Tabari, F. Borhanifar, and S. Makani, "Nano-biotechnology, an applicable approach for sustainable future," 3 Biotech, vol. 12, no. 3, p. 65, 2022.

[83] S. Asadzadeh, T. Y. Rezaii, S. Beheshti, A. Delpak, and S. Meshgini, "A systematic review of eeg source localization techniques and their applications on diagnosis of brain abnormalities," Journal of Neuroscience Methods, vol. 339, p. 108740, 2020.

[84] O. H. Milani, T. Nguyen, A. Parekh, A. E. Cetin, and B. Prasad, "0537 incident hypertension prediction in obstructive sleep apnea using machine learning," Sleep, vol. 46, no. Supplement_1, pp. A236–A237, 2023.

[85] Z. Akalin Acar and S. Makeig, "Effects of forward model errors on eeg source localization," Brain topography, vol. 26, pp. 378–396, 2013.

[86] J. Vorwerk, Ü. Aydin, C. H. Wolters, and C. R. Butson, "Influence of head tissue conductivity uncertainties on eeg dipole reconstruction," Frontiers in neuroscience, vol. 13, p. 531, 2019.

[87] F. Vatta, F. Meneghini, F. Esposito, S. Mininel, and F. Di Salle, "Realistic and spherical head modeling for eeg forward problem solution: a comparative cortex-based analysis," Computational intelligence and neuroscience, vol. 2010, 2010.

[88] H. Azizollahi, A. Aarabi, and F. Wallois, "Effect of structural complexities in head modeling on the accuracy of eeg source localization in neonates," Journal of Neural Engineering, vol. 17, no. 5, p. 056004, 2020.

[89] N. Von Ellenrieder, C. H. Muravchik, and A. Nehorai, "Effects of geometric head model perturbations on the eeg forward and inverse problems," IEEE Transactions on Biomedical Engineering, vol. 53, no. 3, pp. 421–429, 2006.

[90] N. G. Gençer and C. E. Acar, "Sensitivity of eeg and meg measurements to tissue conductivity," Physics in Medicine & Biology, vol. 49, no. 5, p. 701, 2004.

[91] S. J. Hund, B. R. Brown, C. L. Lemale, P. G. Menon, K. A. Easley, J. P. Dreier, and S. C. Jones, "Numerical simulation of concussive-generated cortical spreading depolarization to optimize dc-eeg electrode spacing for noninvasive visual detection," Neurocritical Care, vol. 37, no. Suppl 1, pp. 67–82, 2022.

[92] M. Antonakakis, S. Schrader, Ü. Aydin, A. Khan, J. Gross, M. Zervakis, S. Rampp, and C. H. Wolters, "Inter-subject variability of skull conductivity and thickness in calibrated realistic head models," Neuroimage, vol. 223, p. 117353, 2020.

[93] K. A. Awada, D. R. Jackson, S. B. Baumann, J. T. Williams, D. R. Wilton, P. W. Fink, and B. R. Prasky, "Effect of conductivity uncertainties and modeling errors on eeg source localization using a 2-d model," IEEE Transactions on Biomedical Engineering, vol. 45, no. 9, pp. 1135–1145, 1998.

[94] L. Beltrachini, "A finite element solution of the forward problem in eeg for multipolar sources," IEEE Transactions on Neural Systems and Rehabilitation Engineering, vol. 27, no. 3, pp. 368–377, 2018.

[95] T. Erdbrügger, A. Westhoff, M. Höltershinken, J.-O. Radecke, Y. Buschermöhle, A. Buyx, F. Wallois, S. Pursiainen, J. Gross, R. Lencer

et al., "Cutfem forward modeling for eeg source analysis," Frontiers in Human Neuroscience, vol. 17, 2023.

[96] R. L. Harrison, "Introduction to monte carlo simulation," in AIP conference proceedings, vol. 1204, no. 1. American Institute of Physics, 2010, pp. 17–21.

[97] M. Khalafi and D. Boob, "Accelerated primal-dual methods for convex-strongly-concave saddle point problems," in International Conference on Machine Learning. PMLR, 2023, pp. 16 250–16 270.

[98] T. Medani, D. Lautru, D. Schwartz, Z. Ren, and G. Sou, "Fem method for the eeg forward problem and improvement based on modification of the saint venant's method," Progress In Electromagnetics Research, vol. 153, pp. 11–22, 2015.

[99] Z. Wang, G. Wang, and C. Yu, "Numerical simulation of repetitive transcranial magnetic stimulation by the smoothed finite element method," Engineering Analysis with Boundary Elements, vol. 147, pp. 138–151, 2023.

[100] S. Lew, C. Wolters, T. Dierkes, C. Röer, and R. MacLeod, "Accuracy and run-time comparison for different potential approaches and iterative solvers in finite element method based eeg source analysis," Applied Numerical Mathematics, vol. 59, no. 8, pp. 1970–1988, 2009.

[101] K. Unnwongse, S. Rampp, T. Wehner, A. Kowoll, Y. Parpaley, M. von Lehe, B. Lanfer, M. Rusiniak, C. Wolters, and J. Wellmer, "Validating eeg source imaging using intracranial electrical stimulation," Brain Communications, vol. 5, no. 1, p. fcad023, 2023.

[102] "Besa simulator, https://www.besa.de/products/besa-simulator/besa-simulator-overview/."

Biographical Statement

Saina Namazifard was born in Tehran, Iran. She received her B.Sc. and M.Sc. degrees in Mechanical Engineering from K. N. Toosi University of Technology. In Fall 2019, Saina started her Ph.D. program in Mechanical Engineering at the University of Texas at Arlington (UTA). She joined the Aerospace System Lab (ASL) as a Graduate Research Assistant and worked on projects with a focus on Optimization, Biological Signal Processing, and Computational Neuroscience. After earning her Ph.D., the Baylor College of Medicine is her next destination, where she will grow her expertise in the field of Computational Neuroscience.